Marcelo De Lellis Costa de Oliveira

AIRBORNE WIND ENERGY WITH TETHERED WINGS: MODELING, ANALYSIS AND CONTROL

Doctoral Dissertation submitted to the Post-graduate Course in Automation and Systems Engineering as a requirement for the degree of Doctor (Dr.) in Automation and Systems Engineering.
Advisor: Prof. Alexandre Trofino Neto, Dr.

Florianópolis

2016

Marcelo De Lellis Costa de Oliveira

AIRBORNE WIND ENERGY WITH TETHERED WINGS: MODELING, ANALYSIS AND CONTROL

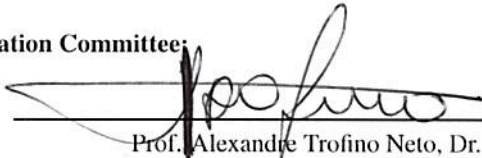This Doctoral Dissertation was deemed adequate for awarding the degree of "Doctor (Dr.) in Automation and Systems Engineering", and approved in its final form by the Postgraduate Course in Automation and Systems Engineering.

Florianópolis, September 30th, 2016.

_____

Prof. Daniel Ferreira Coutinho, Dr.
Course Coordinator

Examination Committee:

_____

Prof. Alexandre Trofino Neto, Dr.
President

Prof. Lorenzo Fagiano, Dr.
Politecnico di Milano

Prof. Roland Schmehl, Dr.
Delft University of Technology

Prof. Flávio Silvestre, Dr.
Instituto Tecnológico de Aeronáutica

Prof. Alexandre Sanfelice Bazanella, Dr.
Universidade Federal do Rio Grande do Sul

Prof. Daniel Martins, Dr.
Universidade Federal de Santa Catarina

Prof. Edson Roberto De Pieri, Dr.
Universidade Federal de Santa Catarina

To my parents, Alvaro and Rejane.

ACKNOWLEDGEMENTS

"The only true wisdom is in knowing you know nothing."

(Socrates, 469 BC – 399 BC)

ABSTRACT

Airborne Wind Energy (AWE) is an emerging field of technology that investigates wind power devices capable of remaining airborne either through aerostatic or aerodynamic forces. Consequently, the heavy and expensive tower of conventional horizontal-axis wind turbines is no longer needed, allowing the AWE device to operate at higher altitudes, where the wind tends to be steadier and stronger and, therefore, more power is available. Another claimed advantage is the reduction on overall costs, especially regarding transportation and installation, due to the absence of the tower to withstand the torque caused by the rotating turbine, thus also requiring a simpler foundation. Several AWE concepts have been proposed, among which the pumping kite stands out as one of the simplest and cheapest, essentially comprising a ground winch where energy is generated, and a tethered wing that can be either flexible or rigid. This dissertation contributes to the field of AWE by addressing the pumping kite in four different aspects. The goal is to serve both as a manuscript for the lay reader with some background on physics, aerodynamics, dynamic systems, classic control and optimization techniques, as well as by specialists in either of these areas who intend to carry out deeper investigations. The first contribution is to revisit in detail important models in the literature used to simulate the flight dynamics, to design and to validate control laws. Namely, the 3D two-tether point-mass wing (to which modifications are proposed), the massless wing in dynamic equilibrium, the course angle dynamics and the logarithmic wind shear model are addressed. The second contribution is a comparative study of flight controllers whose references are computed separately from the ground winch control, in a decentralized topology. A two-loop approach is considered, where the outer loop defines a reference trajectory and generates a reference for the course angle, which is then tracked in the inner loop by manipulating the steering input of the tethered wing. A third contribution is the formulation of an optimization problem to choose the operating parameters of the traction and retraction phases that yield the maximum cycle power. One of the main findings is that, by reeling out at a lower speed than the value that maximizes the traction power, the duty cycle increases and, thereby, also the cycle power. The last major contribution is to reinterpret Loyd's lift (the pumping kite traction phase) and drag modes as particular cases of the actuator disc considered in the derivation of the Betz limit for power extraction from the wind. The expression for the lift mode power coefficient is formulated using blade element momentum theory.

Keywords: Airborne wind energy. Modeling. Flight control.

RESUMO ESTENDIDO

Energia eólica aérea (*Airborne Wind Energy (AWE)*, em inglês) é uma tecnologia de energia renovável que trata de dispositivos que aproveitam a energia cinética do vento e são capazes de se manter no ar através de forças aerostáticas ou forças aerodinâmicas. Este campo de estudos vem atraindo cada vez mais pesquisas devido a duas grandes vantagens previstas sobre a tecnologia convencional de turbinas de eixo horizontal. A primeira vantagem é que a substituição da torre por cabos de comprimento variável permite ao dispositivo operar em altitudes mais elevadas, onde os ventos tendem a soprar mais consistentemente e a uma velocidade maior, caracterizando, portanto, um potencial energético maior. A segunda vantagem é uma redução substancial nos custos do empreendimento, especialmente nos quesitos de transporte e instalação, devido à ausência de uma torre que deva suportar o torque causado pela operação da turbina. Assim, acredita-se que a fundação para o ponto de ancoragem do sistema também se torna mais simples e barata. Os dispositivos de AWE que mantêm-se em voo através de forças aerodinâmicas são denominados de "aerofólios cabeados". Várias estruturas com aerofólios cabeados já foram propostas, dentre as quais destaca-se o *pumping kite* por ser uma das mais simples e de menor custo. O *pumping kite* consiste, essencialmente, de duas unidades – uma de solo e a outra, de voo – com possíveis variações quanto ao tipo de aerofólio (rígido ou flexível), número e função dos cabos, atuadores para controle de voo no solo ou junto ao aerofólio, etc. Em uma das configurações mais usuais, tem-se uma máquina elétrica no solo acoplada a um carretel através de uma redução mecânica. À medida em que o aerofólio descreve uma trajetória que visa maximizar a força de tração no cabo, este desenrola-se do carretel, fornecendo potência mecânica à máquina elétrica que, nessa fase, opera como gerador. Quando o comprimento de cabo atinge um valor pré-determinado, encerra-se a fase de tração e inicia-se a fase de recolhimento, durante a qual a máquina elétrica opera como motor para enrolar o cabo até seu comprimento inicial. Para isto o aerofólio é reconfigurado para uma condição de baixa força aerodinâmica, permitindo o recolhimento com um pequeno gasto energético e, assim, aumentando a potência média entregue à rede (potência de ciclo) ao final deste ciclo com duas fases. A unidade de voo é composta essencialmente pelo aerofólio, por um microcomputador embarcado e pelos atuadores de controle de voo. Esta tese visa contribuir à área de AWE em quatro diferentes aspectos. O objetivo é servir tanto como um documento para o leitor leigo interessado no assunto e que tenha conhecimentos em física, aerodinâmica, sistemas dinâmicos, con-

trole clássico e otimização, bem como uma referência para especialistas que estejam buscando avançar em qualquer uma destas frentes. A primeira contribuição é a discussão em detalhes de alguns modelos importantes usados para a simulação, análise e projeto de controladores de voo para aerofólios cabeados. Dentre estes modelos está o aerofólio ponto de massa com dois cabos, cuja construção é explicada passo-a-passo, incluindo a proposição de pequenas modificações relativas ao efeito da massa dos cabos nas equações de movimento. Em seguida também é feita a derivação do modelo que representa a dinâmica do ângulo de curso ("ângulo de giro") do aerofólio, que é uma variável frequentemente utilizada para o controle de voo. Um terceiro modelo discutido é o modelo logarítmico que descreve a variação da intensidade média do vento de acordo com o coeficiente de rugosidade do solo. Para fins ilustrativos, o modelo foi interpolado para algumas localidades com base em um banco de dados norte-americano aberto ao público. A segunda contribuição desta tese é um estudo comparativo sobre abordagens para controle de voo em uma topologia decentralizada, na qual as leis de controle da unidade de solo e de voo são computadas separadamente. O controle de voo utiliza uma estratégia com duas malhas em cascata. Durante a fase de tração, uma opção é a malha externa utilizar a lemniscata de Bernoulli como referência para a trajetória de "oito deitado" desejada para o voo do aerofólio. Com base no erro de seguimento da lemniscata, é gerada uma referência para o ângulo de curso, que é repassada à malha interna. Já para a fase de retração, a referência do ângulo de curso é mantida apontando para o zênite, fazendo com que o aerofólio saia da zona de potência (condição de vento cruzado, *crosswind*) e possa ser recolhido com baixo gasto energético. Uma outra possibilidade discutida, mais simples, é o uso de apenas dois pontos de atração (atratores) como referência de posição do aerofólio na malha externa, com apenas um dos atratores ativo. Assim que o aerofólio cruza a coordenada azimute de um atrator, o outro torna-se o ativo, levando o aerofólio a executar uma curva e, dessa forma, realizar a trajetória desejada de oito deitado. Devido à descontinuidade no erro de seguimento quando chavea-se entre os atratores, ocorre uma descontinuidade no sinal de controle, razão pela qual esta estratégia é conhecida como "*bang-bang*". É discutido como o *bang-bang* pode ser vantajoso no caso de aerofólios cabeados com um curto perímetro (comprimento de arco) da trajetória, situação em que o período de amostragem do controle torna-se relativamente grande, o que dificulta a estabilização do controle. Por outro lado, no caso de trajetórias com perímetro maior, a ausência de um percurso bem definido entre os dois atratores pode resultar em uma trajetória aproximadamente geodésica ("reta" angular), afastando-se, assim, das trajetórias ótimas de oito deitado sugeridas na literatura. Neste caso, a opção com a lemniscata de Bernoulli pode tornar-se vantajosa. Para a malha interna

do controle de voo também foram investigadas algumas alternativas, entre as quais um controlador proporcional. Usando o modelo da dinâmica do ângulo de curso linearizado em alguns pontos principais, é computado o intervalo do ganho proporcional que garante estabilidade em malha fechada, supondo conhecidos os parâmetros do modelo. Também com base no mesmo modelo do ângulo de curso, projetou-se um controlador de realimentação linearizante que impõe uma dinâmica estável de primeira ordem ao erro de rastreamento da malha interna. Tal controlador linearizante requer, em sua lei de controle, o conhecimento da derivada da referência do ângulo de curso. Dado que esta derivada pode ser difícil de se obter, na prática, com baixo ruído, é investigada uma variante do controlador linearizante sem a mencionada derivada. Considerando, para os três controladores, aproximadamente a mesma constante de tempo do sistema em malha fechada, o controlador linearizante completo obteve o melhor desempenho, seguido pelo proporcional, enquanto o linearizante sem derivada da referência do ângulo de curso ficou com o pior desempenho. Uma terceira contribuição ao estudo do *pumping kite* é a formulação de um problema de otimização para um ciclo de operação, considerando-se a topologia de controle decentralizado. Já que a lei de controle de voo é computada separadamente da unidade de solo, é necessário determinar os valores de alguns parâmetros de operação cuja escolha pode ter um impacto significativo na potência de ciclo. Mostra-se como a potência média durante a fase de tração varia em função do ângulo de ataque médio, e como o ângulo de ataque base pode ser determinado para operar-se no ponto de máxima potência. A fase de tração é parametrizada em termos de um ângulo de ataque base, uma velocidade de desenrolamento, um ângulo polar médio da trajetória, e um comprimento médio do cabo. Já a fase de retração é parametrizada por meio de dois coeficientes que definem a inclinação das rampas de força de tração e ângulo de ataque base, e dois patamares ao final destas rampas. São consideradas restrições no mínimo ângulo de ataque – importante no caso de aerofólios flexíveis – e na máxima velocidade de enrolamento alcançada pela máquina elétrica. A ideia é reduzir a força de tração e o ângulo de ataque do aerofólio enquanto a velocidade de enrolamento aumenta e, dessa forma, obter-se uma fase de retração eficiente. Para fins ilustrativos, o problema de otimização é resolvido para os valores de patamar através de uma busca em *grid*, enquanto os coeficientes de inclinação de rampa são definidos de maneira *ad hoc*. Entre as principais conclusões está que, para o aerofólio do tipo *foil (ram-air) kite* com $12\,\mathrm{m}^2$ de área projetada sujeito a um vento nominal de aproximadamente $10\,\mathrm{m/s}$, ao desenrolar-se o cabo a $2.3\,\mathrm{m/s}$, o que corresponde a uma redução de $25.8\,\%$ com relação à velocidade que maximiza a potência na fase de tração, obtém-se um acréscimo de $9.3\,\%$ na potência de ciclo. Com base em um método simplificado para cálculo da potência de ci-

clo, também é obtida a curva de potência do *pumping kite*, discutindo-se as suas distintas regiões de operação. A última contribuição desta tese refere-se à interpretação dos aerofólios cabeados como um caso específico do "disco atuador" considerado na derivação do limite de Betz para extração de potência do vento. No caso do disco atuador, a potência extraída é abstraída como o produto entre o empuxo sofrido pelo disco e a velocidade do vento atravessando o disco. No caso da turbina eólica de eixo horizontal, a potência dá-se pelo produto entre o torque no disco e a sua velocidade angular. Já no caso do modo de sustentação de Loyd (a fase de tração do *pumping kite*), a potência decorre do produto entre o empuxo no disco e a velocidade de translação do disco no sentido do vento (velocidade de "desenrolamento"). Finalmente, no caso do modo de arrasto de Loyd (turbina acoplada ao aerofólio cabeado), a potência aproveitada surge do produto entre a velocidade tangencial do disco e a força de arrasto (empuxo) sofrida pela turbina. A tese é concluída com a formulação da expressão do coeficiente de potência para o modo de sustentação de Loyd, evidenciando-se o problema do cálculo dos fatores de indução axial, radial, e o ângulo de ataque parcial para cada anel do disco.

Palavras-chave: Energia eólica aérea. Modelagem. Controle de voo.

LIST OF FIGURES

LIST OF TABLES

LIST OF ABBREVIATIONS AND ACRONYMS

GHG	Greenhouse Gas
WEPD	World Energy Primary Demand
AWE	Airborne Wind Energy
KSU	Kite Steering Unit
SISO	Single-Input Single-Output
SIMO	Single-Input Multiple-Output
MIMO	Multiple-Input Multiple-Output
LEI	Leading-Edge Inflated
FSI	Fluid-Structure Interaction
NMPC	Non-linear Model Predictive Control
LIDAR	Light Detection and Ranging
LQR	Linear-Quadratic Regulator
GPS	Global Positioning System
CFD	Computational Fluid Dynamics
BEM	Blade Element Momentum

LIST OF SYMBOLS

C_f capacity factor of a wind power device, [*dimensionless*]

ρ air volumetric density, [kg/m^3]

T (total) tether traction force, [N]; kinetic energy, [J]; thrust force, [N]

v_w wind speed relative to the ground, [m/s]

v_a apparent (effective) wind speed, [m/s]

v_k wing velocity relative to the ground, [m/s]

$v_{k,\tau}$ tangent wing velocity relative to the ground, [m/s]

v_t tether reel-out speed, [m/s]

D , F_D aerodynamic drag force, [N]

C_D aerodynamic drag coefficient, [*dimensionless*]

P power, [W]; or apparent force, [N]

θ wing polar angle, [rad]

θ_T twist angle of the blade section, [rad]

θ_p pitch angle of the blade section, [rad]

$\theta_{p,0}$ pitch angle of the blade (root section), [rad]

ϕ wing azimuth angle or angle of the relative (apparent) wind, [rad]

r tether length or radial length, [m]

L , F_L aerodynamic lift force, [N]

C_L aerodynamic lift coefficient, [*dimensionless*]

F_T tangent force to the disc ring section, [N]

F_N normal force (thrust) to the disc ring section, [N]

Δl steering input of the wing, [m]

α_0 base angle of attack (de-powering input of the wing), [rad]

$\Delta\alpha$ partial angle of attack, [rad]

α angle of attack, [rad]

E aerodynamic efficiency (glide ratio), [*dimensionless*]

n_t number of tethers of significant length, [*dimensionless*]

ψ roll angle induced by steering, [rad]

w_s wingspan, [m]

ρ_t tether volumetric density, [kg/m^3]

d_t tether diameter, [m]

m_t total tether mass, [kg]

g	Earth's gravitational acceleration constant, [m/s^2]
G	Earth's gravity force, [N]
V	kinetic energy, [J]
$C_{D,t}$	tether drag coefficient, [*dimensionless*]
A	projected wing area or cross-sectional swept area, [m^2]
γ	flight course angle, [rad]
f	reel-out factor, [*dimensionless*]
C_R	aerodynamic coefficient of the airborne subsystem, [*dimensionless*]
C	net aerodynamic coefficient for power generation, [*dimensionless*]
a_l	focus of Bernoulli's lemniscate, [rad]
θ_l	polar coordinate of the center of Bernoulli's lemniscate, [rad]
ω_l	angular coordinate of Bernoulli's lemniscate, [rad]
r_l	radial coordinate of Bernoulli's lemniscate, [rad]
c_s	steering coefficient of the turning rate law, [rad/(m·s)]
c_g	gravitational coefficient of the turning rate law, [rad/s]
c_a	coefficient of apparent forces of the turning rate law, [rad/s]
k_p	proportional gain of the course angle control, [m/rad]
δ	(inverse) gain of the lemniscate-based trajectory control, [rad]
p	pole of a dynamic linear(ized) system, [s^{-1}]; pressure, [N/m^2]
e_γ	course angle control error, [rad]
r_d	winch drum radius, [m]; distance between kite and lemniscate, [rad]
$\mathbf{r}_k$	kite position vector in the lemniscate frame, [*dimensionless*]
$\mathbf{r}_r$	wing velocity reference vector in the lemniscate frame, [*dimensionless*]
J_d	drum moment of inertia of the ground winch, [kg·m^2]
κ	gearbox transmission ratio ($1 : \kappa$) of the ground winch, [*dimensionless*]
J_e	electric machine moment of inertia of the ground winch, [kg·m^2]
m	combined wing and control pod mass, or airflow mass, [kg]
m_{eq}	equivalent mass of the airborne dynamics, [kg]
m_{tan}	tangential mass of the airborne dynamics (replaces m_{eq}), [kg]
m_{rad}	radial mass of the airborne dynamics (replaces m_{eq}), [kg]
c_α	(de-)powering rate of change, [rad/s]
c_T	traction force rate of change, [N/s]
U	wind speed relative to the ground, [m/s]
a	axial induction factor, [*dimensionless*]

a'	radial induction factor, [*dimensionless*]
C_P	power coefficient, [*dimensionless*]
C_T	thrust coefficient, [*dimensionless*]
Ω	angular speed of the blade/wing, [rad/s]
ω	angular speed of the wind induced by the blades/wing, [rad/s]
λ	tip speed ratio, [*dimensionless*]
λ_r	local speed ratio, [*dimensionless*]
R	radius of the actuator disc or turbine rotor, [m]
Q	torque, [$\text{N} \cdot \text{m}$]
B	number of blades, [*dimensionless*]
c	airfoil chord length, [m]
σ'	airfoil local solidity, [*dimensionless*]
$(\mathbf{x}_n, \mathbf{y}_n, \mathbf{z}_n)$	orthonormal base of the nominal wind coordinate system
$(\mathbf{e}_\theta, \mathbf{e}_\phi, \mathbf{e}_r)$	orthonormal base of the local coordinate system
$(\mathbf{x}_a, \mathbf{y}_a, \mathbf{z}_a)$	orthonormal base of the apparent wind coordinate system
$(\mathbf{x}_b, \mathbf{y}_b, \mathbf{z}_b)$	orthonormal base of the body coordinate system

NOTATION

- scalars are represented in Roman font: y.

- vectors are represented in lower-case bold face: $\mathbf{x}$.

- matrices are represented in upper-case bold face: $\mathbf{R}$.

- whenever there is a scalar and vector variables of same symbol, then it means that $x = \|\mathbf{x}\|$ is the Euclidean norm of $\mathbf{x}$.

- $\mathbf{x} \cdot \mathbf{y}$ and $\mathbf{x} \times \mathbf{y}$ are the dot (scalar) and cross (vector) products of $\mathbf{x}$ and $\mathbf{y}$, respectively.

- the transpose of $\mathbf{x}$ is $\mathbf{x}'$.

- $\mathbf{v}_{k,[n]}$ represents vector $\mathbf{v}_k$ in the coordinate system of subscript $_{[n]}$.

- the 1ˢᵗ and 2ⁿᵈ time-derivatives of variables are represented by $(\dot{\cdot})$ and $(\ddot{\cdot})$, respectively.

- the $\mathrm{d}(\cdot)$ operator applied to a variable (function), as e.g. $\mathrm{d}P$, represents an infinitesimal share of the total (integrated) value of the variable.

CONTENTS

1 INTRODUCTION

Energy is a primary resource for any living being, including us, humans. The energy needed to keep our bodies working comes from the food we digest, but our energy needs are far from stopping there. As Harari (2015) puts it, the history of humankind is the history of energy. Since primordial times, our societies have always relied on energy sources which, until three centuries ago, were mainly wood, the flow of water and the wind. Mechanical power, mostly for agriculture, transportation and building, was obtained essentially through human and animal labor. However, after the Industrial Revolution was consolidated in continental Europe around the year 1840, energy consumption levels rapidly increased all over the world. This was only possible because new and more abundant sources started to be tapped: the fossil fuels, namely coal, oil and gas.

Nowadays, the energy demand of our industrialized modern societies are orders of magnitude greater than prior to the Industrial Revolution, and energy is needed in the most various sectors. For instance, mechanized agriculture allows the production of food to sustain a world population of nearly 7.5 billion people at the end of 2015. All kinds of heavy-duty machines, mostly oil-powered, are used for the construction of buildings and roads. The expansion of human population also increases the need for a wider and more complex transportation network; not only for people, but also for goods. A growing fleet of commercial ships and airplanes, again mostly oil-powered, daily crosses our oceans and skies. Every now and then new roads and railways are being built, or their capacity is being expanded. Gas is usually burned to produce heat for our homes and buildings in high-latitude areas, whereas in low latitudes, air-conditioning (cooling) devices run on electricity. This energy type is actually converted from other types, depending on the location and availability of resources, as e.g. from the hydraulic power of dams, nuclear power plants through the fission of atoms, the burning of coal and gas, as well as from on- and off-shore wind turbines. Electricity, for being an energy type easily transportable in high quantities, lightens up our expanding metropolitan areas, powers our communication networks, hospitals, industries, schools and so on.

It is hard to think of any aspect of our modern lives in which energy is not fundamental. In fact, we usually only come to realize how dependent we are on the constant and widespread availability of energy, especially electricity, when a blackout occurs, for instance. It is precisely the acknowledgment of how dependent our modern lives are on energy that lays out one of the bases on which our governmental policies are formulated, since less energy

means more costs and therefore less consumption, comfort, production, investments, innovation and jobs – not necessarily in this sequence. Ultimately, our socio-economical de-facto system of nowadays, based on capitalism, relies on a continuously expanding energy offer to keep working. Nonetheless, a growing number of evidences suggests we have reached a point beyond which keeping the same energy paradigm based on fossil fuels will in fact turn the tide and work against us, our expansion and welfare. Simply put, our activities since the Industrial Revolution appear to have triggered, or at least significantly contributed to a process of global warming and, in turn, climate change. This threatens human populations and biodiversity, in general, all over the planet. If so, how to fight this trend while ensuring the needed energy to power the world?

Although nowadays the usual opinion is that the rapidly changing climate is due to human interference in the natural processes, there is still debate about it. For being a non-renewable energy source, fossil fuels have supplies which are limited, and therefore it is a matter of time until we will have to make a transition into an energy grid based on other sources in any case.

1.1 MOTIVATION

Considering that the world population and economy are expected to continue growing in the near future, there is an evident need to further expand the energy offer. This should incorporate sources which are not only economically attractive, but also environmentally sustainable, if possible. The answer lies in fostering the use of *renewable energies* (*"renewables"*). This term refers to a heterogeneous class of technologies, each with its distinct characteristics, among which we can mention the

- source type – wind or water flow, heat from the Earth (geothermal) or directly from the Sun, burning of hydrocarbons from biomass, etc;

- deployment concentration – decentralized topology in small plants, centralized topology in large plants;

- energy output flow – variable and unpredictable, variable but predictable, constant, uncontrollable, etc;

- environmental impact – visual, audible, land or water pollution;

- social impact – for instance, by depreciation of neighboring inhabited areas, or even by displacement of local populations.

So far, the main types of renewable energy technologies commercially deployed in large scale can be classified as biomass, direct solar, geothermal, hydropower, ocean, and the *wind energy*. An innovative approach to harvest the wind energy is the subject of the contributions in this dissertation.

1.1.1 Climate change mitigation

According to the Intergovernmental Panel on Climate Change (IPCC, 2014), one of the main worldwide organizations to investigate the topic, "human influence on the climate system is clear, and recent anthropogenic emissions of Greenhouse Gases (GHGs) are the highest in history. Recent climate changes have had widespread impacts on human and natural systems." Some of the direct impacts are the increase in the global average surface temperature and in the sea level, whose trends are shown in Fig. 1.

Figure 1 – Climate change effects relative to the average over the period between 1986 and 2005. Colors indicate different data sets.
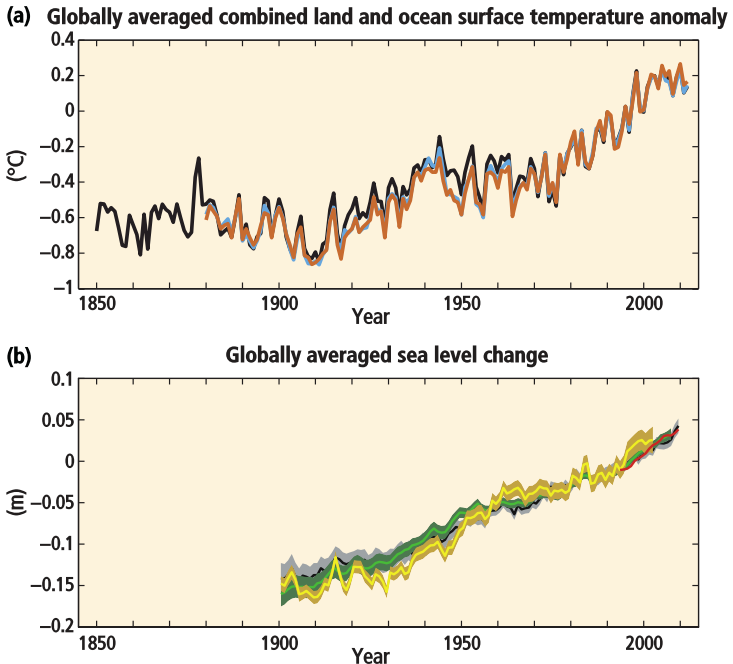
Source: IPCC (2014)

Climate change can be verified in many more aspects of the global weather and biosphere. As an example, some of the CO_2 emissions are absorbed by the ocean, resulting in acidification. Estimates are that the ocean surface water pH has decreased by 0.1, corresponding to a 26 % increase in acidity. The arctic ice sheet has been retreating with a rate between 3.5 % to 4.1 % per year since 1979. Many terrestrial, freshwater and marine species have shifted their habitats and migration patterns. Citing again IPCC (2014), "changes in many extreme weather and climate events have been observed since about 1950. Some of these changes have been linked to human influences, including a decrease in cold temperature extremes, an increase in warm temperature extremes, an increase in extreme high sea levels and an increase in the number of heavy precipitation events in a number of regions."

Supported by studies as the one previously mentioned, a growing number of nations has been joining a collective effort to reduce the emissions of GHGs in an attempt to alleviate some aspects of climate change. Halting this process is often already considered unattainable: even if GHG emissions were completely eliminated today, the associated impacts would continue for centuries. For instance, the surface temperature and the sea level are expected to continue rising, although at different rates, in various emission scenarios. However, if the emissions continue at the current pace, the negative impacts could be even higher, since the risks of abrupt or irreversible changes increase with the average global temperature. Therefore actions still can be taken to avoid further damage, which brings us to the question: where to cut off GHG emissions? To answer this let us take a look at Fig. 2, where the contributions of the different gases to the total emissions are shown.

The fluorinated gases covered under the Kyoto protocol (F-gases) corresponded, in 2010, to only 2 % of the total emissions, while 6.2 % were nitrous oxide (N_2O), 16 % were methane (CH_4), 11 % were carbon dioxide from forestry and other land uses (CO_2 FOLU), and 65 % were CO_2 from fossil fuel combustion and industrial processes. Observe the increasing trend of emissions throughout the latest four decades, with a slight acceleration between the years 2000 and 2010, despite a growing number of climate change mitigation policies. Moreover, almost two thirds of the emissions come from the burning of fossil fuels. We can observe a high correlation between the rise in the average global temperature and sea level (Fig. 1), and the emissions of GHGs (Fig. 2). The atmospheric concentrations of these gases are currently the highest in at least the latest 800 thousand years. Not coincidentally, anthropogenic emissions of GHGs are considered to be *extremely likely*, as stated by the IPCC (2014), the main driving cause for the observed global warming since the mid-20th century.

Mitigation policies and actions must take into consideration that the

Figure 2 – Total annual anthropogenic emissions of GHGs, in gigatonnes of CO_2-equivalent per year and type of gas.
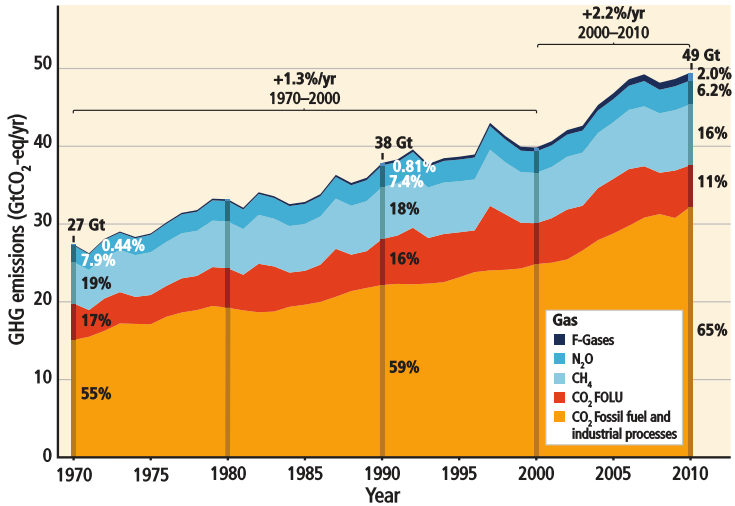
Source: IPCC (2014)

different gas types have distinct lifetimes and heat trapping capacities. For instance, methane, even though having a relatively shorter lifetime of 12 years, is much more efficient in trapping heat than carbon dioxide. The result is a greenhouse impact 25 times greater than CO_2, for the same amount of gas, in a timespan of 100 years. Nonetheless, given the very high share relative to the other gases, the reduction of CO_2 emissions, especially for the purpose of energy generation, must be one of the priorities in the sector policies for the near future. According to the International Energy Agency (IEA, 2013b), "...the energy sector will be pivotal in determining whether or not climate change goals are achieved". It goes on to admit that "...taking into account the impact of measures already announced by governments to improve energy efficiency, support renewables, reduce fossil-fuels subsidies and, in some cases, to put a price on carbon, energy related CO_2 emissions still rise by 20% to 2035. This leaves the world on a trajectory consistent with a long-term average temperature increase of 3.6°C, far above the internationally agreed 2°C target". This means more effort is necessary, both in technological innovation and policies for the energy sector, in order to make the 2°C target feasible.

Let us now check the outlook for the expansion of the energy grid in a global scale, and the role that renewable sources are expected to play.

1.1.2 Expansion of the energy offer

The IEA is an autonomous organization that seeks to promote energy security to its member states through detailed research and analyses. It publishes on an annual basis the *World Energy Outlook*, a report intended to shed some light on how the energy sector is expected to evolve in the coming decades. We will now refer to the report (IEA, 2013b), in which three scenarios are considered. The *Current Policies Scenario* takes into account only those policies and measures formally adopted as of mid-2013. It basically assumes that the governments do not implement any recent commitments that have yet to be backed-up by legislation, nor introduce any significant changes in the policies applied so far. The *New Policies Scenario* incorporates the policies and measures that affect energy markets and that had been adopted as of mid-2013, including initiatives and commitments announced to support renewable energy and improve energy efficiency, promote alternative fuels and vehicles, carbon pricing, reform fossil-fuel subsidies, etc. At last, the *450 Scenario* represents the actions needed to set the global energy sector on a course compatible with a near 50% chance of limiting the long-term increase in the average global temperature to 2°C.

A very common term in the energy sector is the World Energy Primary Demand (WEPD), also known as the *total primary energy supply*: it refers to the amount of energy extracted by all of human civilization to fulfill its needs. It differs from the energy actually spent (consumed) because of the losses caused by transformation of energy from one type to another until its end use. The evolution of the WEPD and related CO_2 emissions for each of the IEA mentioned scenarios is shown in Fig. 3. Observe that, in all cases, the demand increases by the year 2035, pushed by a growing population and expanding economies, but governmental policies have a crucial rule in determining the pace. In the Current Policies Scenario, the WEPD increases more, to a level about 45% higher than in 2011. This is equivalent to adding the combined energy demand, as of 2013, of China, the USA and India – the world's largest energy consumers. In the New Policies Scenario, the WEPD grows to 33% by 2035, with a faster rate of 1.6% per year until 2020, and 1% per year thereafter. Such deceleration is expected to happen because of a gradual slowdown in economic growth, especially in the developing economies that are under rapid industrialization, as well as a reaction to the introduction of more climate-friendly energy policies and the increase in the overall energy efficiency. In the ideal case of the 450 Scenario, the increase in the WEPD is only of 14% by the year 2035.

In all three scenarios the energy demand will increase, and it will have to be met by an increase in the energy offer as well. The question is: how

Figure 3 – Projected evolution of the WEPD (left) and corresponding CO_2 emissions (right).
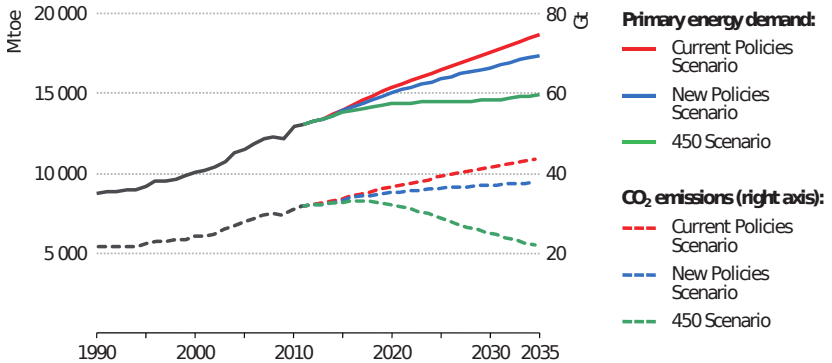
Note: Mtoe = Million tonnes of oil equivalent; Gt = gigatonnes.
Source: IEA (2013b)

will the different sources contribute to the total expected demand? The projections of the IEA in this regard are shown in Fig. 4. Observe that the use of coal may suffer a strong variation by 2035, depending on the considered scenario: the coal share in the WEPD will lie in the interval between 17 % and 30 %. Coal and oil are the two sources which may actually have a reduction in the usage; all other sources are expected to be more exploited. As of 2011, the share of renewable sources in the energy mix was relatively small, about 13 %. By 2035, in the Current Policies Scenario this share remains more or less the same, at 14.6 %, while increasing to 17.6 % in the New Policies Scenario, and practically doubling, at 26.3 %, in the 450 Scenario. Note that the extraction of hydropower will not vary much, nor will its share in the WEPD. One of the reasons for this is that the potential for power generation of the main river basins, mostly concentrated in a few countries as China and Brazil, are already almost fully exploited. More than with nuclear power, the biggest uptake is to occur with bioenergy (biomass) and other renewable sources, including solar and wind energy. Their attractiveness, however, will depend on governmental policies and incentives, higher fossil fuel prices, and technological advances to reduce costs.

According to the IEA (2013b), fossil fuel subsidies worldwide in 2012 were estimated to a total of US$ 544 billion, whereas subsidies to renewable energies, aiming to improve their competitiveness, reached US$ 101 billion at the same year, only about a fifth of the subsidies for fossil fuels. While renewables such as hydropower and geothermal have long been economical in

Figure 4 – Projections of the WEPD according to: the Current Policies Scenario (CPS), the New Policies Scenario (NPS), and the 450 Scenario (450).

(a) Change, relative to the period between 2011 and 2035.
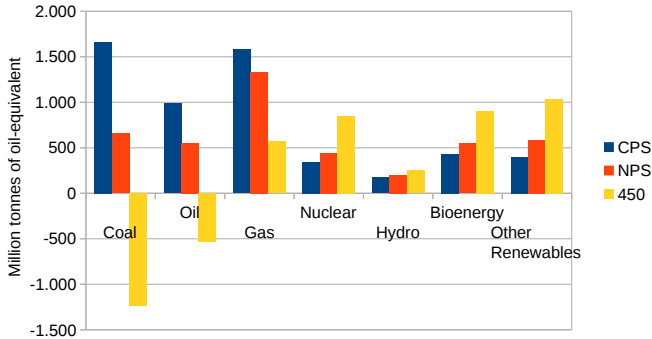
(b) Composition, in 2035.
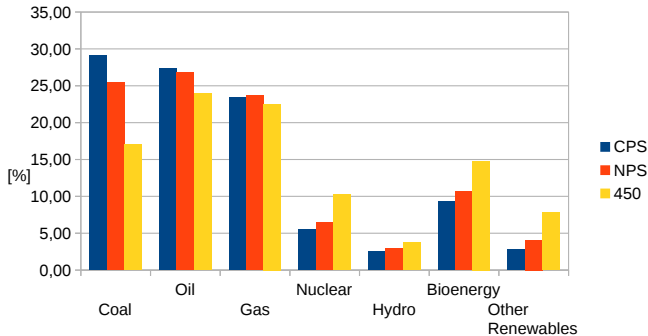
Source: IEA (2013b)

many locations, solar and wind power (especially off-shore wind) still require financial support for their dissemination in many countries. The projections of the New Policies Scenario in Fig. 4 consider that subsidies to renewable energies will grow to around US$ 220 billion in 2035.

Regarding wind energy specifically, the IEA (2013b) reports a growth of around 25 % per year over the past decade, reaching an installed capacity of 282 GW in 2012, which corresponded to 2.3 % of the global power (electricity) generation at that time. China has been leading this recent expansion, with 13 GW added to the grid in 2012, followed by the USA and the European Union, with 12 GW each. Off-shore wind had the highest capacity addition in

one year, reaching 5.4 GW in 2012, mainly due to new installations in Europe, in the North Sea. In the New Policies Scenario, wind-based electricity generation is expected to increase at an average rate of 6 % per year until 2035, when its share of the global electric power supply should reach 7.5 %, with a total capacity of 1,300 GW. Around 80 % of the added capacity is expected to be on-shore, and China will overtake the European Union with the largest share of wind power plants, as shown in Fig. 5.

Figure 5 – Installed wind power capacity, by region, in the New Policies Scenario.
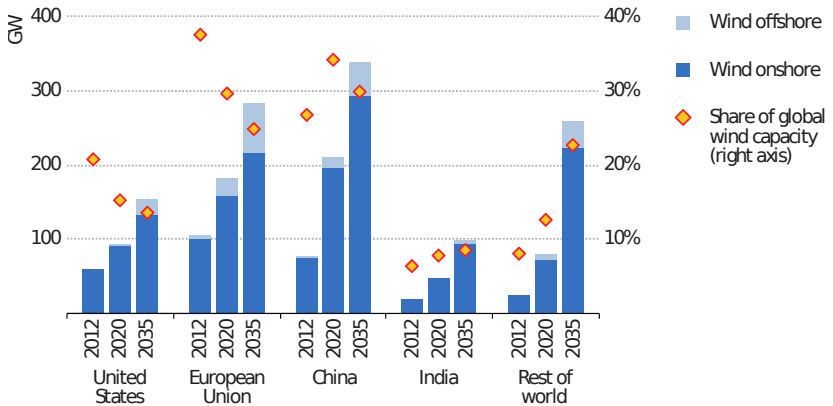
Source: IEA (2013b)

An important aspect of a wind turbine – as any device harvesting the wind power – is its capacity factor C_f, i.e. the average power produced over a period of time with respect to the device rated power. Regarding on-shore wind farms, the capacity factor in recent years has lied typically in the range from 20 % to 35 %, reaching up to 45 % or more in excellent sites (IEA, 2013b). For off-shore installations, the C_f is usually higher due to more consistent sea breezes, varying between 30 % and 45 %. Despite these advantages, the installation of off-shore wind farms tends to be more expensive because of the high complexity for building the underwater foundations and establishing the grid connections.

Brazil is one of the countries with very favorable conditions for wind power. According to a report from the Global Wind Energy Council (GWEC, 2011), considering the recent technological advances, the Brazilian wind power potential is estimated at 350 GW. The northeast region alone is responsible for more than 50 % of such potential. However, in a more recent report (GWEC, 2014) it was claimed that a potential of 240 GW at 150 m altitude

for areas with wind faster than 7 m/s was found in the southern state of Rio Grande do Sul. These estimates are based on the current wind turbine technology. At the end of 2014, Brazil had a total installed capacity of 5.9 GW, responsible for 4.3 % of the electricity generation in the country. The Brazilian government's Decennial Energy Plan sets a goal to produce nearly 12 % of the electric power in the grid from the wind by 2023. The New Policies Scenario of the IEA (2013b) is more conservative, though, projecting about 9 % of the country's electricity from the wind by 2035.

1.2 EVOLUTION OF WIND ENERGY TECHNOLOGY

Wind energy has been known to humankind since ancient times and has been used for the generation of mechanical power, for instance, in windmills. However, it was only in the late 1960s that it started to draw commercial attention for the generation of electricity. To understand how the technology reached the current level of development, let us recall some milestones throughout its history, compiled from Manwell, McGowan and Rogers (2009).

The oldest reference to a wind harvesting device belongs to Hero of Alexandria, believed to have lived around the dawn of the 1st century. His *pneumatics* device was similar to a horizontal-axis windmill, and it was used to pressurize air into an organ (musical instrument). The next reference dates from the 9th century, when vertical-axis windmills driven by drag forces were in use in the Persian region of Seistan, now eastern Iran. The first occurrence of windmills in Europe was recorded in England, in the 12th century. The idea may have been introduced by the Vikings, who regularly traveled to the Middle East, but the English concept was significantly different from the Seistan one: the rotor axis was horizontal, and it was driven by lift forces. These windmills spread through northern Europe and were used to provide mechanical work for tasks like water pumping, grain grinding and wood sawing. They usually had four blades, and were built on posts which could be turned to face the prevailing wind direction.

In those early stages of wind energy technology, the design of windmills was mostly empirical and limited by building constraints. For instance, the amount and size of the blades were influenced by the ease of construction, and the ratio of blade area to swept area was empirical. In the 18th century, an important step towards the scientific development of windmills was taken by Englishman John Smeaton. Basically, he came to the conclusion that the speed of the blade tips was ideally proportional to the wind speed, the maximum torque was proportional to the square of the wind speed, and the

maximum power was proportional to the third power of the wind speed.

After the early decades of the 19th century, the use of windmills started to retreat, mainly because of competition with the newly introduced fossil fuels. For instance, coal and oil could be easily transported everywhere, and could be stored as well – features that did not apply to the wind. However, right before their demise, European windmills had achieved a high level of sophistication when compared to Hero's pneumatics, for instance. The power output of some machines could be controlled by an automatic system, a forerunner of James Watt's approach to steam engines. The windmill was equipped with a fly-ball subject to the centrifugal force caused by the rotor speed and connected to the upper millstone of the windmill grain inlet. If the speed increased (due to a stronger wind), the radius of the fly-ball trajectory would increase as well, pulling up the upper millstone away from the lower one, thus allowing more grain into the grinding chamber. This means more load was added to the machine and thereby the increase in the rotation could be contained to a level that maximized the power.

As soon as the early electrical generators were invented, at the end of the 19th century, there were attempts to power such machines with a windmill rotor. In the USA, some pioneers in the field were Charles Brush and Marcellus Jacobs. The device later known as the "Jacobs turbine" had an horizontal axis rotor driven by three blades forged with a true airfoil shape, beginning to resemble the turbines of today. Moreover, it was coupled to a complete, residential scale power system, including batteries for energy storage. In Denmark, between 1891 and 1918, Poul La Cour built more than 100 electricity generating turbines with rated power ranging from 20 kW to 35 kW. Instead of storing energy in batteries, La Cour used the electricity to produce hydrogen, which was later used as fuel for lighting purposes. Back to the USA, a milestone was achieved when the Smith-Putnam machine was built, in the late 1930s. It was the largest wind turbine so far, with a 2-bladed rotor 53.3 m wide (in diameter) and with a rated power of 1.25 MW. The turbine turned out to be too large for the level of understanding in wind engineering at that time, suffering a blade failure in 1945, which caused the project to be abandoned. The next important technological advancement came right after World War II, when Johannes Juul built the 200 kW Gedser turbine, in Denmark. Its innovation was twofold: the use of aerodynamic stall to control the power, and the use of an induction generator (squirrel cage type) instead of a synchronous machine, which was the convention at the time, allowing for an easier connection to the grid.

The development of the wind energy industry started to pick up pace in the late 1960s. It was when the first real environmental concerns about the industrial development, unconstrained use of fossil fuels and the poten-

tial danger of nuclear energy started to draw public attention. A couple of years later came the oil crisis in the USA, in the mid-1970s. This fostered the deployment of turbines ranging from 100 kW to 3.2 MW, whose operation provided valuable research data but did not lead to commercial endeavors at first. The big opportunities in the USA came in the late 1970s, and soon the so-called "California wind rush" was taking place. In the early 1980s, the installed capacity in California had reached 1.5 GW. After that, governmental policies changed in the USA and the "wind rush" collapsed, causing many local manufacturers to go out of business. In the 1990s, the focal point of wind turbine manufacturing turned to Europe, especially Denmark and Germany. Since then, the wind energy industry suffered an accelerated expansion which lasts until today. Both for on- and off-shore applications, the power output of wind turbines has been steadily increasing, with larger rotors being built on top of taller towers in order to tap into stronger winds, farther from the ground. Fig. 6 illustrates the growth in size of the turbines along the years.

Figure 6 – Evolution of the size and rated power of wind turbines.
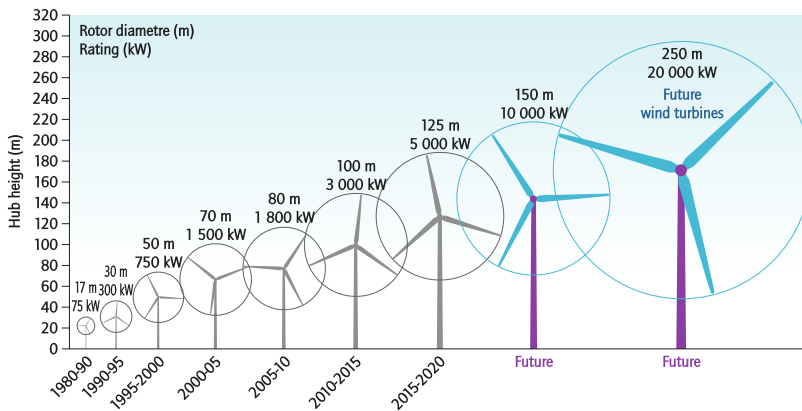
Source: IEA (2013a)

High-altitude winds are usually not only faster than those close to the surface, but also tend to blow more constantly – in other words, more often. As a consequence, a system designed to operate at its rated power at a given wind speed which occurs more often will have a higher capacity factor. In this regard, Archer and Caldeira (2009) illustrate very well the advantages of reaching up into higher altitudes. It is well known that the power available in the wind flow is given by

$$P_{\mathrm{w}} = \frac{1}{2} \rho A_{\mathrm{w}} \|\mathbf{v}_{\mathrm{w}}\|^3 , \qquad (1.1)$$

where ρ is the air density and A_w is the rotor swept area perpendicular to $\mathbf{v}_\mathrm{w}$, which is the wind speed vector relative to the ground. Although, in general, the wind speed increases with altitude, the *optimal height* – where the maximum wind speed is verified – varies according to the location considered and may also vary with time, both in short scales, of hours and days, as well as in longer time scales, of months and years. Therefore, more than being able to tap into the wind energy at a fixed altitude, if we could continuously control the altitude of operation of a wind power device, its capacity factor could be even further increased. Considering the wind data collected in the period between 1979 and 2006 – thus filtering out any time variations up to the order of decades – the optimal heights in the world atlas and their respective wind power densities ($P_\mathrm{w}/A_\mathrm{w}$) are depicted in the right and left column maps of Fig. 7, respectively. The indications 50th, 68th, and 95th correspond to the percentage of time in which the corresponding wind speed (represented as power density) was exceeded.

Observe that, if we would like to harness the wind power at a given wind value that is exceeded at least 95 % of the time, the optimal altitudes would be mostly in the range between 500 m and 1.000 m worldwide, well above the current limit of conventional wind turbines. Let us take, for example, the Brazilian northeast region, which is characterized by an excellent wind potential. Along the coastline, in this altitude range, we could reach power densities up to $0.3\,\mathrm{kW/m^2}$. This means hypothetically that, if we were able to deploy in those altitudes one of the largest wind turbines, with rotor diameters about 100 m, we could reach an approximated rated power of 2.36 MW with a capacity factor of at least 95 %, yielding an average produced power, in the considered period, of 2.24 MW. In contrast, let us imagine a turbine with the same swept area, rated power of 3 MW – which is usual for modern turbines this large – and have it operate at the same location, but at only 150 m of altitude. Furthermore, let us consider that such turbine would operate with a capacity factor of 40 % – a high value for current on-shore wind farm standards. In this case, the resulting average power would be 1.2 MW for the same time period, only about half of that obtained in the high-altitude scenario.

Let us now reduce the desired percentage of exceeding the maximum wind speed to 68 %. Further analyzing the Brazilian northeast coastline, the optimal height would then lie between 1 km and 2 km. There we would have even higher power densities, of up to $1\,\mathrm{kW/m^2}$. Now the turbine, hypothetically operating in this altitude range, would reach a rated power of approximately 7.86 MW and, given a (least) capacity factor $C_\mathrm{f} = 68\,\%$, the turbine would yield an average produced power of 5.34 MW. This is already more than 4 times the average power output of the 150 m altitude scenario for the

Figure 7 – Optimal wind power density (left-column maps) and respective optimal height (right-column maps) in which the (maximum) wind speed was exceeded in 50%, 68%, and 95% of the time in the period between 1979 and 2006.
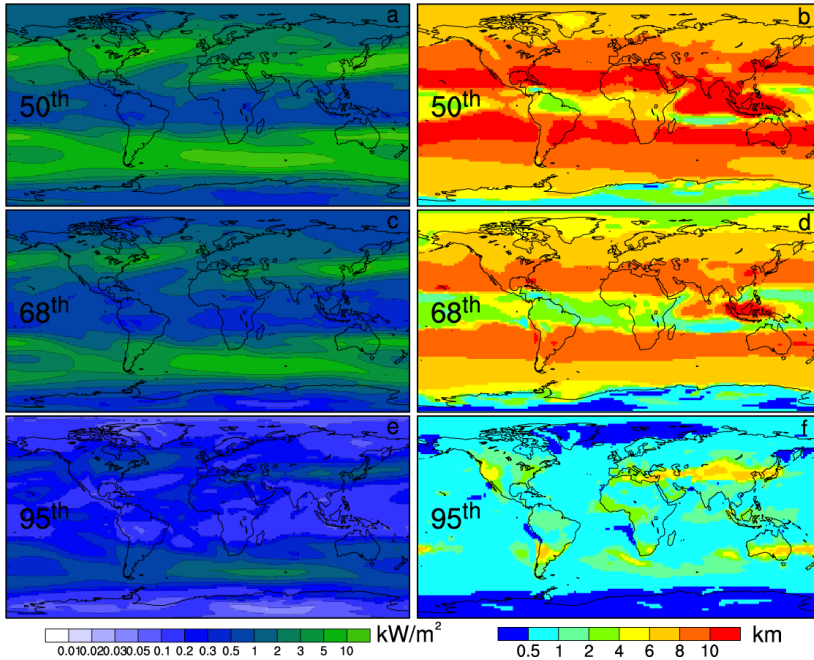
Source: Archer and Caldeira (2009)

same rotor swept area.

      Because the average wind speed tends to increase with the altitude, the trend to build larger and taller wind turbines is well justified, as already discussed. However, as Thresher, Robinson and Veers (2007) pointed out, this continued growth in turbine size is progressively running into tighter economical constraints. The primary argument is the "square-cube-law": the idea is that the power of a turbine increases with the rotor swept area, which is a function of its squared diameter, whereas the volume of material, hence the mass, increases with the cube of the diameter. Consequently, at some point, the cost of a larger wind turbine will grow faster than the power gain obtained. Recent technology advancements have allowed the gain in mass to decrease from the exponent 3 to 2.3, which in turn allowed the turbine rotor diameter to reach about 125 m nowadays, with a rated power about 5 MW. Nevertheless,

further decreases in this exponent towards 2 should be asymptotically harder to achieve.

Another important constraint to conventional wind technology are transportation and installation costs. As the turbine components grow in size, it becomes unfeasible to transport them over cost-effective truck-pulled trailers, whose size is limited by the width of the existing roads. Rail transportation is also dimensionally restricted, when available for the desired destinations in the first place. Assembling structures such as cranes also have a limitation on the size and weight of the lifted material. In summary, further increases in the rated power of wind turbines will probably occur at a lower pace if compared to what it has been so far.

Despite these difficulties, the development of conventional wind energy technology – based on horizontal-axis wind turbines – has continued at a fast pace from 2007 up to now. For instance, the turbine design is being adapted to diverse operating conditions, including icy climates and slower winds. Control systems are becoming more sophisticated, based on more accurate mathematical models, in order to reduce loads and aerodynamic losses. Efforts in the enhancement of wind models are also underway, thus allowing a better predictability and optimization of the power output of wind farms. Stronger and lighter materials are being developed, as well as novel rotor architectures with active blade elements. Hydraulic drive-train designs, replacing the traditional gearboxes, and direct coupling between turbine and generator are being considered as possibilities to reduce losses in the conversion from mechanical to electric energy. Also, new tower materials and foundations for deep water applications are being investigated, aiming at the off-shore sector, where there is a greater potential for cost reductions and technology breakthroughs.

Building on these efforts, the ultimate goal is to further scale up the turbines towards a rated power in the range from 10 MW to 20 MW. However, recalling the square-cube-law previously discussed, we may come to a point in this road to the 20 MW target where further decreases in the system weight, as well as advances in the fronts already mentioned, simply stop making economical sense. Citing again the report from IEA (2013a), "No single element of on-shore turbine design is likely to reduce dramatically the cost of energy in the coming years." Based on this observation, it adverts that "...scaling up turbines to lower costs has been effective so far, but it is not clear the trend can continue forever."

In face of these uncertainties and limitations, we should diversify by also looking into other approaches to harness the wind power available above 200 m, which is the approximate altitude reached by the tips of the current largest rotor blades. Moreover, as importantly as developing the technology to

harness this high-altitude wind energy is making it economically competitive to other energy sources. If we had such alternative, the share of wind energy in the WEPD and electric grid could become even larger, approaching the 450 Scenario of the IEA (see Fig. 4), or perhaps even surpassing it. The solution may consist of a paradigm shift: what if we removed the tower sustaining the rotor and found a way to keep it airborne?

1.3 AIRBORNE WIND ENERGY

In recent years, there has been ongoing research to develop other ways to exploit high-altitude wind energy. One possibility is to replace the rigid, heavy tower by one or more flexible, light-weight tether(s), and have the wind power device redesigned to become extremely light, so that it can be kept aloft either through *aerostatic* or *aerodynamic* lift forces. This is a fundamental characteristic of Airborne Wind Energy (AWE) technology that distinguishes it from conventional wind energy technology.

Systems that rely on the aerostatic lift to fly, as the *aerostat* built by the US company Altaeros Energies, consist essentially of a buoyant device tethered to the ground – usually a helium-inflated balloon – with an on-board horizontal-axis turbine, as illustrated in Fig. 8. The principle of work is the same that applies to conventional tower-based turbines, except that the electric energy is transmitted to the ground through the tether(s). Lifted by the buoyant device, the tether(s) could be reeled out to a very large length in order to reach, in principle, altitudes in the scale of a few kilometers, depending on the tether weight. However, as the wind speed increases, the thrust exerted by the wind upon the turbine and the drag on the balloon and tether(s) would tilt the rotor away from the vertical direction, i.e. bring it closer to the ground by decreasing the elevation angle. Therefore climbing up to very high altitudes with tethered devices using solely the aerostatic lift force, although conceptually trivial, may be challenging to achieve in practice.

The other category of AWE systems utilizes the aerodynamic lift force acting on a tethered wing (airfoil) both to remain airborne as well as to harvest the wind power. These wings can be either flexible, like a power kite, rigid, as an airplane wing, or have intermediate characteristics. Compared to the tethered balloons, the wing-based systems depend on a minimum wind speed at the ground, or on an auxiliary propulsion system, to be launched and landed. On the other hand, tethered wings certainly offer a higher power-to-volume ratio, since the typically helium-inflated balloons must have a high volume in order to generate the needed aerostatic lift to keep the turbine, balloon structure and tether airborne.

Figure 8 – Concept of a buoyant wind turbine.
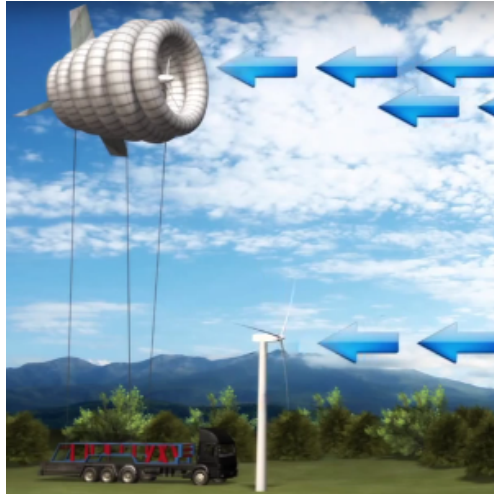
Source: Altaeros Energies

1.3.1 Drag and lift modes of tethered wings

We will show in Sect. 4.3 that the majority of the power extracted from the wind by a horizontal-axis wind turbine comes from the blade part closer to the tip, due to its higher tangential speed. This means that all other components – namely the tower, the nacelle and the blade part closer to the nacelle – are needed basically to support the blade part closer to the tip. So if we could find a way to get rid of all those supporting components and have the remaining blade part – which we will denote from now on as the *wing* – kept airborne through aerodynamic lift, we could extract most of the wind power of the original wind turbine, but with a structure orders of magnitude lighter and thus probably cheaper to construct, transport, install and maintain. Moreover, without the tower constraint, we could fly the wing in higher altitudes, which offers advantages in terms of power density in the wind flow, as already discussed. One way to do this is by tethering the wing to the ground.

Before we continue, let us briefly explain one term very common in the AWE literature: the *crosswind*. It refers to the wind perceived by the airfoil when it flies approximately perpendicular to the nominal wind vector, $\mathbf{v}_w$. This perceived wind, which we name the *apparent (or effective) wind* ($\mathbf{v}_a$), in the crosswind motion can typically reach a magnitude between 5 and 10 times the intensity of $\mathbf{v}_w$, depending on the airfoil aerodynamic efficiency

(glide ratio). Because the aerodynamic forces depend on the square of v_a, and the power is proportional to these forces, crosswind operation can yield up to 100 times more power than when harvesting the power in the nominal wind flow, which is the case, for instance, of the ancient vertical-axis windmills driven by the aerodynamic drag – similar to a waterwheel. Horizontal-axis wind turbines also exploit the crosswind, but the resulting aerodynamic force is used to exert a torque on the rotor. For the case of AWE with tethered wings, the crosswind operation causes the tether traction force T to increase, along with an increase in the apparent wind.

It is usually referred to the work of Loyd (1980) as the "official birth" of modern research with AWE technology based on tethered wings. Loyd proposed two ways to harness the wind energy by a tethered wing flying in crosswind motion: the *lift* and *drag* modes, illustrated in Fig. 9. In the drag mode, the system operates with a tether of constant length, while the power P is harnessed through turbines mounted onto the wing. The product between the apparent wind tangent to the wing position vector, $v_{a,\tau} \approx v_a$ (in the crosswind), and the drag force[1] D_p suffered by the turbines due to their operation gives rise to the mechanical power input to the electric generators connected to the turbines, according to the expression

$$P = D_p v_a. \tag{1.2}$$

Figure 9 – Loyd's AWE drag and lift modes with tethered wings to explore the crosswind.
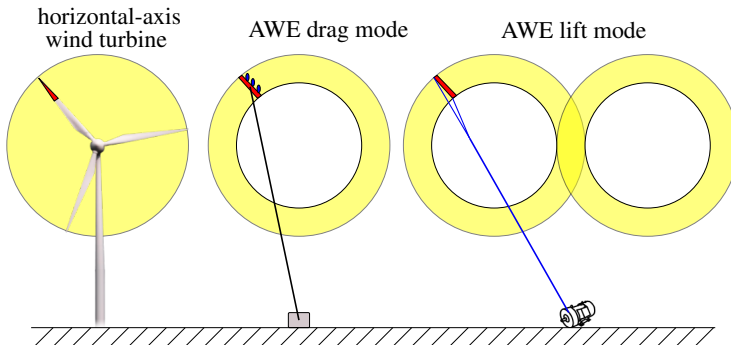
Source: original

---

[1] To be more precise, the turbine disc is subject to a thrust force, in the axial direction, whereas the drag force acting on the turbine blades deviates from the axial towards the radial direction as the blades rotate faster. This is discussed in Sect. 4.3.

The generated electric power is then transferred to the ground by means of electric wires passing through the traction tether, as in the case of the tethered balloon. The maximum power output is obtained when the turbines add an optimal amount of "drag" (thrust), which is half of the drag D_k acting upon the wing:

$$D_p^* = \frac{1}{2} D_k. \qquad (1.3)$$

If more drag is added to the airborne system by the turbines, the effect of slowing down the wing and thus decreasing v_a is stronger, such that product in Eq. (1.2) falls. This is also what happens when D_p is decreased, because the increase in v_a does not occur in the same proportion. The US company Makani Power has already built prototypes for demonstrating the drag-mode AWE concept. The smaller version is 8 m wide and 3 m long in total, produces 20 kW of rated power at 10 m/s of nominal wind speed, and is designed to operate between 40 m and 110 m of altitude, in a circular flight trajectory with a radius of 140 m. The aircraft has 4 turbines mounted onto the main wing, which has a chord length of approximately 60 cm. The company is currently developing its M600 version (see Fig. 10), capable of generating 600 kW through its 8 DC on-board turbines at 11.5 m/s of nominal wind, designed to operate in an altitude range between 140 m and 310 m in a circular trajectory with 145 m of radius.

Figure 10 – Drag-mode AWE system prototype with 600 kW of rated power.

Source: Makani Power

The aloft turbines on a drag-mode system play another role other than

only capturing the kinetic energy from the apparent wind and driving the light-weight, high-speed and directly coupled electric machines as generators. During launch and landing, the turbines act reversely – as engines – being driven by the electric machines, which then operate as motors. Hence the AWE system is able to produce the necessary lift regardless of the wind conditions at the ground level, allowing the wing to hover in the air, similarly to a "drone". This feature is one of the biggest advantages of Loyd's drag-mode machines in comparison to the lift-mode ones, for which the automated tasks of launching and landing are still to be properly solved.

Regarding Loyd's lift mode, the idea is that the tether, of length r, is reeled out at a speed $v_t = \dot{r}$ from a drum on the ground, connected to an electric generator, while the wing flies a trajectory that maximizes the traction force T. As shown in Fig. 9, the flight path has usually the shape of a lying eight in order to avoid accumulated torsion of the tether that would be induced if a circular trajectory were flown[2]. Loyd showed that, if the wing lift coefficient C_L is significantly higher than the wing drag coefficient C_D, the traction force is composed predominantly of the kite lift force L. The mechanical power input to the generator is thus basically dependent on the wing aerodynamic lift, which is the reason behind the name for this configuration:

$$P = T\dot{r} \approx L v_t. \qquad (1.4)$$

Other names found in the literature for the lift mode are *pumping kite* and *yo-yo*. This naming is because, after some time generating energy by means of reeling out, the tether must be wound back onto the drum so that a new generation cycle can begin – hence the "pumping" behavior. The maximum power for the generating phase is obtained if the tether is reeled out at the optimal speed

$$v_t^* = \frac{1}{3} v_w \sin \theta \cos \phi, \qquad (1.5)$$

where θ is the polar (complementary elevation) angle, and ϕ is the azimuth angle of the wing. Starting at v_t^*, if v_t is decreased, T increases in a smaller proportion such that the product in Eq. (1.4) falls. The same happens if v_t is increased, because T falls more strongly. Details on this behavior and the study of a more thorough strategy for optimizing the pumping cycle will be addressed in Sect. 3.2.

A few years ago, Goldstein (2013) devised the configuration shown in Fig. 11. In the notation of his paper, $\mathbf{W_g}$ is the kite velocity, $\mathbf{V}$ is the nominal

---

[2]Observe that, in the drag-mode circular trajectory, the tether would indeed accumulate torsion. Therefore there must be a technological solution similarly to a rescue or fishing swivel, that withstands the high traction force while allowing for the electric current to go through.

wind, **W** is the effective wind, $\mathbf{D_k}$ is the kite drag, **U** is the tether traction force, $\mathbf{D_t}$ is the tether drag, and $\mathbf{F_{w,k}}$ and $\mathbf{F_{w,t}}$ are the kite and tether weight, respectively. The motivation behind Goldstein's concept is that the operation modes studied by Loyd could face technological issues that could render the commercial use of such AWE systems unfeasible. Firstly, regarding the drag mode, the turbines attached to the wing would be significantly heavy, reducing the overall efficiency. Also, the electric power generated would have to be transmitted to the ground through the tether, requiring airborne transformers to increase the voltage as an attempt to reduce the ohmic losses and the conductor cross section. Moreover, these transformers would add undesired airborne weight. The lift mode configuration would also offer its practical drawbacks. For instance, the tether would be reeled out from the drum at a relatively low optimal speed for economically feasible generators, thus requiring a gearbox to amplify the angular speed from the drum. Because the gearbox has losses, the overall system efficiency would be negatively impacted. Also, as the system is scaled up, the increase in the tether diameter would require a proportional increase in the drum diameter in order to keep the tether from excessive mechanical stress due to bending. At some point, this diameter scaling would render the configuration unfeasible.

Figure 11 – Goldstein's fast-motion transfer system.
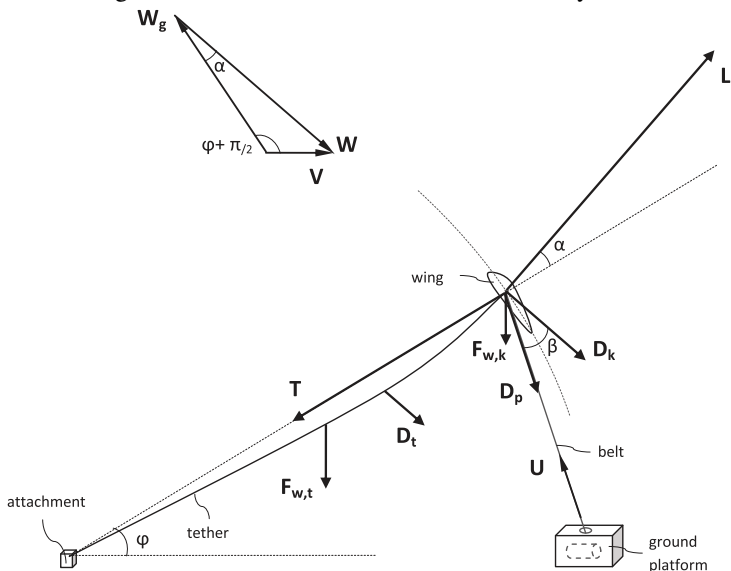
Source: Goldstein (2013)

The system proposed by Goldstein also exploits the crosswind. The wing is attached to the ground through a tether of constant length, which becomes subject to a traction force **T** mainly due to the kite lift force **L**. There is another tether, named *belt*. One of its tips is connected to the wing, while the other is wound around a drum on the ground, connected to an electric generator. Thus, power is produced as the wing flies with a speed $\mathbf{W_g}$ relative to the ground. Because, in the crosswind motion, the magnitude of the apparent wind approaches that of the kite, i.e. $W \approx W_g$, the reel-out speed U in this configuration is high enough so that the gearbox between drum and electric machine is no longer needed. Also, the belt tension would be at least one order of magnitude lower than the tether traction force. This is because the belt tension has the effect of the turbine "drag" (thrust) force in Loyd's drag mode, contributing to the wind power removal. As a consequence, the optimal belt tension could be approximated by D_p^* in Eq. (1.3), as well as by a function of the tether traction force and aerodynamic coefficients of the wing, according to the expression

$$D_p^* = \frac{1}{2} D_k = \frac{1}{3} \frac{C_D}{C_L} T. \tag{1.6}$$

This means that the mechanical system for power conversion on the ground would be subject to a smaller traction force (and torque on the drum) because $D_p \ll T$, thereby simplifying the mechanical structure. Similarly to the pumping kite, one operation cycle of Goldstein's system has two phases: in the working phase, the wing flies upwards, pulling the belt and producing electric energy on the ground. At some point, the wing executes an U-turn and heads downwards, when the returning phase starts, and the belt is reeled back in through an electric motor connected to the drum. This belt retrieval would occur at the expense of only a fraction of the energy produced in the working phase. When the wing executes another U-turn, the flight direction becomes upwards again, and a new working phase begins. Table 1 contains some scenarios of parameterization and numeric simulation results of the fast motion transfer configuration. Flexible (FW) and rigid (RW) wing types were considered, as well as round (RT) and streamlined (ST) tethers.

Despite Goldstein's arguments, and to this author's best knowledge, it has not been found in the literature so far, nor in the general media, any reference to a prototype construction of the fast motion transfer system, let alone its commercial use. This may result from features that, if on the one hand are the reason for the claimed advantages, on the other hand give rise to complications as well. For instance, Goldstein's system has two anchoring points on the ground, the *attachment* and the *ground platform* in Fig. 11, instead of the single anchoring point of the pumping kite. Hence, the ground platform

Table 1 – Parameterization and simulation results of power production of Goldstein's AWE system.

		(wing type,tether type)		
		(FW, RT)	(RW, RT)	(FW, ST)
wind	[m/s]	12	12	15
wing lift, C_L	–	1.2	1.5	1.2
wing drag, C_D	–	0.15	0.05	0.15
tether drag, C_t	–	1.2	1.2	0.2
wing area	[m^2]	500	500	3.000
altitude	[m]	1.000	1.000	3.000
working power	[MW]	1.82	7.27	15.5
cycle power	[MW]	1.09	4.36	9.32

Source: Goldstein (2013)

would have to rotate around the attachment point according to changes in the wind direction. The distance between the two anchoring points would also determine the tether length. Therefore changing the tether length to optimize the harvested power according to variations of the wind with the altitude could be a challenging thing to do as well. Finally, observe that the flight path of Goldstein's system would be similar to a "standing eight", instead of the "lying eight" usually considered for Loyd's lift mode. Flying a standing-eight path would require a faster steering response to make the wing execute the U-turn when heading towards the ground at a faster speed, in comparison to making the U-turn when flying mostly horizontally in the lying-eight.

1.3.2 Multiple-wing configurations

In the turning of the century, Ockels (2001) proposed the *laddermill*, a configuration composed of multiple wings attached to a tether in a closed circuit called the "translator", similar to a ladder, as depicted in Fig. 12. The idea is that the sum of the lift force being exerted on each wing that is going up the ladder is much stronger than the sum of the lift force on each wing going down the ladder. Consequently, there is a resulting tether (translator) force, T_{res}, that drives a generator on the ground. Power is obtained depending on the speed with which the generator is driven, as in Eq. (1.4), because this configuration also exploits the lift mode. In Table 2, simulation results of three operation scenarios are presented. According to Ockels' estimates, the laddermill offers advantages like being able to exploit high-altitude wind energy at a lower installed capacity cost, as well as being scalable to high power

levels. However, this configuration gives rise to serious safety concerns when its practical implementation is taken into consideration, such as the collapse of the ladder structure when there is lack of wind, and the collision risk with aircraft. Proper launching and landing could be complicated procedures as well, given the task to keep the multiple wings operating in a synchronized fashion.

Figure 12 – Ockels' laddermill AWE concept.

(a) Structure overview and wind profile intercepted. (b) Varying wing setup.
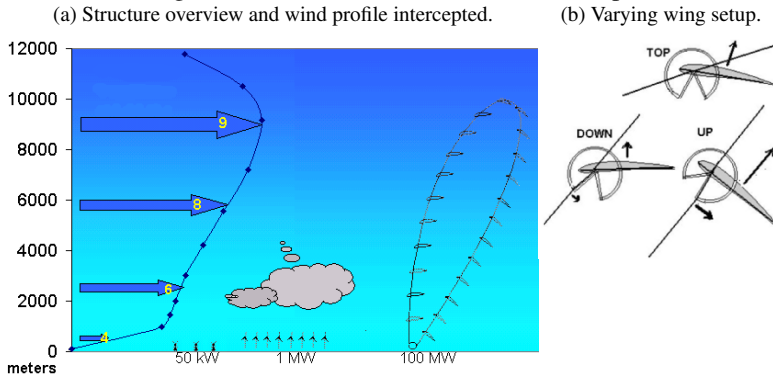
Source: Ockels (2001)

Table 2 – Ockels' laddermill parameterization and static simulation results obtained with the simulator from TU Delft.

		system size		
		small	medium	large
wing size	[m²]	20	60	1.000
wing mass	[kg]	10	30	500
distance between wings	[m]	10	20	65
number of wings	–	52	416	416
tether diameter	[mm]	3	22	160
cable speed	[m/s]	2.0	3.4	5.2
laddermill height	[m]	207	3.216	11.100
power	[kW]	11	1.220	47.800

Source: Ockels (2001)

Studies of the *Carousel* configuration, shown in Fig. 13, were first published by Canale, Fagiano and Milanese (2007). The Carousel consists of a series of Kite Steering Units (KSUs) – where the generators/motors that

steer the kite are located – mounted on rails and moving along a circular trajectory. Each KSU is connected through a rigid arm to a rotor in the carousel center, where an electric generator is located. Power is obtained by exploiting Loyd's lift mode in two ways: by reeling out the tether at each KSU, according to Eq. (1.4), and by the electric generator in the carousel center, whose input mechanical power is $P = \dot{\Theta} Q_c$, where $\dot{\Theta}$ is the angular speed of the carousel, and Q_c is the sum of the torques produced by each KSU. The carousel angular speed is kept constant at an optimal value. As depicted in Fig 13, the traction phase of a KSU begins at $\Theta = \Theta_3$, where the tether force is able to contribute to the total torque Q_c. A suitable reference curve for the tether reel-out speed is applied in order to maximize the power output. At $\Theta = \Theta_0$ the kite can no longer pull the carousel because it starts going against the wind direction, thus characterizing the end of its traction phase and beginning of its passive (retraction) phase. The three subdivisions of the passive phase refer to how the kite is maneuvered in its flying zone (wind window), and the corresponding tether winding speeds, in order to maximize the cycle power of the carousel. The control signals are the difference in the tether length of each KSU (each kite has two tethers, one for each wingtip), the (average) tether reel-out speed, and the carousel angular speed. Given a carousel with at least two KSUs placed $180°$ distant from each other, the carousel is able to operate without an external input of energy during the passive phase of each kite individually, as if the carousel were a "windmill in the airflow".

Two years later, Fagiano (2009) proposed a different carousel configuration in which the KSU did not produce torque for a common generator at the carousel center. Instead, each KSU had an electric generator being driven by wheels rotating along the carousel track. As a result of his optimal control strategy, he observed that the maximum absolute power (considering traction and passive phases) achieved through tether reeling was about 10 MW, while the maximum power generated through the motion of the KSUs along the carousel was 14 MW. Due to the kite passive phase, however, the carousel average cycle power was of only 1.65 MW. These power peaks characterized a major drawback, because the electric machines would have to be sized for about 10 times the average produced power. Thus, he suggested that the carousel with KSUs having only the wheel-attached generators – i.e. with a constant average tether length connecting to the kite – was the more promising candidate for further investigations.

Another multi-wing approach was studied by Houska and Diehl (2007), who executed numerical optimizations of AWE systems with tethered wings operating in lift mode. They proposed the configuration with two kites shown in Fig. 14, informally referred to as the "dancing kites". The name arises from the kite antisymmetric trajectories, seen in Fig 14b on the $(\mathbf{y}, \mathbf{z})$ plane,

Figure 13 – Carousel AWE configuration.
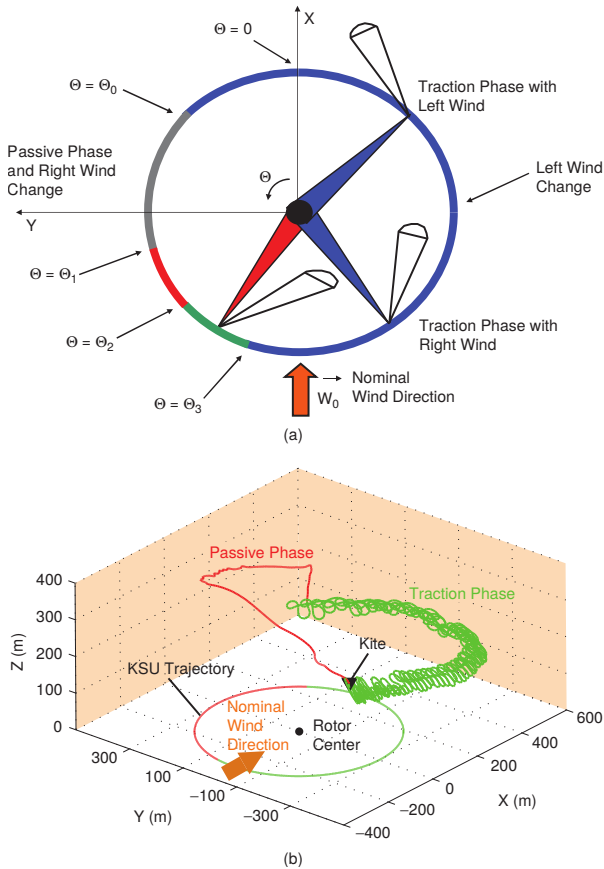
Source: Canale, Fagiano and Milanese (2007)

with the wind blowing in the $\mathbf{x} = \mathbf{z} \times \mathbf{y}$. The red-dotted segments refer to the retraction (passive) phase of periodic orbits[3], i.e. orbits which are repeated with the same initial tether length. The antisymmetric trajectories allow the main tether – between the ground and the juncture point – to remain almost static, thus suffering much less air drag. The result is that a greater power output is possible during the traction phase, when the main tether is reeled out at an optimal speed. The retraction phase is also benefited, since the kites can be flown in trajectories where the forces on the secondary tethers – be-

---

[3]Periodic orbits can also be referred to as close orbits.

tween each kite and the juncture point – practically cancel each other out. As a consequence, the main tether force can be greatly reduced for the retraction phase.

Figure 14 – Houska and Diehl's "dancing kites".

(a) Concept.

(b) Optimal kite trajectories.
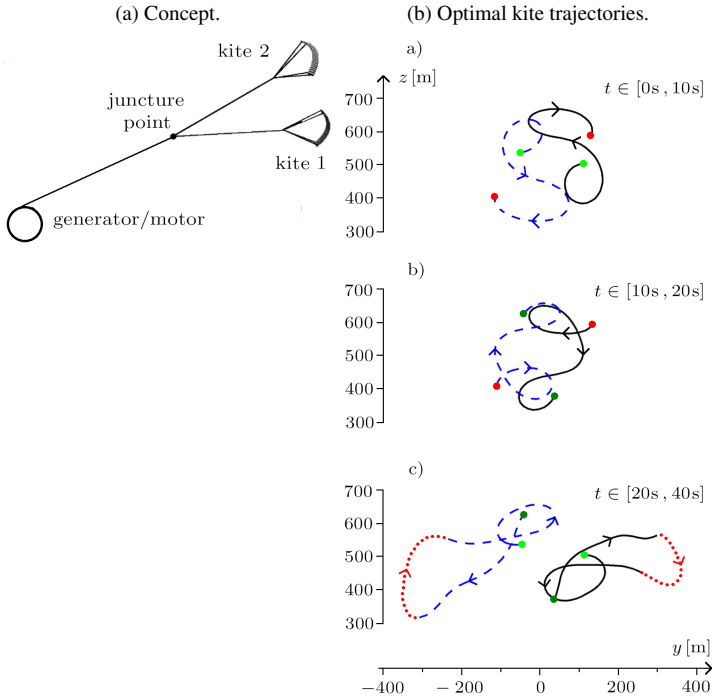
Source: Houska and Diehl (2007)

Based on simulations with a kite area of $500\,m^2$, a main tether length around $1,350\,m$, and an average wind speed of $12.3\,m/s$ at the operating altitude, the dancing kites produced an average cycle power of $14.86\,MW$. This means $7.43\,MW$ per kite whereas, when operating alone, each kite was able to achieve a cycle power of only $4.9\,MW$. Despite this advantageous prospect, the dancing kites, as in the case of all previously mentioned multiple-wing AWE configurations, offer stern challenges for practical implementation. For instance, the online controller of each kite must track fairly well the offline-calculated reference trajectories in order to achieve the antisymmetric feature – needed both for flight stability as well as for cycle power maximization. Also, the controllers must ensure that the kites do not collide in the presence

of turbulence. Automated launching and landing maneuvers, still to be solved in a robust way for the pumping kite, are even more of an open topic for the dancing kites.

Due to their compelling features, AWE systems based on single tethered wings are also being adapted to other applications. For instance, the Swedish company Minesto is currently developing a drag-mode underwater system named "Deep Green", to generate electricity from the tidal and ocean currents. The company is aiming at the deployment of a 1.5 MW version of its concept in 2017. The German company SkySails has developed an AWE system in crosswind flight for towing seagoing vessels, as explained by Erhard and Strauch (2012) and Erhard and Strauch (2015). It is claimed that the system, employing a flexible ram-air kite of $320\,\mathrm{m}^2$, can replace up to 2 MW of the main engine propulsion power.

Besides the configurations discussed so far, many others can be found in the literature, including several patents, exploring the use of tethered wings for harvesting energy from the wind and water flows. Neither the scientific community nor the industry has yet come to an agreement on which configuration is the most promising one in terms of efficiency, technological and economical feasibility, scalability and reliability. According to Schmehl (2015), at the beginning of 2015 there was a total of 55 institutions around the world actively involved with Research & Development (R&D) in the field, including academy and industry, represented in the world map of Fig. 15.

A few years ago, a report from consultants on renewable energies at GL Garrad Hassan (2011) revealed two fronts which require special attention in order to push forward AWE technology towards commercial deployment. First of all, AWE systems must offer a reliable, safe operation. The risk of a fast-flying flexible kite, or even worse, of a heavier rigid wing aircraft losing control and crashing into the ground, possibly induced by turbulent operating conditions or component wear, must be minimized to a tolerated level. At least, such systems should be able to be promptly put out of operation when these conditions are formed, thus minimizing the risk of accidents. This would also be important to receive public support when planning to deploy AWE systems over land and near populated areas. Also, some technological aspects still must be solved or improved to allow for a robust operation, as, for instance, the automatic launching and landing strategies for lift-mode systems, especially those with flexible wings.

Secondly, when the technology becomes more mature, investors and insurance companies will require design standards and a certification scheme. The lifetime of cables and wings, especially when it comes to flexible kites made of synthetic fabric, must be proven to be minimally long in order to reduce maintenance costs. Besides, regulatory issues will have to be addressed

Figure 15 – Institutions actively involved with R&D in AWE technology around the world at the beginning of 2015.
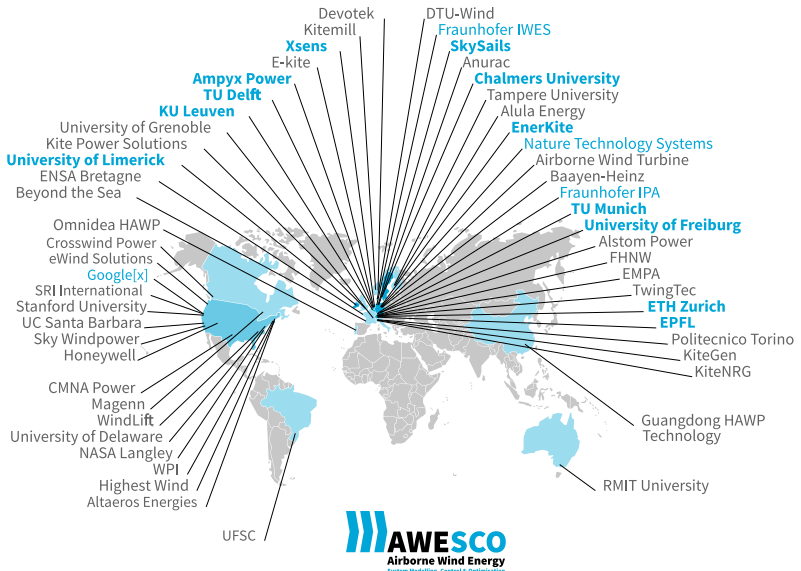
Source: Schmehl (2015)

with the air traffic authorities, since the operation of AWE systems can create a collision risk with aircraft, or cause radar interference.

1.4 OBJECTIVES AND CONTRIBUTIONS

It is evident that the road to large-scale deployment of AWE systems still requires further advancements. In particular, the prospect for tethered wings to become a feasible alternative to the challenge of expanding the energy offer while attending environmental concerns seems promising. With this motivation, the goal of this dissertation is to serve both as a manuscript for the lay reader, interested in getting acquainted with the technology and who has some background on physics, aerodynamics, dynamic systems, classic control and optimization techniques, as well as by specialists in these areas, who intend to carry out deeper investigations.

Based on theoretical results obtained through simulations, the contributions of this dissertation address four different aspects of AWE with tethered wings, focused on the pumping kite concept:

a) to revisit models from the literature used in AWE, especially those describing the flight dynamics of a tethered wing. The derivation of the course angle dynamics and the two-tether point-mass wing are explained step-by-step, and some adjustments to the latter model are proposed. The contribution in this regard is based on the relevance of these models and the fact that they are not found so far in (didactic) textbooks. The idea is that all information required to reconstruct a dynamic simulation model for the pumping kite flight can be found in this dissertation;

b) based on some of the models compiled above, to compare different control laws for the flight of a pumping kite in a decentralized topology, where the control inputs of the tethered wing and the ground winch are computed separately. In particular, an approach with Bernoulli's lemniscate for the lying-eight flight during the traction phase is detailed;

c) to formulate an optimization problem, considering constraints on the angle of attack and reel speed, in order to choose the operating parameters of the traction and retraction phases that yield the maximum cycle power;

d) to reinterpret Loyd's lift (the pumping kite traction phase) and drag modes as particular cases of the actuator disc considered in the derivation of the Betz limit for power extraction from the wind, using the same modeling framework as for the horizontal-axis wind turbines.

The rest of the dissertation is organized as follows. In Chap. 2, most of the mathematical models considered in this work are presented. In Sect. 2.1 we discuss the four-tether steering concept and the state-of-the-art models describing the deformations and aerodynamics of flexible wings (kites). Sect. 2.2 follows with the concept of the two-tether kite, where we revisit, in detail, and propose some corrections and extensions to the point-mass kite model, which will be used to simulate the wing flight. In Sect. 2.3 we discuss the massless wing in dynamic equilibrium, used to optimize the traction phase of the pumping cycle. The derivation of an important Single-Input Single-Output (SISO) model for the flight dynamics, used for control design, is made in Sect. 2.4. To represent how the average wind increases with altitude due to viscous interaction with the ground, in Sect. 2.5 we explain and interpolate the logarithmic wind shear model and the wind histograms for different locations.

Several aspects of the pumping kite are addressed in Chap. 3. Firstly, we will design flight controllers, in Sect. 3.1, to be used both for the lying-eight figure of the traction phase as well as for the retraction maneuver. With

this controller we will be able to simulate a full pumping cycle. Before we do so, we need to choose the values of the parameters that define the pumping cycle, which is the focus of Sect. 3.2. The traction phase is parameterized with a base angle of attack, a reel-out speed, an average polar angle of the lying-eight trajectory, and an average tether length. As for the retraction phase, it is parameterized by means of two coefficients describing the ramp inclinations of the traction force and base angle of attack, and two constant values at the end of these ramps. We then formulate an optimization problem with the goal of finding the set of parameters that yields the maximum cycle power. We will also consider constraints which affect practical implementations of the AWE system. Regarding the ground winch, there is the reel speed saturation, which determines a minimum duration of the retraction phase. As for the flight with (flexible) kites, we assume a maximum de-powering[4] that can be applied, and a minimum value for the angle of attack, which is important in order to ensure a robust flight. By taking into consideration these constraints we expect two things. First, is to obtain a more realistic insight into how much power can be actually harvested from the wind. Second, the resulting operating parameters should correspond to an optimal trade-off between cycle power maximization and robust operation of the wing, which is a crucial point. The chapter is concluded with Sect. 3.3, where we compute and analyze the pumping kite power curve.

The idea in Chap. 4 is to compare, using the same modeling framework, AWE with conventional wind energy based on horizontal-axis wind turbines. We start, in Sect 4.1, by using momentum theory applied to the generic actuator disc to derive Betz limit for the extraction of power from the wind. Next, in Sect 4.2, we extend the model with the radial dimension of the disc. The model is once more extended, in Sect. 4.3, by considering the aerodynamics and geometry of the specific airfoil used for the blades (or wing). In the sequel we formulate the expression of the power coefficient of Loyd's lift mode. Sect. 4.4 finishes the chapter by comparing the average energy generation (capacity factor) of pumping kites and wind turbines based on their power curves and the histograms for some locations around the world.

The manuscript is concluded with Chap. 5, where we summarize the main contributions, emphasize some important conclusions, and point out topics for future works. The main results of this PhD dissertation in terms of publications and research grants are also listed.

---

[4]By "de-powering" we refer to the decrease of the wing lift and drag coefficients in order to reduce the aerodynamic force and thereby also the traction force on the tether, which is a necessary condition to perform an efficient retraction phase.

2 MODELS FOR TETHERED WINGS

Many models have been proposed in the literature to describe the behavior of a tethered wing, in several levels of accuracy and for different steering mechanisms. The most complex models are able to describe the aerodynamics and deformations of the wing in detail, yet at a high computational cost. As a consequence, they are strictly oriented to simulation. Models with intermediate levels of complexity still achieve a reasonable level of detail and thus can be used for faster, real-time simulations. The simplest models are more appropriate for analytical tasks such as optimization and control design, for instance.

For the contributions in this dissertation we will address four wing models: one of intermediate complexity, to simulate the 3D translational dynamics of the tethered wing, and three simpler, analytical models, used for optimization and control design. The chosen models will consider a generic wing with given aerodynamic characteristics and a steering based on the difference in the length of two tethers reaching the kite, i.e. we will not consider the aircraft setup with ailerons. For all wing types – rigid or flexible – pulling one tether while releasing the other will cause the wing to execute a turn in the same direction. However, the internal mechanisms through which the change in the flight trajectory is achieved can be different. Basically, a steering input causes a rigid wing to roll and a flexible kite to deform. In the next two sections we will discuss these different steering implementations, their corresponding de-powering possibilities, and some models found in the literature.

2.1 FOUR-TETHER FLEXIBLE KITES

One of the branches of AWE with tethered wings focuses on the use of flexible kites, which offer some interesting advantages. First of all, the current technology allows for a maximum wing loading compatible for energy generating purposes. For instance, Leading-Edge Inflated (LEI) tube kites reach a maximum loading of about $500\,\text{N/m}^2$, while foil (ram-air) kites – as the $320\,\text{m}^2$ one described by Paulig, Bungart and Specht (2013) for towing sea-going vessels – reach even higher values, withstanding approximately $1\,\text{kN/m}^2$ at a specific weight[1] of $7.8\,\text{N/m}^2$. Moreover, flexible wings are significantly lighter and cheaper to build than rigid wings. Also, in the eventual case of crash with the ground, the damage caused and/or suffered by the flex-

---

[1]The specific weight, or fabric density, increases with the wing loading. It is usually found that LEI tube kites have a higher specific weight than foil kites with the same area.

ible wing is much lower than the damage associated with a rigid wing.

Based on these motivations, in recent years the level of sophistication in wing modeling has rapidly increased, focusing especially on a more realistic simulation of the dynamics of flexible kites. The majority of these models considers the four-tether actuation concept, shown in Fig. 16 for a LEI tube kite. In this concept, a single (main) traction tether leaves the drum attached to the generator on the ground and splits into two tethers at a "Y" bifurcation near the kite. Each of these two tethers are then connected to the kite leading edge, and are responsible for transmitting the bulk of the traction force used for power generation at the ground. In the case of a foil kite, the two tethers are formed by merging the A, B and C lines from each half of the wingspan, as it will be seen later in this section. Sitting atop the "Y" bifurcation and held in place by the two *traction tethers* going up to the kite leading edge is a control pod. It contains an actuator responsible for manipulating two *steering tethers*, which are connected to the wingtips closer to the kite trailing edge. By pulling one tether while the other is released, i.e. by creating a difference in the tether length $\Delta l = l_L - l_R$, where l_L is the left tether length and l_R is the right tether length, the kite is deformed, causing it to yaw and translate sidewards simultaneously.

The *base angle of attack* α_0, and consequently the angle of attack α, can be augmented by decreasing the length of both steering tethers through an equal amount Δl_p. A reverse operation must be done to de-power the kite, i.e. to make α_0 become negative. De-powering, however, is usually limited to a small interval for this four-tether system with LEI tube kites. The main reason is that, as α_0 becomes negative, the apparent wind starts reaching the kite from "above" (at the outer kite area), and the wing loading inside the C-shaped kite drops. Consequently, at some point, the inflated main strut along the leading edge is not able to withstand the pressure caused by the apparent wind coming from "above", and the kite loses its inflated characteristic C-shape. A consequence of this behavior is that a LEI tube kite must operate above a minimum angle of attack in order to ensure a safe operation.

The models developed in the latest years for the four-line flexible kite are particularly important to validate control laws designed with simpler models. In contrast to the blades of the wind turbines, as pointed out by Bosch et al. (2014), in the case of a LEI tube kite, the airfoil shape is determined by the aerodynamic wing loading and pressure distribution in the tubes, as well as by the internal forces in the membrane fabric and bridle lines. Due to its low inertia, the wing response is very sensitive to control commands, fluctuations of the apparent wind (for instance caused by turbulence), and changes in the kite geometry due to variations of the wing loading. These factors contribute to making robust automated flight control a challenging task.

Figure 16 – Four-tether actuation concept with control pod for steering and
de-powering (here seen for a LEI tube kite).

center chord

(projected) wingspan w_s

trailing edge

α_0

Δl_p

steering

$\Delta l = l_L - l_R$

leading edge

(de-)powering

pulleys

control pod

"Y" junction

Legend

Traction
Fixed length steering
Variable length steering
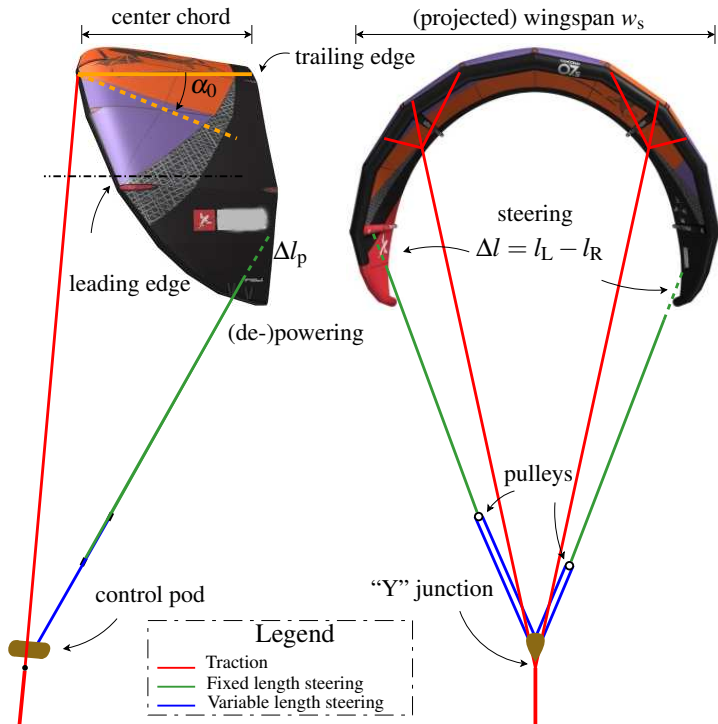
Source: original

Implementing a detailed simulation model is far from being an easy
task. The strongly coupled aerodynamics and structural dynamics of the wing
constitutes a challenging Fluid-Structure Interaction (FSI) problem. One ef-
fort in this direction was made by Breukels (2011), who discretized the wing
into multiple bodies, each one having its independent aerodynamics described
by the modeller. Another approach was used by Baayen (2012), who illus-
trated the use of a 3-dimensional panel method to simulate a power kite inter-
acting with the apparent wind. Given that the panel equations can be easily
solved numerically in comparison to the Navier-Stoques equations, the panel
method approach offers a computational advantage which makes it a suit-
able candidate for implementing a detailed dynamic simulation at a relatively
high speed. Simply put, the idea is to use the panel method to obtain the
forces and moments acting on the kite; these cause the shape and tension of

the tethers to change, which is calculated by a solver of ordinary differential equations. The force on the bowed tether, in turn, acts back on the kite, deforming it. This feedback loop characterizes a stiff interaction. Because in the panel method the computed aerodynamic forces and moments result from the shape of the entire wing, its orientation in the flow, and its interaction with the wake, Baayen expected his method to be more accurate than Breukel's multi-body one.

In his modeling framework, Baayen (2012) considered the tether as a string of point-masses connected by high-modulus dampers. The aerodynamic forces acting on the kite, resulting from the panel method, are added to the spring-damper forces of the top point-mass in the tether model. In this way, the bulk of the kite lift force is balanced by the tether forces. Baayen attempted to model one important deformation mode of the kite – the *spanwise bending* – inspired by the observation that the tips of arc-shaped kites bend inward when pulling on their respective steering lines. The resulting asymmetrical shape occurs because, when turning, while the steering line on one wingtip is being pulled, the steering line on the other wingtip is being released. Bosch et al. (2014) investigated in more detail this and other kite deformation effects on an inflatable membrane wing. Their approach, however, was to use a geometrically nonlinear finite-element framework to describe the large quasi-static deformations caused by changing the bridle line geometry and by the varying aerodynamic loading. The effect of the external flow was described in terms of discrete pressure distributions for the different wing sections.

The static structural model is based on a finite-element discretization of the wing. The canopy is represented by triangular shell elements, whereas the pressurized tubular frame is represented by beam elements. The steady aerodynamic load model provides a discrete surface pressure distribution for each wing section as a function of its local relative flow conditions and shape deformation. The dynamic behavior of the complete system consisting of wing, bridle lines, control pod and tether is described by a particle system model. Bridle lines are described as linear spring-damper elements, whereas the tether is described as a distance constraint. The inertia of the system components is represented by point masses at the control pod and at the bridle line attachments on the wing. For each dynamic integration step, the structural model provides the resulting wing forces at the bridle line attachments. These forces are applied as external loads to the particle system model. Following the integration step, the updated positions of the point masses are returned to the structural model and treated as displacement boundary conditions.

As observed by Bosch et al. (2014), the spanwise wing bending results from the aerodynamic wing loading. The heavily loaded center part of the

wing is pulled outwards, as illustrated in Fig 17b, tensioning the bridle line system and the tether, and forcing the less loaded wingtips to move towards each other. This bending deformation reduces the tip distance of the unloaded wing by an average value of 1 m, i.e. about 20 % of the design value of the North Rhino 16 m^2 kite analyzed in that work.

Figure 17 – Spanwise deformation effects on a LEI tube kite, exemplified when the right wingtip (left-hand side) is pulled.

(a) Bottom view: wing torsion.
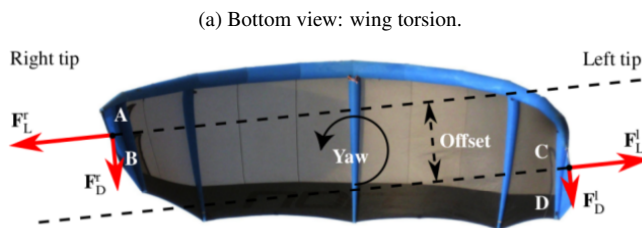
(b) Leading edge perspective view: wing bending .
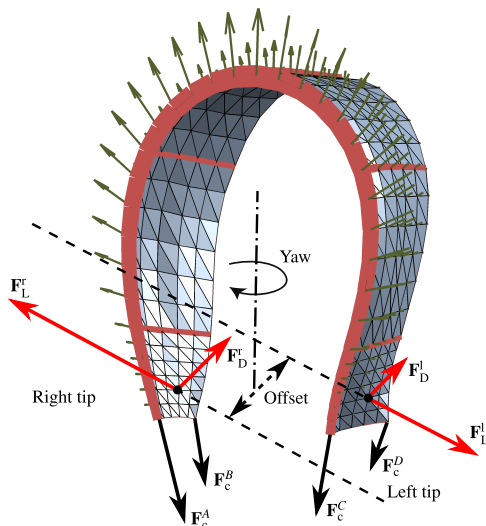
Source: Bosch et al. (2014)

According to Breukels (2011), pulling on one of the steering lines attached to the kite trailing edge not only increases the aerodynamic forces at the respective wingtip – due to the increase in the angle of attack in that region – but also leads to a spanwise *wing torsion*, depicted in Fig. 17a. This

antisymmetric deformation significantly amplifies the aerodynamic yaw moment, forcing the wing to turn around the actuated tip. It is due to this effect that the C-shaped kite is regarded to have an excellent maneuverability[2].

Fig. 17b is also helpful to illustrate how the steering input on a four-tether LEI tube kite occurs. In the depicted case, by pulling on the right wingtip (viewer's left-hand side) the angle of attack increases in that region, causing both the lift $\mathbf{F}_L^r$ and drag $\mathbf{F}_D^r$ forces to increase, whereas releasing the left steering line causes the opposite effects in the left wingtip. Therefore the kite responds in two ways. First, because the lift on the right wingtip is higher than on the left wingtip, i.e. $\mathbf{F}_L^r > \mathbf{F}_L^l$, the kite suffers an acceleration in its lateral axis (sidewards translation). Second, we can see that all aerodynamic forces shown, except for $\mathbf{F}_D^l$, produce a torque around the kite vertical axis because of the offset induced by the torsion deformation, causing the kite to yaw in the clockwise direction (as seen from above).

Another flexible wing type that can be used with the four-tether concept is the foil (ram-air) kite. We can highlight some differences between foil and LEI tube kites. To start, for a same total area, foil kites usually have a higher projected area, i.e. they are "flatter". This is good for producing traction, but at the expense of less maneuverability than LEI tube kites, which tend to be more "C-shaped". A second difference is that the bridle line system of a foil kite has many more attachments points to the kite, forming basically three line groups, as shown in Fig. 18. Since the produced lift force is much higher in the leading than in the trailing edge, most of the wing loading is supported by the A-lines, an intermediate portion by the B-lines, whereas the smaller share is transmitted by the C-lines. These three line groups are merged to form the two traction tethers (one for each side), that merge at the "Y" junction right below the control pod. Finally, the F-lines (brakes) converge to the corresponding left and right steering tethers, connected to the differential steering actuator. By pulling on one F-line the respective wingtip is slowed down, causing the kite to yaw.

Differently from a LEI tube kite, the base angle of attack of a foil kite cannot, a priori, be changed during operation – it is predetermined by the bridle line system. Therefore, the de-powering procedure must be other than equally increasing the length of both steering tethers. One possibility is to apply the so-called "B-stall". To this end, a de-powering tether is clamped to the B-lines (from both sides) some 50 cm distant from the control pod. Thus, when the de-powering actuator pulls on the B-lines between 15 cm and 20 cm, the airfoil shape (cross-section) changes, as shown in the right-hand side of Fig. 18. Basically, the perimeter of the inner part of the airfoil increases so that the speed of the airflow passing right above and under the airfoil become

---

[2]though in detriment of a higher glide ratio.

Figure 18 – Four-tether actuation concept with control pod, for steering and de-powering (through "B-stall") a foil (ram-air) kite.
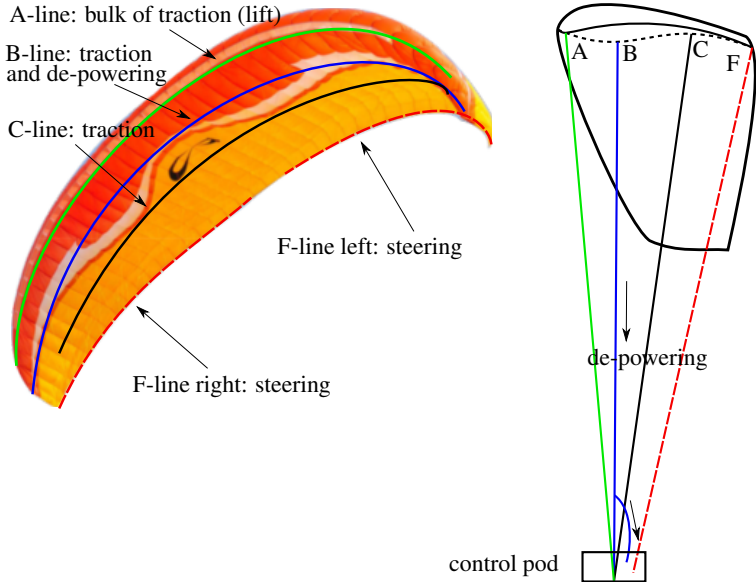
Source: original

practically the same. This causes the pressure in the inner part (wing loading) to drop, thus decreasing the lift and increasing the drag. With the B-stall maneuver, the glide ratio can be reduced typically from 10 or 8 to about 2 or even less.

Another relevant difference is that foil kites are usually lighter than LEI tube kites of same area, which helps maintaining the apparent speed (and harvested power) when going up the lying-eight path in the crosswind, besides requiring less wind for launching and landing. Moreover, foil kites have a higher aerodynamic efficiency, also known as glide ratio, defined as $E = C_{\mathrm{L}}(\alpha)/C_{\mathrm{D}}(\alpha)$, where $C_{\mathrm{L}}(\alpha)$ is the airfoil lift coefficient, $C_{\mathrm{D}}(\alpha)$ is its drag coefficient, and α, the angle of attack. The higher is E, the more power can be harnessed from the wind. One last important observation about foil kites is that, if the angle of attack becomes negative, the air intake (openings) at the kite leading edge may close. This can lead to loss of the airfoil shape by "deflation", and the kite may enter a stall without control. Hence, to avoid this dangerous condition, a constraint on the minimum angle of attack around zero should be considered, perhaps an even stronger constraint

the one already discussed for LEI tube kites.

2.2 THE TWO-TETHER POINT-MASS WING

We know from aeronautical sciences (see e.g. Stevens and Lewis (2003)) the three basic control surfaces (actuators) of a "conventional" aircraft: the ailerons, the rudder and the elevator. By actuating on the ailerons the airplane rolls (tilts around its longitudinal axis), the lift force vector is decomposed on the horizontal plane as a centripetal component and, consequently, the airplane executes a turn. Now imagine we remove the ailerons and tether each of the two wingtips to a drum connected to an electric machine on the ground. By pulling one tether while releasing the other one in the same amount, the aircraft is rolled as in the case with ailerons. One advantage of the tether-induced roll is that, besides controlling the flight, the tethers can be used to generate electricity if reeled out while subject to a traction force. This is the steering and power-harvesting concept used e.g. by the Swiss company TwingTec with its TT100 model, and by the German company Enerkite with its EK200 model. Changing the base angle of attack α_0 (decreasing it for de-powering) continues to be possible with the two-tethered rigid wing through the elevator.

We could also hypothetically use this two-tether concept with foil kites, for instance. In this case, the F-lines (brakes) in Fig. 18 would be left unused. De-powering could be more challenging, though, because the B-tethers (from each wing side) should arrive separately at the ground in order to be pulled, so that we would actually have four tethers (2 ACs and 2Bs) at the ground level. This increase in complexity leads us to conclude that, when considering the two-tether steering mechanism, rigid wings[3] offer an advantage over flexible wings due to the separation between the aerodynamic surfaces upon which the power-generating lift force acts (main wings) and the surface used for de-powering (elevator). This separation allows the wing to operate at an angle of attack low enough so to practically cancel the lift, causing the tether force to be greatly reduced, which is essential for an efficient reel-in maneuver. In short, the possibility of having the elevator in a rigid wing is a big advantage for de-powering. Another advantage of rigid wings over the other types is a higher aerodynamic efficiency (glide ratio), which unfortunately comes along with a higher density (specific weight) as well.

At this point we are able to highlight some differences between both

---

[3]It is well known that even rigid airplane wings are, to some degree, flexible. Yet, when compared to LEI tube kites or foil kites, which are made of synthetic fabric, the flexibility of rigid wings is negligible.

steering concepts. First of all, because the steering causes deformations on the four-tethered wing, the latter must be *flexible* – a LEI tube or a foil kite. Also, having only one main tether is better for reducing the aerodynamic drag, allowing the kite to reach higher speeds and, ultimately, to produce more power than with the two-tether concept. On the other hand, keeping the control pod airborne demands lift force from the kite, which has a negative impact on the lift force left for power generation, especially when going up in the eight-figure flight path. Back to the advantages of the four-tether concept, the fact that the actuators are closer to the kite makes steering less susceptible to transport delay – an important feature for flight performance and robustness. However, having airborne actuators requires providing power supply to the control pod. There are basically two ways to achieve this: electricity could be transmitted from the ground through the main traction tether, or it could be generated directly on-board. In any case, undesired complexity is added to the airborne part of the AWE system. Finally, one important advantage of the four-tether concept is its versatility: because of the single (main) traction tether, the kite could be more easily used in mechanical configurations other than the classic pumping kite to convert the traction force into electric power.

As already discussed, the cost for the high level of accuracy and detail obtained with the state-of-the-art simulation models mentioned in Sect. 2.1 is a high computational load incurring in a slow simulation, besides the implementation effort. Aiming at a faster execution and simpler implementation while still maintaining a desired level of detail, it was chosen the two-tether point-mass approach, originally proposed by Diehl (2001), to model the translational dynamics of the wing. In this work, we will use the two-tether model also for four-tethered wings as LEI tube kites or foil kites, assuming the "B-stall" de-powering for the latter wing type. The idea is to focus on the same steering input that yields a similar change of trajectory – the difference in the length of the steering tethers. The internal steering mechanism (kite deformation or rolling) is not important for the conclusions that will be drawn.

Making the point-mass model applicable to both two-tethered and four-tethered wings affects the number of tethers n_t whose length r is significant to calculate the tether weight and drag. Hence, for the two-tether case we must consider the two steering/traction tethers, whereas for the four-tether case only the main traction tether is considered and the weight of the control pod can be added to that of the wing.

In the following sections, we will revisit the modeling procedure of the 3D point-mass model, attempting to give more detailed explanations, discussing the assumptions involved, proposing some adjustments, and interpreting the results. The parameters of this model will be adjusted for simulation purposes in the rest of the work.

2.2.1 Kinematics

Let us consider the nominal wind vector $\mathbf{v}_{w,[n]} = (v_w, 0, 0)$ and define the *nominal wind frame*, with orthonormal basis $(\mathbf{x}_n, \mathbf{y}_n, \mathbf{z}_n)$, whose origin is the mean point on the ground between the electric machines of the two-tether concept, or the location of the single electric machine of the four-tether concept, as illustrated in Fig. 19. The longitudinal direction is defined by $\mathbf{x}_n = \mathbf{v}_w / \|\mathbf{v}_w\|$, whereas the lateral direction is defined by the unitary vector $\mathbf{y}_n \perp \mathbf{x}_n$ such that vector $\mathbf{z}_n = \mathbf{x}_n \times \mathbf{y}_n$, which represents the vertical direction, points upwards. We will treat the nominal wind frame as the "inertial" one because we assume that the nominal wind direction varies with time very slowly if compared to the kite dynamics. In order to have the kite flight correctly centered in the wind window in a real application, this rotation of the nominal wind frame around the z-axis of the ground station frame should be detected and taken into consideration, for instance, by using the approach proposed by Zgraggen, Fagiano and Morari (2015).

Figure 19 – The point-mass wing of spherical coordinates (θ, ϕ, r) and Cartesian coordinates (x_k, y_k, z_k), and the wind window.
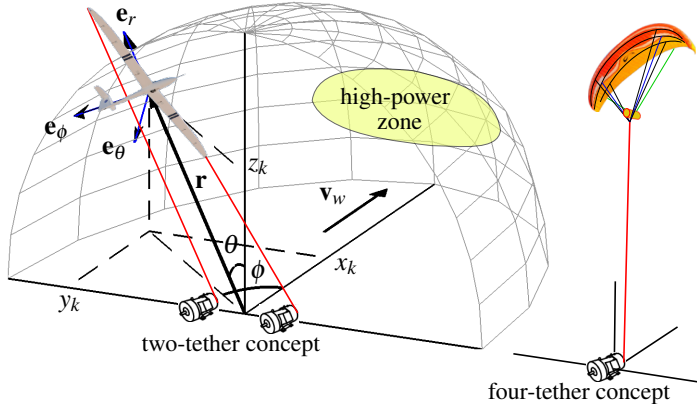
Source: original

Now let us consider the wing mass m to be concentrated in one point. Its position in the nominal wind frame can be represented by the spherical coordinates (θ, ϕ, r), where θ is the polar angle, ϕ is the azimuth angle, and r is the radial distance of the point-mass wing to the ground winch. Because the tether(s) are assumed to be perfectly straight and inelastic, and much greater than the wingspan, r also corresponds to the tether length. The wing position vector in Cartesian coordinates is

$$\mathbf{r}_{[n]} = \begin{bmatrix} x_k & y_k & z_k \end{bmatrix}' = r \begin{bmatrix} \sin\theta\cos\phi & \sin\theta\sin\phi & \cos\theta \end{bmatrix}'. \qquad (2.1)$$

Besides corresponding to the wing center of mass, vector $\mathbf{r}$ is also the origin of the *local frame* $(\mathbf{e}_\theta, \mathbf{e}_\phi, \mathbf{e}_r)$, defined in the nominal wind frame by the orthonormal vectors

$$\mathbf{e}_\theta = \frac{\partial \mathbf{r}}{\partial \theta}\frac{1}{r} = \begin{bmatrix} \cos\theta\cos\phi & \cos\theta\sin\phi & -\sin\theta \end{bmatrix}'$$

$$\mathbf{e}_\phi = \frac{\partial \mathbf{r}}{\partial \phi}\frac{1}{r\sin\theta} = \begin{bmatrix} -\sin\phi & \cos\phi & 0 \end{bmatrix}' \qquad (2.2)$$

$$\mathbf{e}_r = \frac{\partial \mathbf{r}}{\partial r}\frac{1}{r} = \begin{bmatrix} \sin\theta\cos\phi & \sin\theta\sin\phi & \cos\theta \end{bmatrix}',$$

hence the rotation matrix from the local to the nominal wind frame is

$$\mathbf{R}_l^n = \begin{bmatrix} \mathbf{e}_\theta & \mathbf{e}_\phi & \mathbf{e}_r \end{bmatrix} = \begin{bmatrix} \cos\theta\cos\phi & -\sin\phi & \sin\theta\cos\phi \\ \cos\theta\sin\phi & \cos\phi & \sin\theta\sin\phi \\ -\sin\theta & 0 & \cos\theta \end{bmatrix}. \qquad (2.3)$$

The wing velocity in the local frame is

$$\mathbf{v}_{k,[l]} = \begin{bmatrix} r\dot{\theta} & r\dot{\phi}\sin\theta & \dot{r} \end{bmatrix}'. \qquad (2.4)$$

The apparent wind in the local frame is

$$\mathbf{v}_{a,[l]} = \mathbf{R}_n^l \mathbf{v}_{w,[n]} - \mathbf{v}_{k,[l]}, \qquad (2.5)$$

where $\mathbf{R}_n^l = \left(\mathbf{R}_l^n\right)'$ is the rotation matrix from the nominal wind to the local frame, obtained by applying a transpose operation to the matrix for the inverse direction – a property which holds to all rotation matrices. We use $\mathbf{R}_n^l$ in Eq. (2.5) to have all vectors expressed in the same coordinate system[4].

Two other coordinate systems complete the model: the *apparent wind frame*, composed by the orthonormal basis $(\mathbf{x}_a, \mathbf{y}_a, \mathbf{z}_a)$, and the *body frame*, defined by $(\mathbf{x}_b, \mathbf{y}_b, \mathbf{z}_b)$. These coordinate systems are depicted in Fig. 20 and are used to define the aerodynamic forces and to represent the orientation of the kite with respect to the local frame, respectively.

For a null rotation of the apparent wind frame with respect to the local frame we have $\mathbf{x}_a \equiv -\mathbf{e}_\theta$, $\mathbf{y}_a \equiv \mathbf{e}_\phi$ and $\mathbf{z}_a \equiv -\mathbf{e}_r$. In this point-mass model we assume that the *wing symmetry plane* $(\mathbf{x}_b, \mathbf{z}_b)$ is coincident with the plane

---

[4]Note that we could also have used $\mathbf{v}_{a,[n]} = \mathbf{v}_{w,[n]} - \mathbf{R}_l^n \mathbf{v}_{k,[l]}$.

Figure 20 – Bases of the apparent wind frame, $(\mathbf{x}_a, \mathbf{y}_a, \mathbf{z}_a)$, and body frame, $(\mathbf{x}_b, \mathbf{y}_b, \mathbf{z}_b)$.
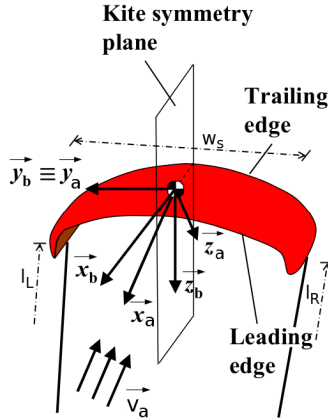
Source: adapted from Fagiano (2009)

spanned by $(\mathbf{x}_a, \mathbf{z}_a)$, similarly to what happens with a diamond-shaped kite because of its tail being blown by the apparent wind. In other words, we assume that the sideslip angle of the kite is always zero, which means that the wing changes its orientation instantaneously with $\mathbf{v}_a$, i.e. we do not model the wing moment of inertia and torques acting upon it. As reported by Baayen (2011) based on practical experiments with LEI tube kites, the zero sideslip angle is a good assumption when the steering input is close to zero, which typically happens in the center of the lying-eight trajectory of the traction phase, as well as during the retraction phase with zero azimuth.

The longitudinal axis of the apparent wind frame is defined as

$$\mathbf{x}_a = -\mathbf{v}_a/\|\mathbf{v}_a\|. \tag{2.6}$$

The wingspan w_s can be seen as the wing dimension in its transversal, $\mathbf{y}_a \equiv \mathbf{y}_b$ direction, as depicted in Fig. 20. Considering the two-tether concept and defining l_L and l_R as the cable length of the left and right wingtips, respectively, by creating a difference in the length of the steering/traction tethers the wing is rolled through an angle ψ:

$$\Delta l = l_L - l_R = w_s \sin \psi. \tag{2.7}$$

The angle ψ represents the inclination of the wing transversal axis with respect to the tangent local plane $(\mathbf{e}_\theta, \mathbf{e}_\phi)$, as shown in Fig. 21, or the

roll angle in the Tait-Bryan (Euler) nomenclature. If $\Delta l > 0 \Rightarrow \psi > 0$ and the kite turns to the right (when looking at the kite leading edge from the ground), and vice-versa. In this model, the roll angle is only valid in the interval $|\psi| \leq \pi/2$.

Figure 21 – View of the wing leading edge showing the roll angle ψ, created by the differential tether length Δl with the two-tether concept.
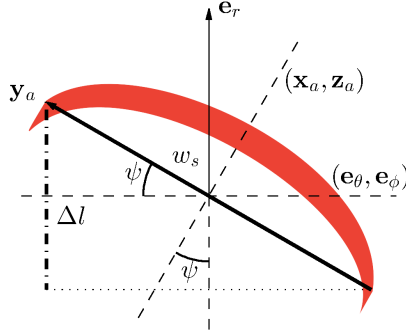
Source: original

To complete the basis of the apparent wind frame we define $\mathbf{z}_a = \mathbf{x}_a \times \mathbf{y}_a$. Hence we now need to calculate $\mathbf{y}_a$, whose direction changes as a function of ψ and the apparent wind direction. To this end let us establish some requirements. First of all, the kite transversal direction should be always perpendicular to its symmetry plane, therefore

$$\mathbf{y}_a \perp \mathbf{x}_a \Rightarrow \mathbf{y}_a \cdot \mathbf{x}_a = \mathbf{y}_a \cdot \mathbf{v}_a = 0. \tag{2.8}$$

Secondly, the projection of $\mathbf{y}_a$ onto $\mathbf{e}_r$ is $\sin \psi$:

$$\mathbf{y}_a \cdot \mathbf{e}_r = \sin \psi = \Delta l/w_s. \tag{2.9}$$

A third requirement is that the decomposition of $\mathbf{z}_a$ onto $\mathbf{e}_r$ must be always negative, i.e. it has to point in the opposite direction of $\mathbf{e}_r$:

$$(\mathbf{x}_a \times \mathbf{y}_a) \cdot \mathbf{e}_r < 0 \Rightarrow (\mathbf{v}_a \times \mathbf{y}_a) \cdot \mathbf{e}_r > 0. \tag{2.10}$$

We start to determine $\mathbf{y}_a$ by introducing the notion of the *partial angle of attack* $\Delta\alpha$, which is the angle between $\mathbf{x}_a$ and the tangent local plane $(\mathbf{e}_\theta, \mathbf{e}_\phi)$, defined as

$$\Delta\alpha = \arcsin\left(\frac{\mathbf{v}_a \cdot \mathbf{e}_r}{\|\mathbf{v}_a\|}\right). \tag{2.11}$$

We use the adjective *partial* to describe $\Delta\alpha$ because the component α_0, denoted as the *base angle of attack* by Fagiano (2009), can be added in order to produce the *total angle of attack*[5], as shown in Fig. 22:

$$\alpha = \alpha_0 + \Delta\alpha. \tag{2.12}$$

Figure 22 – View of the wing longitudinal cross section (symmetry plane) showing the components $\Delta\alpha$ and α_0 of the (total) angle of attack.
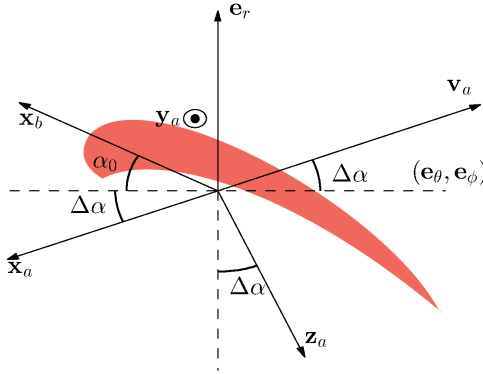
Source: original

The notion of α_0 is important, since this quantity can be chosen constant or varied at will as a control input in the case of a two-tether rigid wing with elevator (or with a third tether in the aircraft tail), or still in the case of a four-tether LEI tube kite. On the other hand, $\Delta\alpha$ depends on $\mathbf{v}_a$, which in turn depends on the kite velocity $\mathbf{v}_k$ and, therefore, on the kite dynamics. Other authors, as Fechner et al. (2015), refer to a *de-powering angle* $\alpha_d = \alpha_{0,o} - \alpha_0$, where $\alpha_{0,o}$ is the base angle of attack used during the traction phase. When going into the retraction phase, de-powering is applied by making $\alpha_d > 0$, which means that α_0 decreases, and so does the angle of attack α. As a consequence, the lift and the tether traction force fall as well. For a null roll angle ψ, the base angle of attack can be interpreted as the angle between the airfoil chord direction – represented by the unitary vector $\mathbf{x}_b$ – and the tangent plane $(\mathbf{e}_\theta, \mathbf{e}_\phi)$. Let us now consider the projection of $\mathbf{v}_a$ onto the tangent plane:

$$\mathbf{v}_{a,\tau} = (\mathbf{e}_\theta \cdot \mathbf{v}_a)\,\mathbf{e}_\theta + (\mathbf{e}_\phi \cdot \mathbf{v}_a)\,\mathbf{e}_\phi = \mathbf{v}_a - (\mathbf{e}_r \cdot \mathbf{v}_a)\,\mathbf{e}_r. \tag{2.13}$$

If $\Delta\alpha \neq 0$ then $\mathbf{v}_{a,\tau} \neq \mathbf{v}_a$. Let us use $\mathbf{v}_{a,\tau}$ to define the auxiliary vector

---

[5]Note that, in the case of a conventional, "untethered" aircraft, it does not make sense to divide the angle of attack into the base, α_0, and partial, $\Delta\alpha$, components.

$$\mathbf{e}_{\mathrm{w}} = \mathbf{v}_{\mathrm{a},\tau}/\|\mathbf{v}_{\mathrm{a},\tau}\|. \tag{2.14}$$

Having $\mathbf{e}_{\mathrm{r}} \perp \mathbf{e}_{\mathrm{w}}$, we complete the orthonormal basis by defining $\mathbf{e}_{\mathrm{o}} = \mathbf{e}_{\mathrm{r}} \times \mathbf{e}_{\mathrm{w}}$, as illustrated in Fig. 23. In this representation, χ is the angle between the apparent wind projection onto the tangent plane and $\mathbf{e}_{\theta}$. Observe that the plane spanned by vectors $(\mathbf{e}_{\mathrm{w}}, \mathbf{e}_{\mathrm{o}})$ coincides with the tangent plane $(\mathbf{e}_{\theta}, \mathbf{e}_{\phi})$. Also, if $\psi = 0 \Rightarrow \mathbf{y}_{\mathrm{a}} \equiv \mathbf{e}_{\mathrm{o}}$ even if $\Delta\alpha \neq 0$. Starting at this scenario, if we now have $\Delta\alpha \neq 0$ and then apply $\psi \neq 0$, $\mathbf{y}_{\mathrm{a}}$ will "detach" itself from $\mathbf{e}_{\mathrm{o}}$ and its projection onto the tangent plane will be

$$\mathbf{y}_{\mathrm{a},\tau} = \mathbf{y}_{\mathrm{a}} - (\mathbf{y}_{\mathrm{a}} \cdot \mathbf{e}_{\mathrm{r}}) \mathbf{e}_{\mathrm{r}}. \tag{2.15}$$

Figure 23 – View of the wing top surface (outside the "C") showing the angle η, here illustrated for a situation with $\Delta\alpha > 0$ and $\psi > 0$.
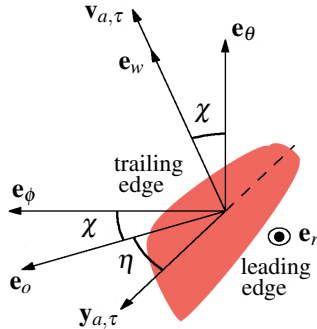
Source: original

As shown in Fig. 23, η is the angle between $\mathbf{e}_{\mathrm{o}}$ and the projection $\mathbf{y}_{\mathrm{a},\tau}$. Moreover, since $\mathbf{y}_{\mathrm{a}} \cdot \mathbf{e}_{\mathrm{r}} = \sin\psi$, then the projection of $\mathbf{y}_{\mathrm{a}}$ onto the tangent plane has norm $\|\mathbf{y}_{\mathrm{a},\tau}\| = \cos\psi$. Using this information and the commutative and distributive properties of the inner (scalar) product, let us calculate the inner product between $\mathbf{e}_{\mathrm{w}}$ and $\mathbf{y}_{\mathrm{a},\tau}$:

$$\mathbf{e}_{\mathrm{w}} \cdot \mathbf{y}_{\mathrm{a},\tau} = \|\mathbf{e}_{\mathrm{w}}\| \|\mathbf{y}_{\mathrm{a},\tau}\| \cos(\pi/2 + \eta) = \cos\psi(-\sin\eta). \tag{2.16}$$

Solving Eq. (2.16) for $\sin\eta$, using Eq. (2.15), then Eq. (2.14) and the requirement of Eq. (2.9), we get

$$\sin\eta = -\frac{\mathbf{e}_w \cdot [\mathbf{y}_a - (\mathbf{y}_a \cdot \mathbf{e}_r)\mathbf{e}_r]}{\cos\psi} = -\frac{(\mathbf{e}_w \cdot \mathbf{y}_a) - \mathbf{e}_w \cdot [(\mathbf{y}_a \cdot \mathbf{e}_r)\mathbf{e}_r]}{\cos\psi}$$

$$= -\frac{\frac{\mathbf{v}_{a,\tau}}{\|\mathbf{v}_{a,\tau}\|} \cdot \mathbf{y}_a - \mathbf{e}_w \cdot ((\sin\psi)\mathbf{e}_r)}{\cos\psi}. \tag{2.17}$$

We know that $\mathbf{e}_w \perp \mathbf{e}_r \Rightarrow \mathbf{e}_w \cdot ((\sin\psi)\mathbf{e}_r) = 0$ and that $\mathbf{v}_{a,\tau}$ is given by Eq. (2.13). Applying these results into Eq. (2.17) yields

$$\sin\eta = -\frac{\frac{[\mathbf{v}_a - (\mathbf{v}_a \cdot \mathbf{e}_r)\mathbf{e}_r]}{\|\mathbf{v}_{a,\tau}\|} \cdot \mathbf{y}_a}{\cos\psi} = -\frac{(\mathbf{v}_a \cdot \mathbf{y}_a) - [(\mathbf{v}_a \cdot \mathbf{e}_r)\mathbf{e}_r] \cdot \mathbf{y}_a}{\|\mathbf{v}_{a,\tau}\|\cos\psi}. \tag{2.18}$$

Now, using the requirements of Eq. (2.8) and Eq. (2.9) once more, we get

$$\sin\eta = \frac{(\mathbf{v}_a \cdot \mathbf{e}_r)(\mathbf{e}_r \cdot \mathbf{y}_a)}{\|\mathbf{v}_{a,\tau}\|\cos\psi} = \frac{(\mathbf{v}_a \cdot \mathbf{e}_r)\sin\psi}{\|\mathbf{v}_{a,\tau}\|\cos\psi}. \tag{2.19}$$

Finally, we solve Eq. (2.19) for η and obtain

$$\eta = \arcsin\left(\frac{\mathbf{v}_a \cdot \mathbf{e}_r}{\|\mathbf{v}_{a,\tau}\|}\tan\psi\right). \tag{2.20}$$

Recalling the geometric relations in Fig. 23, having determined η we can now express the base vector of the wing transversal axis as

$$\mathbf{y}_a = (-\cos\psi\sin\eta)\mathbf{e}_w + (\cos\psi\cos\eta)\mathbf{e}_o + (\sin\psi)\mathbf{e}_r. \tag{2.21}$$

Now let us check whether this result complies with the requirements. If we take the first requirement, of Eq. (2.8), and perform the inner product in the $(\mathbf{e}_w, \mathbf{e}_o, \mathbf{e}_r)$ basis using Eq. (2.21), Eq. (2.13) solved for $\mathbf{v}_a$, and Eq. (2.20), we arrive at

$$\begin{aligned}\mathbf{y}_a \cdot \mathbf{v}_a &= \begin{bmatrix} -\cos\psi\sin\eta & \cos\psi\cos\eta & \sin\psi \end{bmatrix}\begin{bmatrix} \|\mathbf{v}_{a,\tau}\| & 0 & \mathbf{e}_r \cdot \mathbf{v}_a \end{bmatrix}' \\ &= -(\cos\psi\sin\eta)\|\mathbf{v}_{a,\tau}\| + \sin\psi(\mathbf{v}_a \cdot \mathbf{e}_r) \\ &= -\cos\psi\frac{\mathbf{v}_a \cdot \mathbf{e}_r}{\|\mathbf{v}_{a,\tau}\|}(\tan\psi)\|\mathbf{v}_{a,\tau}\| + \sin\psi(\mathbf{v}_a \cdot \mathbf{e}_r) = 0, \end{aligned} \tag{2.22}$$

therefore the requirement of Eq. (2.8) holds true. The condition established

in Eq. (2.9) is trivially satisfied. At last, by evaluating the requirement of Eq. (2.10) using Eq. (2.21), and Eq. (2.13) solved for $\mathbf{v}_a$, we verify that

$$
\begin{aligned}
(\mathbf{v}_a \times \mathbf{y}_a) \cdot \mathbf{e}_r &= \begin{bmatrix} \|\mathbf{v}_{a,\tau}\| \\ 0 \\ (\mathbf{e}_r \cdot \mathbf{v}_a) \end{bmatrix} \times \begin{bmatrix} -\cos\psi\sin\eta \\ \cos\psi\cos\eta \\ \sin\psi \end{bmatrix} \\
&= \begin{bmatrix} -\cos\psi\cos\eta\,(\mathbf{v}_a \cdot \mathbf{e}_r) \\ -\cos\psi\sin\eta\,(\mathbf{v}_a \cdot \mathbf{e}_r) - \sin\psi\|\mathbf{v}_{a,\tau}\| \\ \cos\psi\cos\eta\,\|\mathbf{v}_{a,\tau}\| \end{bmatrix}' \begin{bmatrix} 0 \\ 0 \\ 1 \end{bmatrix} \\
&= \cos\psi\cos\eta\,\|\mathbf{v}_{a,\tau}\| > 0,
\end{aligned}
\tag{2.23}
$$

i.e. the requirement of Eq. (2.10) holds true $\forall\,\psi, \eta \in \left(-\frac{\pi}{2}, \frac{\pi}{2}\right)$, and given that $v_{a,\tau} > 0$. Keep in mind that this model is valid as long as η can be determined through Eq. (2.20). This happens if

$$
\left| \frac{(\mathbf{v}_a \cdot \mathbf{e}_r)}{(\mathbf{v}_a \cdot \mathbf{e}_w)} \tan\psi \right| \leq 1,
\tag{2.24}
$$

which means that ψ may not be arbitrarily large inside the range $|\psi| < \pi/2$ previously mentioned, depending on the combination of $\mathbf{v}_a \cdot \mathbf{e}_r$ and $\mathbf{v}_a \cdot \mathbf{e}_w$.

Having determined the apparent wind coordinate system, we can obtain the body frame simply by applying a rotation through an angle α around the transversal axis $\mathbf{y}_b \equiv \mathbf{y}_a$:

$$
\mathbf{R}_a^b = \begin{bmatrix} \cos\alpha & 0 & -\sin\alpha \\ 0 & 1 & 0 \\ \sin\alpha & 0 & \cos\alpha \end{bmatrix}.
\tag{2.25}
$$

In summary, we have used four coordinate systems in this mass-point model. The rotations among these frames are parameterized by the variables under the arrows, shown in Fig. 24.

Figure 24 – Coordinate systems in the point-mass model of the tethered wing, and the rotations involved.

nominal wind (inertial) $\xrightarrow{(\theta,\phi)}$ local $\xrightarrow{(\chi,\Delta\alpha,\psi)}$ apparent wind $\xrightarrow{(\alpha)}$ body
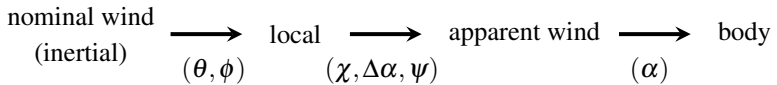
Source: original

One important observation on this point-mass model arises from the fact that the body frame is obtained by a rotation through an angle α around

the lateral axis $\mathbf{y}_a \equiv \mathbf{y}_b$. Imagine a situation where the kite is parked at the border of the wind window, around the zenith position. If the equilibrium is perturbed, for instance by increasing α_0 (and consequently α), the drag force increases and the kite may move "backwards", i.e. $\mathbf{v}_k \cdot \mathbf{v}_w > 0$. If the backward motion is fast enough so that $\mathbf{v}_k \cdot (\mathbf{v}_w / \|\mathbf{v}_w\|) > \|\mathbf{v}_w\|$ then, according to Eq. (2.5), the apparent wind speed $\mathbf{v}_a$ becomes negative. In this case, the apparent wind longitudinal axis $\mathbf{x}_a$ in Eq. (2.6) would be inverted, which means the kite would suddenly rotate $180°$ around its vertical axis – an unrealistic behavior. Because of such limitation, this point-mass model is not adequate for studying the dynamic behavior of the wing at the border of the wind window.

2.2.2 Dynamics

The equations of motion can be constructed using classical mechanics. Knowing that the kite position vector in the nominal wind frame is given by Eq. (2.1), the kite velocity is

$$\mathbf{v}_{k,[n]} = \dot{\mathbf{r}} = \begin{bmatrix} \dot{r}\sin\theta\cos\phi + r\dot{\theta}\cos\theta\cos\phi - r\dot{\phi}\sin\theta\sin\phi \\ \dot{r}\sin\theta\sin\phi + r\dot{\theta}\cos\theta\sin\phi + r\dot{\phi}\sin\theta\cos\phi \\ \dot{r}\cos\theta - r\dot{\theta}\sin\theta \end{bmatrix}. \qquad (2.26)$$

Recalling the assumption that the n_t tether(s) (1 or 2), of volumetric mass density ρ_t and diameter d_t, are perfectly straight and inelastic (similarly to a rod), the total tether mass

$$m_t(r) = (1/4)\, n_t\, \rho_t\, \pi\, d_t^2\, r \qquad (2.27)$$

can be assumed to be concentrated at half the tether length. Thus we have the equivalent tether mass position $\mathbf{r}_t = (1/2)\,\mathbf{r}$ and the equivalent tether velocity $\mathbf{v}_t = (1/2)\,\mathbf{v}_k$. Now we can build the system Lagrangian

$$L(\mathbf{q}) = T(\mathbf{q}) - V(\mathbf{q}), \qquad (2.28)$$

where $\mathbf{q} = (\theta, \phi, r)$ are the *generalized coordinates*, and $T(\mathbf{q})$ and $V(\mathbf{q})$ are the kinetic and potential energy shares, respectively. Denoting the gravitational acceleration constant as g, by performing the calculations we obtain

$$T(\mathbf{q}) = \frac{1}{2}\left(m + \frac{1}{4}m_\text{t}\right)\mathbf{v}_\text{k}^2 = \frac{1}{2}m_\text{eq}\left[\dot{r}^2 + r^2\left(\dot{\theta}^2 + \dot{\phi}^2\sin^2\theta\right)\right]$$

$$V(\mathbf{q}) = \left(m + \frac{1}{2}m_\text{t}\right)g\,r\cos\theta,$$

(2.29)

where the equivalent mass for the airborne dynamics is

$$m_\text{eq} = m + (1/4)\,m_\text{t}. \tag{2.30}$$

Let us consider the sum of all external (non-conservative) forces acting upon the point-mass wing and tether, translated to the wing position $\mathbf{r}$, as $\sum\mathbf{F}_\text{ext}$. Then we can find the expression of the kite dynamics by solving the Euler-Lagrange equation

$$\frac{\partial L(\mathbf{q})}{\partial q_\text{i}} - \frac{d}{dt}\frac{\partial L(\mathbf{q})}{\partial \dot{q}_\text{i}} + \sum\mathbf{F}_\text{ext}(i) = 0, \tag{2.31}$$

where $\sum\mathbf{F}_\text{ext}(i)$ is the sum of the external forces in each q_i direction. By doing the calculations we get

$$\begin{bmatrix}\ddot{\theta}\\ \ddot{\phi}\\ \ddot{r}\end{bmatrix} = \frac{1}{m_\text{eq}}\begin{bmatrix}(1/r)(\mathbf{G}+\mathbf{P}+\sum\mathbf{F}_\text{ext})\cdot\mathbf{e}_\theta\\ (1/(r\sin\theta))(\mathbf{G}+\mathbf{P}+\sum\mathbf{F}_\text{ext})\cdot\mathbf{e}_\phi\\ (\mathbf{G}+\mathbf{P}+\sum\mathbf{F}_\text{ext})\cdot\mathbf{e}_\text{r}\end{bmatrix}, \tag{2.32}$$

where the weight upon the airborne mass is

$$\mathbf{G} = g\begin{bmatrix}(m+(1/2)\,m_\text{t})\sin\theta\\ 0\\ -(m+m_\text{t})\cos\theta\end{bmatrix}, \tag{2.33}$$

and the apparent forces (centrifugal and Coriolis) are

$$\mathbf{P} = m_\text{eq}\begin{bmatrix}\dot{\phi}^2 r\sin\theta\cos\theta - 2\dot{r}\dot{\theta}\\ -2\dot{\phi}\left(\dot{r}\sin\theta + r\dot{\theta}\cos\theta\right)\\ r\left(\dot{\theta}^2 + \dot{\phi}^2\sin^2\theta\right)\end{bmatrix}. \tag{2.34}$$

Observe how the results obtained for $\mathbf{G}$ and $\mathbf{P}$ are slightly different from those published by Fagiano (2009). First of all, in that work it was considered the same magnitude of the tether weight decomposition in the θ and r directions, namely $(m + (1/2)m_\text{t})\,g$, because the tether mass was assumed to be applied at half of the tether length. Nonetheless, under this same assumption, the whole tether mass m_t should, in fact, act in the radial direction $\mathbf{e}_\text{r}$, which is indeed the result in Eq. (2.33). Also, although considering

the tether mass for the system's potential energy (hence weight), the tether mass was disregarded by Fagiano (2009) for the total kinetic energy. Thus, to be more rigorous with the physics and assumptions involved, the factor $m_{eq} = (m + (1/4) m_t)$ appears in Eqns. (2.32) and (2.34) instead of only the kite (and eventually control pod) mass m.

We should note here that the validity of the results found in the literature based on the previous models of Diehl (2001) and Fagiano (2009) remains unaltered with respect to the changes here proposed. In other words, the effect of the modifications here proposed on the generated power is usually negligible[6]. The reason is that the tether mass can be often very small in comparison to the wing (and possibly control pod) mass, specially at relatively small tether lengths, where the sagging of the tether can be neglected and, therefore, where these models are better applicable.

Let us assume that the wing point-mass also corresponds to the wing aerodynamic center. According to Houska and Diehl (2007), the drag force acting upon the tether(s) of drag coefficient $C_{D,t}$, corrected for the angle of attack $\Delta\alpha$ of the apparent wind reaching the tether(s), and translated[7] to the wing aerodynamic center, is

$$\mathbf{D}_t = -\frac{1}{8} n_t \rho \, C_{D,t} \, r \, d_t (\cos \Delta\alpha) v_a^2 \mathbf{x}_a. \tag{2.35}$$

Taking into account also the wing drag coefficient $C_{D,k}(\alpha)$, we can define the total drag coefficient

$$C_D(\alpha) = C_{D,k}(\alpha) + \frac{n_t C_{D,t} \, r \, d_t (\cos \Delta\alpha)}{4A}. \tag{2.36}$$

Now we are in conditions to define two external forces that act upon the airborne system and strongly influence the flight dynamics – the aerodynamic *lift* $\mathbf{L}$, and (total) *drag* $\mathbf{D}$:

$$\begin{aligned}
\mathbf{L}(\psi) &= -(1/2) \rho \, A \, C_L(\alpha) \, v_a^2 \, \mathbf{z}_a(\psi) \\
\mathbf{D} &= -(1/2) \rho \, A \, C_D(\alpha) \, v_a^2 \, \mathbf{x}_a,
\end{aligned} \tag{2.37}$$

whose intensities depend on the projected wing area A and on the coefficients of lift, $C_L(\alpha)$, and drag, $C_D(\alpha)$, respectively. Observe that the decomposition of the lift in the nominal wind frame is determined by the roll angle ψ through $\mathbf{z}_a$. By replacing Eq. (2.37) in $\sum \mathbf{F}_{ext}$ of Eq. (2.32), and considering only the

---

[6]For the system considered in Sect. 3.2, the increase in the average reel-out power when using Fagiano's model was about 0.1 %.

[7]In fact, Houska and Diehl (2007) calculated the torque upon the tether caused by the drag integrated along the cable length. The resulting force from this torque at the upper end (wing point-mass) is then obtained by considering the tether length r.

tangent plane $(\mathbf{e}_\theta, \mathbf{e}_\phi)$ to the wing position, we obtain the equations of motion

$$\begin{bmatrix} \ddot{\theta} \\ \ddot{\phi} \end{bmatrix} = \begin{bmatrix} (1/m_{\mathrm{eq}} r)(\mathbf{G} + \mathbf{P} + \mathbf{L} + \mathbf{D}) \cdot \mathbf{e}_\theta \\ (1/(m_{\mathrm{eq}} r \sin\theta))(\mathbf{G} + \mathbf{P} + \mathbf{L} + \mathbf{D}) \cdot \mathbf{e}_\phi \end{bmatrix}. \qquad (2.38)$$

One last external force to the airborne system is the tether traction which, because of the assumption of perfectly straight tether(s), has only a component in the $\mathbf{e}_r$ direction, i.e. $\mathbf{T} = (0, 0, T)$. The magnitude of the traction force depends on the sum of all other forces as well as on the tether acceleration $\ddot{r}$. Thus, we can treat the radial dynamics of the wing translation in two ways. We can either assume we manipulate the traction force T as a control input and obtain the tether acceleration $\ddot{r}$ as a result, or vice-versa:

$$\ddot{r} = (1/m_{\mathrm{eq}})((\mathbf{G} + \mathbf{P} + \mathbf{L} + \mathbf{D}) \cdot \mathbf{e}_r - T), \text{ or} \qquad (2.39a)$$

$$T = (\mathbf{G} + \mathbf{P} + \mathbf{L} + \mathbf{D}) \cdot \mathbf{e}_r - m_{\mathrm{eq}} \ddot{r}. \qquad (2.39b)$$

Although we are not modeling the dynamics of the ground winch, i.e. the joint dynamics of the eletric machine coupled to the drum by means of a gearbox, we can still consider the ground winch inertia in the equations of motion of the airborne subsystem. To this end let us state r_{d} as the drum radius, J_{d} as the drum moment of inertia, κ as the gearbox transmission ratio $(1 : \kappa)$, and J_{e} as the electric machine moment of inertia. We can then define the *tangential mass* m_{tan} and the *radial mass* m_{rad} as

$$m_{\mathrm{tan}} = m + (m_{\mathrm{t}}/4), \qquad (2.40a)$$

$$m_{\mathrm{rad}} = (J_{\mathrm{d}} + \kappa^2 J_{\mathrm{e}})/r_{\mathrm{d}} + m_{\mathrm{tan}}. \qquad (2.40b)$$

With these new mass definitions, we can consider the ground winch inertia in the airborne dynamics by replacing m_{tan} for m_{eq} in Eqns. (2.34) and (2.38), and replacing m_{rad} for m_{eq} in Eq. (2.39).

To conclude this section we would like to highlight one feature of the adapted point-mass model here proposed: although the model developed by Diehl (2001) and Fagiano (2009) has been originally conceived for the two-tether concept, we can now use it for the four-tether concept (with separated tethers for steering and traction) by considering the amount n_{t} of tethers of significant length in terms of drag and weight. The flight control input remains as the difference in the length of the steering tethers. What changes in the four-tether configuration is that, instead of rolling the wing, the Δl com-

mand creates the spanwise deformations of bending and torsion, discussed in Sect. 2.1. In both cases, the same steering input causes the wing to change its flight direction more or less in the same way.

One last remark is that, because of the relatively complex expression of $\mathbf{y}_a$ in Eq. (2.21), which $\mathbf{L}$ depends on, it is hard to represent the equations of motion analytically in a compact form. However, if we consider the particular case of zero azimuth, the equations are significantly simplified. A flight trajectory at $\phi = 0$ is, in fact, a good choice for executing the retraction phase, since the airborne mass helps reducing the tether traction force, especially towards the end of the maneuver (near the zenith). With this motivation, let us formulate in the sequel such simplified, 2D model.

2.2.3 The zero-azimuth special case

For optimization purposes, the simpler is the model, the faster the algorithm can run, which also allows for more parameters to be optimized. Our goal now is to have models less complex than the 3D point-mass one previously discussed in order to, later on, propose an optimization strategy, in Sect. 3.2. Regarding the traction phase we will discuss, in the following section, that a good approximation is to consider the kite in dynamic equilibrium, i.e. at an approximately constant apparent speed v_a and wing position (θ, ϕ). Nonetheless, when it comes to the retraction phase of current LEI tube kites, such assumption may be quite unrealistic.

To achieve a smooth transition into the retraction phase we must ramp down the base angle of attack from the value used in the traction phase, $\alpha_{0,o}$, to the value $\alpha_{0,i}$. Because α_0 usually cannot be low (negative) enough, the polar angle typically decreases during the reel-in maneuver. Hence, as argued by Fechner and Schmehl (2013), we must work with a dynamic model instead of a "static" (in equilibrium) one. To obtain this dynamic model let us establish some assumptions. Firstly, we replace the lying eight in the flight control by a trajectory with $\phi = 0$. By doing this the airborne weight contributes to decreasing the traction force, thus allowing us to save some reel-in power. Secondly, we would like to gradually decrease $v_t = \dot{r}$ (increase the reel-in speed) during the retraction phase – in this way we avoid spending too much power while the kite is still in the high-power zone. One way to pursue this, as proposed by Vlugt, Peschel and Schmehl (2013), is to work with a traction force setpoint: as the kite leaves the high-power zone, the reel-in speed naturally increases so that the desired traction force can be maintained. To achieve a smooth transition we also ramp down the traction force setpoint from the traction phase value T_o to the retraction phase value T_i. Therefore

our control inputs will vary in the retraction phase according to

$$\alpha_0(t) = \max\{\alpha_{0,\mathrm{o}} + c_\alpha t, \alpha_{0,\mathrm{i}}\} \quad \text{and} \quad T(t) = \max\{T_\mathrm{o} + c_\mathrm{T} t, T_\mathrm{i}\}, \quad (2.41)$$

where the ramp inclinations are constant values $c_\alpha < 0$ and $c_\mathrm{T} < 0$, and the time t is counted from the moment the retraction phase starts. By applying the assumptions made here to Eqns. (2.38) and (2.39), while considering the case of traction force control and the tangent and radial masses of Eq. (2.40), we arrive at the zero-azimuth equations of motion

$$\ddot{\theta} = \frac{1}{m_{\tan} r}\left[(\mathbf{G}+\mathbf{P})\cdot\mathbf{e}_\theta + \frac{1}{2}\rho A\,(C_\mathrm{D}\,v_{\mathrm{a},\theta} - C_\mathrm{L}\,v_{\mathrm{a,r}})\,v_\mathrm{a}\right] \quad (2.42a)$$

$$\ddot{r} = \frac{1}{m_{\mathrm{rad}}}\left[(\mathbf{G}+\mathbf{P})\cdot\mathbf{e}_\mathrm{r} + \frac{1}{2}\rho A\,(C_\mathrm{D}\,v_{\mathrm{a,r}} + C_\mathrm{L}\,v_{\mathrm{a},\theta})\,v_\mathrm{a} - T\right], \quad (2.42b)$$

where the apparent wind vector is simplified to

$$\mathbf{v}_\mathrm{a} = \begin{bmatrix} v_{\mathrm{a},\theta} \\ v_{\mathrm{a,r}} \end{bmatrix} = \begin{bmatrix} v_\mathrm{w}\cos\theta - r\,\dot{\theta} \\ v_\mathrm{w}\sin\theta - \dot{r} \end{bmatrix}. \quad (2.43)$$

2.2.4 Polar angle dynamics at the border of the wind window

From the 3D mass-point two-tether wing it is also possible to derive models for the polar angle dynamics. Similarly to the zero-azimuth model, these polar angle models can be used to design flight controllers for the retraction phase, when the wing is flown out of the high-power (crosswind) zone and towards the border of the wind window, where less power is required to reel in the tether. Note that, by choosing to perform the retraction phase at a polar angle similar to the one used in the traction phase we give up on one important feature of a trajectory with $\phi = 0$, discussed in the previous section: as the wing flies around the zenith towards the end of the retraction phase, the airborne weight contributes more to decreasing the traction force, which is beneficial for a more efficient reel-in maneuver. In any case, let us here briefly discuss two models derived by Zgraggen, Fagiano and Morari (2016). These models are not used for the results in this dissertation, but they will be presented in the sequel to enrich the survey. The reader should keep in mind that, whereas the original work uses the elevation angle ϑ, we are here considering its complement, the polar angle $\theta = \pi/2 - \vartheta$.

From this point onwards we will need the notion of the *course angle* γ, which is used to represent the flight direction on the tangent plane $(\mathbf{e}_\theta, \mathbf{e}_\phi)$. To this end let us consider in Fig. 25 the projection of the wing speed vector $\mathbf{v}_k$ onto the tangent plane to the wing position vector $\mathbf{r}$ as $\mathbf{v}_{k,\tau} = \mathbf{v}_k - v_t \mathbf{e}_r$. We can then define the course angle as

$$\gamma = \arctan 2 \left(\frac{\mathbf{v}_{k,\tau} \cdot \mathbf{e}_\phi}{\mathbf{v}_{k,\tau} \cdot \mathbf{e}_\theta} \right) = \arctan 2 \left(\frac{\dot{\phi} \sin \theta}{\dot{\theta}} \right), \qquad (2.44)$$

where $\arctan 2()$ is the four-quadrant version of the $\arctan()$ function, i.e. $\gamma \in (-\pi, +\pi)$. Observe that, if the course angle is kept at $\gamma = 0$, the wing will eventually collide with the ground; $\gamma = \pm \pi/2$ means flying parallel to the ground; and $\gamma = \pm \pi$ means flying towards zenith.

Figure 25 – Course angle (γ) definition.
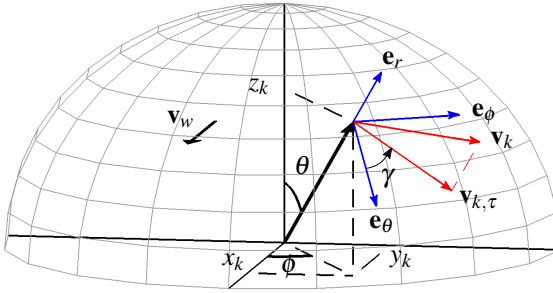
Source: original

Observe in Eq. (2.44) that the course angle loses definition whenever $v_{k,\tau} \to 0$. This is often the case when the wing reaches the border of the wind window. One way to cope with this issue is by using the nominal wind direction projected onto the tangent plane to define the orientation of the wing, and have the course angle represent such orientation. Recall that in Sect. 2.2, Eq. (2.6), we have already assumed that the wing longitudinal symmetry plane remains aligned with the apparent wind $\mathbf{v}_a$, a property that holds for rigid wings with a rudder as well as C-shaped kites. Let us then define a *regularized course angle* by considering the angle between $-\mathbf{v}_{a,\tau}$, contained in the tangent plane $(\mathbf{e}_\theta, \mathbf{e}_\phi)$, and vector $\mathbf{e}_\theta$. Based on Eq. (2.5) we have

$$\gamma_r = \arctan 2 \left(\frac{-\mathbf{v}_{a,\tau} \cdot \mathbf{e}_\phi}{-\mathbf{v}_{a,\tau} \cdot \mathbf{e}_\theta} \right) = \arctan 2 \left(\frac{r \dot{\phi} \sin \theta + v_w \sin \phi}{r \dot{\theta} - v_w \cos \theta \cos \phi} \right). \qquad (2.45)$$

Note in Eq. (2.45) that, even if $\dot{\theta}, \dot{\phi} \to 0$, as long as $v_{\mathrm{w}} > 0$ the regularized course angle remains defined. Also, from the definition of γ_r we obtain

$$v_{\mathrm{a},\tau} \cos\gamma_r = r\,\dot{\theta} - v_{\mathrm{w}} \cos\theta \cos\phi\,. \tag{2.46}$$

Let us consider the trigonometric identity $\cos\gamma_r = \sin(\pi/2 - \gamma_r)$. Furthermore, at the border of the wind window with $\phi \approx \pi/2$ we have that $\gamma_r \approx \pi/2$, allowing us to make the approximations $\sin(\pi/2 - \gamma_r) \approx \pi/2 - \gamma_r$ and $\cos\phi \approx 0$. By applying these considerations to Eq. (2.46) we obtain a linear, time-variant model for the polar angle dynamics at the border of the wind window, as a function of the regularized course angle:

$$\dot{\theta} = \frac{v_{\mathrm{a},\tau}}{r}\left(\frac{\pi}{2} - \gamma_r\right)\,. \tag{2.47}$$

Another model developed by Zgraggen, Fagiano and Morari (2016) expresses the polar angle dynamics at the border of the wind window directly as a function of the steering input. In short, such model can be obtained by taking the first row of Eq. (2.38) and assuming a steady-state equilibrium, i.e. $\dot{\phi} \approx 0$. A second assumption is that the steering input is small, so that its trigonometric functions can be linearized. After some algebraic manipulations, we arrive at the second-order, time-varying non-linear model

$$\ddot{\theta} = -\left[\frac{\rho A C_{\mathrm{L}}}{2\,r m_{\mathrm{eq}} w_s}\left(1 + \frac{1}{E_{\mathrm{eq}}^2}\right) v_{\mathrm{w}} v_{\mathrm{k}} \sin\phi\right]\Delta l + \frac{(m + \frac{1}{2}m_{\mathrm{t}})\,g\,\sin\theta}{m_{\mathrm{eq}}\,r} - \frac{2\,\dot{r}\,\dot{\theta}}{r}\,. \tag{2.48}$$

The models of Eqns. (2.47) and (2.48) can be used to design retraction phase controllers to stabilize the kite flight at a reference polar angle.

2.3 THE POINT-MASS WING IN DYNAMIC EQUILIBRIUM

We will now address a steady-state model which is often used to represent the average behavior of the tethered wing. This model will be used in Sect. 3.2.2 to optimize the reel-out power.

Let us consider the scenario depicted in Fig. 26, where $\mathbf{G_r} = (m + m_{\mathrm{t}})\,g\,\cos\theta$ is the airborne weight decomposition in the tether direction, and $\mathbf{G_\tau} = (m + (1/2)\,m_{\mathrm{t}})\,g\,\sin\theta \cos\gamma$ is the weight component in the direction of flight in the tangent plane. The wing is flying with null steering input, so that we have no "loss" of lift force (decomposition outside the plane shown in Fig. 26) as centripetal force in order to make turns.

Figure 26 – Point-mass wing flying with null steering input and subject to no apparent forces.
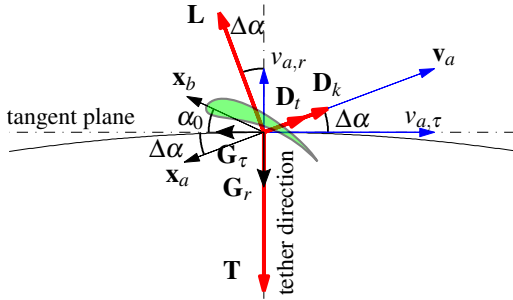
Source: original

During the traction phase the wing flies in the high-power zone, in approximate crosswind conditions. If we consider a sufficiently high glide ratio $E(\alpha)$, the relatively high aerodynamic forces allow us to neglect the weight ($\mathbf{G}_r$ and $\mathbf{G}_\tau$) and apparent forces – i.e. to neglect the airborne mass, which implies that the wing is in dynamic equilibrium (at constant speed). Furthermore, let us assume that the elevation and azimuth angles remain approximately constant. Under these assumptions, we will now reproduce some results from Schmehl, Noom and van der Vlugt (2013). Knowing that $f = v_t/v_w$ is the reel-out factor, and defining the aerodynamic coefficients

$$C_R = \sqrt{C_L^2 + C_D^2} \text{ , and } C = C_R \left(\frac{C_R}{C_D}\right)^2 , \tag{2.49}$$

the tether traction force can be approximated as

$$T = \frac{1}{2}\rho A C (\sin\theta\cos\phi - f)^2 v_w^2 , \tag{2.50}$$

while the mechanical power is, by definition,

$$P = T v_t = T f v_w . \tag{2.51}$$

We can calculate the kite tangential speed $v_{k,\tau}$ by using the factor $\lambda = v_{k,\tau}/v_w$, defined by Schmehl, Noom and van der Vlugt (2013) as

$$\lambda = a + \sqrt{a^2 + b^2 + 1 + E^2(b-f)^2} \text{ , where}$$
$$a = \cos\theta\cos\phi\cos\gamma - \sin\phi\sin\gamma \quad \text{and} \quad b = \sin\theta\cos\phi . \tag{2.52}$$

Due to its relative simplicity, we will use this model to optimize the traction phase of the pumping kite. However, it is important to highlight some limitations inherent to this model. Firstly, if the glide ratio E is not high enough, the airborne mass becomes non-negligible, which means that the wing takes more time to reach the dynamic equilibrium (or may not reach it at all), and G_r must be subtracted from the tether traction force. Moreover, an indirect effect of G_τ is that, when flying in the $\mathbf{e}_\theta$ direction, i.e. $\gamma = 0$, the wing speeds up, causing T to increase, whereas the opposite happens when the wing flies towards zenith. In fact, not only the traction force but also other system variables such as the (mechanical) power, wing speed and angle of attack – which naturally suffer cyclic variations due to the constantly varying (θ, ϕ) wing position in the wind window –, undergo stronger variations as the glide ratio is decreased. This is undesired, since we would like to have a power output as constant as possible (with the lowest variance), less stress induced on the wing and mechanical structure on the ground due to oscillations in the traction force, as well as a more constant angle of attack, kept inside a safe region (away from stall).

On the other hand, as $E = C_L/C_D$ assumes arbitrarily higher values, so does C_R and C in Eq. (2.49), and finally the mechanical power in Eq. (2.51). This obviously does not correspond to the reality; it happens because the model does not consider the feedback effect of the tethered wing upon the nominal wind field $\mathbf{v}_w$ reaching the wing. In essence, as E increases, so does the wing velocity v_k. As the wing speeds up in the approximate crosswind plane, it creates an obstacle to the nominal wind, slowing it down as the airflow reaches the wing orbit. We will discuss this "permeable wall" effect in the modeling framework used to derive the Betz limit for power extraction from the wind, to be discussed in Chap. 4.

2.4 COURSE ANGLE DYNAMICS

The course angle γ is an important system variable not only for the purpose of analysis, but also for control design. If we were to parameterize, for instance, the lying-eight figure of the traction phase by means of the spherical coordinates (θ, ϕ), we would have to control these two system outputs by manipulating the steering input Δl. Hence we would have a Single-Input Multiple-Output (SIMO) system with (coupled) dynamics described by Eq. (2.38). However, if we could parameterize the flight dynamics with a single variable, the control problem would be simplified to the SISO case. Moreover, if the proposed model were compact enough, it would be possible to design an analytical control law. Both of these modifications would

be advantageous when tackling the problem, and this is why using the course angle to parameterize the flight becomes attractive. With this motivation in mind, we will derive, in the sequel, the model for the course angle dynamics originally proposed by Fagiano et al. (2013). This model will be used in Sect. 3.1 to design flight controllers.

Consider the course angle illustrated in Fig. 25, and the kite velocity vector $\mathbf{v}_k$ defined in Eq. (2.4). From the course angle definition in Eq. (2.44) we have

$$\tan\gamma = \frac{\sin\gamma}{\cos\gamma} = \frac{\mathbf{v}_{k,\tau} \cdot \mathbf{e}_\phi}{\mathbf{v}_{k,\tau} \cdot \mathbf{e}_\theta} = \frac{\dot\phi \sin\theta}{\dot\theta}. \tag{2.53}$$

By differentiating Eq. (2.53) w.r.t. time we obtain

$$\frac{\cos\gamma(\dot\gamma\cos\gamma) + \sin\gamma(\dot\gamma\sin\gamma)}{(\cos\gamma)^2} = \frac{\dot\theta\left(\ddot\phi\sin\theta + \dot\phi\dot\theta\cos\theta\right) - \dot\phi\ddot\theta\sin\theta}{(\dot\theta)^2}. \tag{2.54}$$

The left-hand side of Eq. (2.54), when substituting $\tan\gamma = (\dot\phi\sin\theta)/\dot\theta$ from Eq. (2.53), becomes

$$\dot\gamma + \dot\gamma(\tan\gamma)^2 = \dot\gamma + \dot\gamma\left(\frac{\dot\phi\sin\theta}{\dot\theta}\right)^2. \tag{2.55}$$

If we multiply Eq. (2.55) and the right-hand side of Eq. (2.54) by $(\dot\theta)^2$, and solve the resulting equation for $\dot\gamma$, we obtain

$$\dot\gamma(\dot\theta)^2 + \dot\gamma(\dot\phi\sin\theta)^2 = \dot\theta(\ddot\phi\sin\theta + \dot\phi\dot\theta\cos\theta) - \dot\phi\ddot\theta\sin\theta$$
$$\dot\gamma = \frac{\dot\theta\ddot\phi\sin\theta + \dot\phi(\dot\theta)^2\cos\theta - \dot\phi\ddot\theta\sin\theta}{(\dot\phi\sin\theta)^2 + (\dot\theta)^2}. \tag{2.56}$$

Now we must apply the expressions (equations of motion) of $\ddot\theta$ and $\ddot\phi$ from Eq. (2.38). Note that we already have analytical expressions for $\mathbf{G}$ and $\mathbf{P}$ in the local frame, however the aerodynamic forces are defined in the apparent wind frame $(\mathbf{x}_a, \mathbf{y}_a, \mathbf{z}_a)$: $\mathbf{L}(\mathbf{z}_a)$ and $\mathbf{D}(\mathbf{x}_a)$, according to Eq. (2.37). In order to have these forces expressed in the local frame in a compact way, we need to establish some assumptions.

We start by considering once more the wing flying with (approximately) null steering input, as depicted in Fig. 26. If we assume the wing reaches a high speed relative to the nominal wind ($v_a \gg v_w$) – which can reflect a traction phase executed with a wing of high glide ratio flying in approximate crosswind conditions and at a relatively low reel-out speed –, the

airborne weight (and apparent forces) can be neglected and $\Delta\alpha$ is small. In this case, from the equilibrium of forces in the tangent plane we obtain

$$C_L \sin\Delta\alpha = C_D \cos\Delta\alpha \Rightarrow \frac{C_D}{C_L} = \frac{1}{E} = \frac{\sin\Delta\alpha}{\cos\Delta\alpha} \approx \Delta\alpha. \qquad (2.57)$$

In the equilibrium scenario of Fig. 26 we have $v_{a,r} = v_a \sin\Delta\alpha$ and $v_{a,\tau} = v_a \cos\Delta\alpha$. From these components of the apparent wind we obtain $(v_{a,r}/v_{a,\tau}) = (\sin\Delta\alpha/\cos\Delta\alpha)$. Applying this result to Eq. (2.20), along with the assumptions of a small steering input ψ and small $\Delta\alpha$, yields

$$\sin\eta = \frac{v_{a,r}}{v_{a,\tau}} \tan\psi \approx \frac{\sin\Delta\alpha}{\cos\Delta\alpha} \psi \approx (\Delta\alpha)\psi. \qquad (2.58)$$

We can also express the apparent wind speed, which we defined in Eq. (2.5), as a function of the course angle – which is interesting at this point since we are treating γ as a state whose dynamics we are trying to model. The apparent wind expression becomes

$$\mathbf{v}_{a,(l)} = \begin{bmatrix} v_w \cos\theta \cos\phi - r\dot\theta \\ -v_w \sin\phi - r\dot\phi \sin\theta \\ v_w \sin\theta \cos\phi - v_t \end{bmatrix} = \begin{bmatrix} v_w \cos\theta \cos\phi - v_{k,\tau} \cos\gamma \\ -v_w \sin\phi - v_{k,\tau} \sin\gamma \\ v_w \sin\theta \cos\phi - v_t \end{bmatrix}. \qquad (2.59)$$

Based on the assumptions of $v_a \gg v_w$, which implies that $v_{a,\tau} \approx v_{k,\tau}$, and small $\Delta\alpha$, we can simplify the vector that defines the longitudinal direction of the aerodynamic coordinate system in Eq. (2.6) to $\mathbf{x}_a = -\mathbf{v}_a/v_a \approx (\cos\gamma, \sin\gamma, -\Delta\alpha)$. This allows us to simplify the total drag force acting upon the airborne system to

$$\mathbf{D}_{(l)} \approx \frac{1}{2}\rho A C_D v_a^2 \begin{bmatrix} -\cos\gamma \\ -\sin\gamma \\ \Delta\alpha \end{bmatrix}. \qquad (2.60)$$

Note how the drag is not dependent on the roll angle ψ, created by the steering input Δl in the two-tether configuration. Regarding the lift force, we already know it is defined as a function of $\mathbf{z}_a$, which in turn depends on $\mathbf{y}_a$. According to Eq. (2.21), $\mathbf{y}_a$ depends on $\mathbf{e}_w$ and $\mathbf{e}_o$, so let us now recalculate these vectors with the assumptions just made. From Eq. (2.14) we have

$$\mathbf{e}_{\mathrm{w}} = \frac{\mathbf{v}_{\mathrm{a},\tau}}{v_{\mathrm{a},\tau}} = \frac{1}{v_{\mathrm{a},\tau}} \begin{bmatrix} v_{\mathrm{w}}\cos\theta\cos\phi - v_{\mathrm{k},\tau}\cos\gamma \\ -v_{\mathrm{w}}\sin\phi - v_{\mathrm{k},\tau}\sin\gamma \\ 0 \end{bmatrix} \approx \begin{bmatrix} -\cos\gamma \\ -\sin\gamma \\ 0 \end{bmatrix}$$

$$\mathbf{e}_{\mathrm{o}} = \mathbf{e}_{\mathrm{r}} \times \mathbf{e}_{\mathrm{w}} \approx \begin{bmatrix} 0 \\ 0 \\ 1 \end{bmatrix} \times \begin{bmatrix} -\cos\gamma \\ -\sin\gamma \\ 0 \end{bmatrix} = \begin{bmatrix} \sin\gamma \\ -\cos\gamma \\ 0 \end{bmatrix}.$$

(2.61)

Using the results above we obtain

$$\mathbf{y}_{\mathrm{a}} = (-\cos\psi\sin\eta)\,\mathbf{e}_{\mathrm{w}} + (\cos\psi\cos\eta)\,\mathbf{e}_{\mathrm{o}} + (\sin\psi)\,\mathbf{e}_{\mathrm{r}}$$
$$\approx \begin{bmatrix} (\Delta\alpha)\psi\cos\gamma + \sin\gamma \\ (\Delta\alpha)\psi\sin\gamma - \cos\gamma \\ \psi \end{bmatrix}.$$

(2.62)

Recalling that $\mathbf{z}_{\mathrm{a}} = \mathbf{x}_{\mathrm{a}} \times \mathbf{y}_{\mathrm{a}}$, we can approximate the lift force as

$$\mathbf{L}_{(1)} \approx \frac{1}{2}\rho A C_{\mathrm{L}} v_{\mathrm{a}}^2 \begin{bmatrix} (\Delta\alpha)\cos\gamma - ((\Delta\alpha)^2\psi + \psi)\sin\gamma \\ (\Delta\alpha)\sin\gamma + ((\Delta\alpha)^2\psi + \psi)\cos\gamma \\ 1 \end{bmatrix}.$$

(2.63)

Now we can apply these approximations of $\mathbf{D}$ and $\mathbf{L}$ to the equations of motion in Eq. (2.38), and replace the resulting expressions of $\dot{\theta}$ and $\ddot{\phi}$ into the expression of $\dot{\gamma}$ in Eq. (2.56). After some regrouping and algebraic simplifications, we obtain

$$\dot{\gamma} = \frac{\rho A C_{\mathrm{L}} v_{\mathrm{a}}^2 \left((\Delta\alpha)^2 + 1\right)\psi r \left[\dot{\theta}\cos\gamma + \dot{\phi}\sin\theta\sin\gamma\right]}{2 m_{\mathrm{eq}} v_{\mathrm{k},\tau}^2}$$
$$+ \frac{\rho A v_{\mathrm{a}}^2 (C_{\mathrm{L}}\Delta\alpha - C_{\mathrm{D}}) r \left(\dot{\theta}\sin\gamma - \dot{\phi}\sin\theta\cos\gamma\right)}{2 m_{\mathrm{eq}} v_{\mathrm{k},\tau}^2}$$
$$- \dot{\phi}\cos\theta - \frac{g r \dot{\phi}(\sin\theta)^2}{v_{\mathrm{k},\tau}^2}.$$

(2.64)

Note that from the course angle definition we have $(\sin\gamma)/(\cos\gamma) = (r\dot{\phi}\sin\theta)/(r\dot{\theta}) \Rightarrow \dot{\theta}\sin\gamma - \dot{\phi}\sin\theta\cos\gamma = 0$. Applying this result eliminates the second term of Eq. (2.64). Also, we know that $r\dot{\phi}\sin\theta = v_{\mathrm{k},\tau}\sin\gamma$, which we can use to simplify the fourth term of Eq. (2.64).

To simplify the first term of Eq. (2.64), let us use some approximations and properties of the models of Sects. 2.2 and 2.3. First, aiming to have an expression depending only on the wing tangential speed, let us represent v_a as a function of $v_{k,\tau}$. To this end, from Eq. (2.57) we already know that $(\sin\Delta\alpha)/(\cos\Delta\alpha) = 1/E$ and, from the decomposition of the apparent wind speed in Fig. 26, that $v_{a,r} = v_{a,\tau}(\sin\Delta\alpha)/(\cos\Delta\alpha)$. Applying these results to the apparent wind speed magnitude $v_a = \sqrt{v_{a,\tau}^2 + v_{a,r}^2}$ yields $v_a = v_{a,\tau}\sqrt{1 + (1/E^2)}$, which can be further developed with the assumption that $v_{a,\tau} \approx v_{k,\tau}$. Also from Eq. (2.57) we know that $\Delta\alpha \approx 1/E$, and from the definition of the wing tangential speed we have $r(\dot{\theta}\cos\gamma + \dot{\phi}\sin\theta\sin\gamma) = v_{k,\tau}$. Moreover, to have an expression as a function of the steering input, from Eq. (2.7) we can use the approximation $(\Delta l)/w_s = \sin\psi \approx \psi$. By applying all these developments to Eq. (2.64) we arrive at a similar result to the one obtained by Fagiano et al. (2013),

$$
\dot{\gamma} = \underbrace{\frac{\rho A C_L \left(1 + \frac{1}{E^2}\right)^2 v_{k,\tau}}{2 m_{eq} w_s}}_{c_s} \Delta l - \underbrace{\frac{g\sin\theta}{v_{k,\tau}}}_{c_g} \sin\gamma \underbrace{-\dot{\phi}\cos\theta}_{c_a}, \qquad (2.65)
$$

where c_s, c_g and c_a are the steering, gravitational, and apparent coefficients, respectively. The turning rate model in Eq. (2.65) has two differences with respect to the original result from Fagiano et al. (2013): the fact that we use θ to represent the polar angle instead of the elevation angle, and that we consider the equivalent mass for the airborne dynamics, m_{eq} of Eq. (2.30), instead of only the wing (and control pod) mass m. Observe that the first-order nonlinear model of Eq. (2.65) has a singularity when $v_{k,\tau} \to 0$, which may occur at the end of a relatively long retraction phase, for instance. Also, for $\Delta l = 0$ the system has stable equilibria at $\bar{\gamma} = \pm 2k\pi$ (flight towards the ground), as well as unstable ones at $\bar{\gamma} = \pi \pm 2k\pi$ (flight towards zenith), $k \in \mathbb{N}$. Moreover, when $\gamma \to k\pi$ the wing flies aligned with vector $\mathbf{e}_\theta$ (towards or against zenith) and the course angle dynamics behaves approximately as an integrator. Eq (2.65) represents, in fact, a non-empirical, more detailed representation of the wing flight dynamics during the traction phase with respect to previous models in the literature, as the ones proposed by Baayen and Ockels (2012), Erhard and Strauch (2012), and Lellis, Saraiva and Trofino (2013).

2.5 THE WIND SHEAR MODEL AND HISTOGRAMS

In this section we will discuss a wind shear model that is used to extrapolate the wind speed as a function of the altitude. This extrapolation is important for the pumping kite in order to determine its optimal operating height. The wind shear model will be used, from Sect. 3.2 onwards, both for simulation and optimization purposes. We will also present in this section the wind histograms. They are used to represent the frequency in which intervals of wind speed occur within a given time span (usually one year). These histograms will be used in Sect. 4.4 to compute the average power generation of both pumping kites and wind turbines.

Assuming that the pumping kite will operate inside the atmospheric boundary layer which, according to Archer (2014), extends up to $z \approx 600\,\text{m}$ above ground, we choose the *logarithmic wind shear model*

$$v_\text{w}(z) = v_\text{ref} \frac{\ln\left(\frac{z}{z_0}\right)}{\ln\left(\frac{z_\text{ref}}{z_0}\right)}, \tag{2.66}$$

where $\ln()$ is the natural logarithm[8], parameters z_ref and $v_\text{ref} = v_\text{w}(z_\text{ref})$ are the reference height and its correspondent wind speed, respectively, and z_0 is the surface roughness. The latter coefficient represents the wind gain with the altitude due to dissipative interactions (friction) of the airflow with the rough terrain. Note that this logarithmic model loses validity very fast when $z_\text{ref} > z \to 0$, i.e. when the altitude becomes very close to the ground level, in which case $v_\text{w}(z \to 0) \to -\infty$. Obviously, such conditions will not be considered in our analyses henceforth.

Wind recordings in several altitude levels are difficult to find. First of all, measuring probes are usually assembled only at two different heights on the towers of wind turbines. Hence the resolution along the height domain is low, as well as only a small fraction of the desired 600 m span is swept. Another option would be to employ remote sensing technology such as Light Detection and Ranging (LIDAR). As the acronym suggests, the technology consists of illuminating a target with a laser light. For the purpose of atmospheric and meteorology studies, it is measured the backscatter from the atmosphere in specific frequencies and polarizations. Especially in the case of sophisticated technology such as LIDAR, the collected data can be valuable for the decision-making of investors in the wind energy sector, for instance. Hence, even when the wind data exists, it is seldom available to the public for free.

---

[8] logarithm of base $e \approx 2.72$: Euler's number, also known as Napier's constant.

To cope with this we turn to the radiosonde database of the Earth System Research Laboratory (ESRL) of the National Oceanic and Atmospheric Administration (NOAA), in the USA. A radiosonde consists essentially of a battery-powered telemetry instrument package carried into the atmosphere by a weather balloon. As the balloon ascends, the on-board instruments carry out several readings such as humidity, pressure, wind speed and direction, radiation etc. All this data is transmitted to a ground station through radio waves. When a certain altitude is reached, the balloon explodes due to the low atmospheric pressure, and the instrument package falls safely by parachute so that it can be later re-launched.

For the purpose of illustrating how the power curve of pumping kites and wind turbines compare to each other in different locations, we will process data from the 3-year period between January 2013 and 2016 at different sites. This time interval corresponds approximately to that required by Brazilian authorities for the auction of wind power plants. In our case, the collected data consist of one or two soundings per day with wind measurements at different altitudes. Let us define an altitude grid with a resolution of a few tens of meters, and take the average wind speed, for the considered time period, at every grid point (slot). The slot size is chosen to ensure no slot is left empty. Then, with the resulting data set of n points (slots), the wind shear model is interpolated with the *least-squares method* by placing Eq. (2.66) in the form

$$\underbrace{\left[v_{\mathrm{w}}(z) \right]}_{\mathbf{Y}_{[n \times 1]}} = \underbrace{\left[1 \quad \ln(z) \right]}_{\mathbf{X}_{[n \times 2]}} \underbrace{\left[\begin{array}{c} -\dfrac{v_{\mathrm{ref}} \ln(z_0)}{\ln(z_{\mathrm{ref}}) - \ln(z_0)} \\ \dfrac{v_{\mathrm{ref}}}{\ln(z_{\mathrm{ref}}) - \ln(z_0)} \end{array} \right]}_{\mathbf{A}_{[2 \times 1]}}, \tag{2.67}$$

where $\mathbf{Y}$ is the set of measured outputs – a function of $v_{\mathrm{w}}(z)$ – and $\mathbf{X}$ is the set of measured inputs – a function of z. Thus, $\mathbf{A} = \begin{bmatrix} A_1 & A_2 \end{bmatrix}'$ can be calculated as $\mathbf{A} = \left(\mathbf{X}^T \mathbf{X} \right)^{-1} \mathbf{X}^T \mathbf{Y}$. By solving A_1 and A_2 for $\ln(z_{\mathrm{ref}}) - \ln(z_0)$ we find the surface roughness to be $z_0 = e^{-A_1/A_2} > 0$. Knowing that the shape of the logarithmic curve in Eq. (2.66) depends strictly on z_0, it can be shown that there are infinite solutions for the two remaining parameters. Therefore, by arbitrarily choosing $z_{\mathrm{ref}} > z_0$, we obtain $v_{\mathrm{ref}} = A_2(\ln(z_{\mathrm{ref}}) - \ln(z_0))$. In Table 3 the interpolation results for some sites in Brazil and Europe are shown.

The parameters shown in Table 3 yield the curves presented in Fig. 27. In the case of Schleswig (Germany), and for the purpose of illustration, the average wind speed of each slot is also shown as the red asterisks around the interpolated dashed curve. In fact, Schleswig is the location where the highest average wind speed is found at almost all heights, except when very close to the ground, where in Brindisi (Italy) stronger winds are verified, in

Table 3 – Interpolated parameters of the logarithmic wind shear model for different sites from January/2013 through January/2016.

Location (latitude,longitude)	z_{ref} [m]	v_{ref} [m/s]	z_0 [m]	Slot [m]
Belém/PA, Brazil $(1.38°S, 48.48°W)$	45	4.09	8.5124	30
Manaus/AM, Brazil $(3.1°S, 59.98°W)$	30	3.42	2.8739	20
Fortaleza/CE, Brazil $(3.73°S, 38.55°W)$	30	6.71	0.0052	20
Porto Velho/RO, Brazil $(8.77°S, 63.92°W)$	30	3.44	2.2000	20
Alta Floresta/MT, Brazil $(9.87°S, 56.10°W)$	30	5.41	0.0012	20
Brasília/DF, Brazil $(15.87°S, 47.93°W)$	60	5.63	0.3773	40
Confins/MG, Brazil $(19.62°S, 43.57°W)$	30	4.50	0.3932	20
Foz do Iguacu/PR, Brazil $(25.52°S, 54.58°W)$	60	6.77	0.4213	40
Florianopolis/SC, Brazil $(27.67°S, 48.55°W)$	30	4.48	0.8160	20
Porto Alegre/RS, Brazil $(30°S, 51.18°W)$	30	3.47	4.8328	20
De Bilt, the Netherlands $(52.10°N, 5.18°E)$	30	3.79	7.4770	20
Schleswig, Germany $(54.53°N, 9.55°E)$	30	5.21	3.8512	20
Brindisi, Italy $(40.65°N, 17.95°E)$	30	6.30	0.0083	20

Source: original

average. Note that the wind gain with altitude in Brindisi is low, varying only about 1 m/s in the range from 100 m to 600 m. So is the case of Fortaleza, regarded as an excellent location to operate wind power plants in Brazil. On the other hand, for locations as Schleswig, De Bilt (the Netherlands) and Belém (Brazil), the wind gain is clearly stronger. As a matter of fact, in altitudes above 250 m, Belém has a higher $v_w(z)$ than Fortaleza. For the sites where the average wind speed is already high enough to justify the deployment of power plants based on conventional wind turbine technology, the wind gain is not a decisive factor. However, at locations such as Florianópolis, Manaus and Porto Velho (all in Brazil), where the average wind speed in the altitude range ≥ 300 m becomes significant, wind power plants could be deployed if the technology were technically and economically feasible. This is one of the market niches where AWE technology is expected to become particularly competitive in the near future.

As we already discussed in Sect. 1.2, because the available wind power depends on the cube of the nominal wind speed, even slight differences in $v_w(z)$, in the order of tenths of meters per second, may turn out to be a decisive factor for the feasibility of wind power plants. However, only the

Figure 27 – Average wind curve $v_w(z)$ obtained with the wind shear model interpolated for different sites from January/2013 through January/2016.
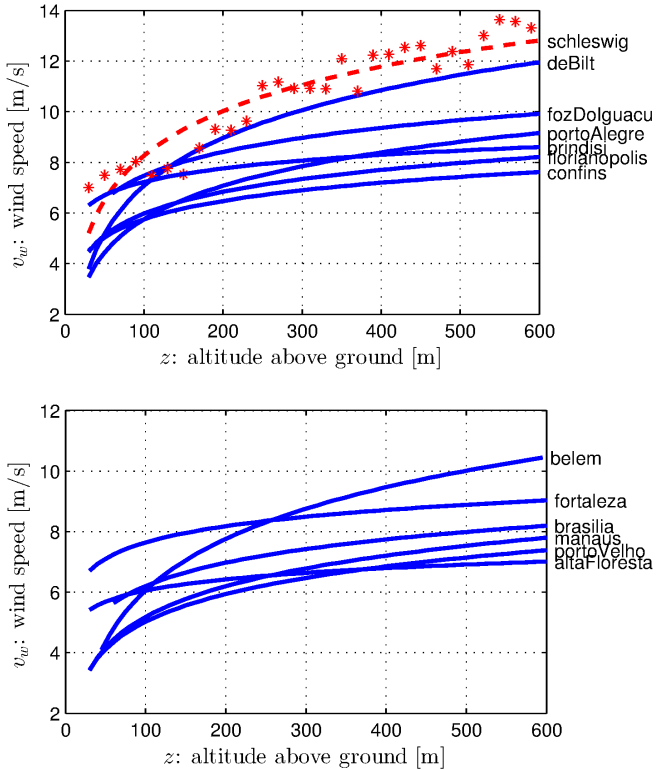
Source: original

average wind speed is not enough to characterize the potential of a given location. It is also important to know the frequency of observation of the different intervals of the wind speed. Let us take, for instance, the case of Schleswig. Imagine we have a wind turbine installed in that location, reaching 3 MW of rated power at a minimum wind speed of $v_{w,min} \approx 8$ m/s. As we will see in the power curves in Sect. 4.3.1, and considering t as the time variable, if $v_w(t)$ increases above $v_{w,min}$ the power output remains saturated at the rated value; on the other hand, if $v_w(t) < v_{w,min}$ the power output falls according to a cubic curve. Hence we would only be able to harvest, in average, the wind power correspondent to the curves in Fig. 27 if $v_w(t)$ would remain constant at the

average value for a given altitude z. This, however, is not verified in practice. For some sites the variation around the average wind speed is greater than for others. The frequency of observation f_{obs} of the different wind speed intervals can be quantified by means of the *wind histograms*. In a histogram, it must hold that $\sum_{i=1}^{k} f_{obs}(i) = 1$, where k is the number of wind speed intervals considered.

A drawback about the data obtained from ESRL is that the wind samples are often poorly distributed along the altitude range. Hence, in the case of a desired histogram whose slot contains only a few wind samples, the result is more likely to be biased. Let us keep in mind that, because the pumping kite may change its average operating altitude, it would be important to be able to compute the corresponding histogram in spite of the lack of specific data to that altitude. To cope with this we decide for the following approach: for each given wind sample $v_w(z,i)$, we apply the interpolated z_0 to find the corresponding $v_{ref}(i)$ at the chosen reference height z_{ref}. In this way we are able to build the histogram for z_{ref} and, by later calculating the pumping kite and wind turbine power curves as a function of v_{ref}, their average power production can be obtained. Also, by substituting each $v_{ref}(i)$ into Eq, (2.66) and using the same z_0, we can extrapolate the respective $v_w(z,i)$ for any altitude z. In other words, we use the specific roughness coefficient of the site – which should be time-invariant as long as the site remains unaltered – to compute the histogram for any altitude in the range where the wind shear model is valid.

For the sake of illustration, let us analyze the histograms computed for the locations of Schleswig and Brasília (Brazil), presented in Fig. 28. The reference heights are $z_{ref} = 30$ m and $z_{ref} = 60$ m, respectively, and they are represented by the starting points in the respective curves of Fig. 27. Note that $v_w(z_{ref})$ given by those curves correspond roughly to the wind speed interval with the highest observation frequency, $v_w \in (4,5)$ m/s for both locations. This correspondence between $v_w(z)$ of highest observation frequency and that given by the wind shear model is also verified for the altitudes of 100 m, where the nacelle of the wind turbines with rated power range between 3 MW and 4 MW usually operate, and for $z = 300$ m, where the pumping kites are expected to operate. Another common feature for both locations is that, as the altitude increases, so does the most frequent wind speed. However, it is evident that Schleswig offers a greater wind power potential as the altitude increases: observe how the wind distribution shifts to the right, towards higher wind speed values, whereas in the case of Brasília this shifting behavior is much less significant.

One important difference to be noted between Figs. 28a and 28b is the shape of the histograms for a same altitude: the frequency of observation of

Figure 28 – Wind histograms for three altitudes and two locations, from January/2013 through January/2016.

(a) Schleswig, Germany.

(b) Brasília, Brazil.
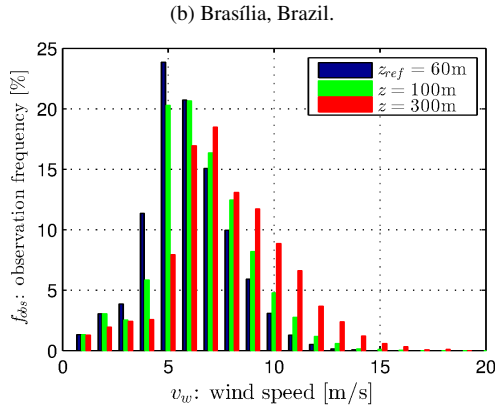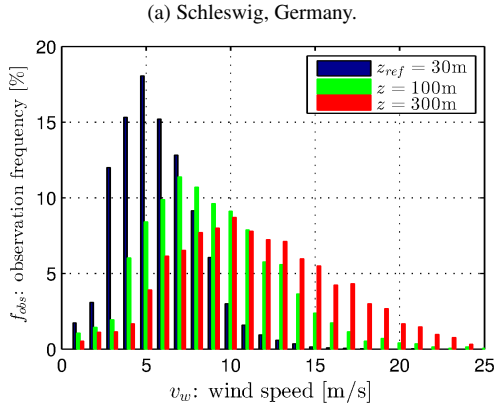
Source: original

winds in Brasília is more concentrated around the average value. For instance, at $z = 100$ m, according to Fig. 27 we have $v_w(z) \approx 6$ m/s. If we take ± 2 m/s around that average value, we can see in the histogram that about 70 % of the time the wind speed is in the interval $v_w(t) \in (4, 8)$ m/s. On the other hand, in Schleswig we have a stronger average wind $v_w(z = 100$ m$) \approx 8$ m/s but, considering the same variation of ± 2 m/s, the percentage of time in which the wind is inside the interval $v_w(t) \in (6, 10)$ m/s is only around 40 %. This means that, in Schleswig, a wind turbine whose size was chosen based on the average wind would spend 30 % less time operating at its rated power than in

Brasília, even though the average wind power is much stronger at the German site. In other words, the capacity factor tends to be lower in Schleswig than in Brasília, whereas the opposite applies to the rated power. Both of these characteristics affect the amount of wind energy harvested inside a time span (3 years, in this case). We will address more on this topic in Sect. 4.4.

3 THE PUMPING KITE

The pumping kite has been probably the most studied configuration in the literature so far. One of the reasons for this is the simple fact that controlling an AWE system comprising a single wing is simpler than with multiple wings, like the laddermill, carousel, or the dancing kites, discussed in Sect. 1.3.2. Early prototype implementations used predominantly flexible kites in detriment of rigid wings, which is partially justified by the cost criterion – LEI tube and foil kites are easily purchased from the kitesurfing and paragliding markets, respectively – and the fact that, in the case of collision during experiments, flexible kites are less likely to be damaged and to cause damage. Nonetheless, in recent years, an increasing number of research groups and companies have migrated to pumping kite implementations with rigid wings. We can name three reasons for this trend: the fact that rigid wings have a higher aerodynamic efficiency than flexible ones, the possibility of attaching small on-board propellers to solve the problem of launching and landing the wing, and the difficulty in de-powering the flexible kite for the retraction phase – a problem that has a negative impact on the net power delivered by the AWE system. Regardless of the wing type, current implementations employ only a single wing. Once the pumping kite concept becomes more mature in terms of sensing, control, materials, and safety/robustness, among other aspects, researchers will be in a better position to start experimenting with multiple-wing configurations, or even with different mechanical structures at the ground for converting the captured wind energy from the wing(s) into electricity.

As already mentioned, a pumping kite operation cycle comprises two phases. In the *traction phase* the tether is reeled out from a drum connected to the electric machine on the ground, which then acts as a generator. In order to maximize the power during the traction phase – the *traction power* – while avoiding accumulated torsion of the tether(s), Argatov and Silvennoinen (2010) showed that the optimal trajectories of the wing have the shape of a "standing figure-of-eight": an "8". However, due to the risk of losing control over the kite and having it crash when vertically fast flying towards the ground, the de-facto trajectory is usually the "lying figure-of-eight": "∞". When the tether reaches a predetermined length, the *retraction phase* (also denoted as "passive" phase) starts, during which the tether is reeled back in around the drum, with the electric machine operating as a motor. Aiming at the maximization of the cycle power – which corresponds to the net harvested mechanical energy divided by the cycle duration –, the retraction phase must be executed according to a compromise between minimization of the energy

consumption and the duration of the reel-in maneuver. The name "pumping kite" derives from this cyclic behavior of reeling out and in, i.e. adjacent traction and retraction phases, respectively.

3.1 FLIGHT CONTROL

Flight control is of fundamental importance not only for power maximization, but also for safety reasons, i.e. to avoid having the wing collide with the ground or eventual nearby obstacles. Before we address the control strategies proposed in this dissertation, let us discuss some related previous works. It is not our intention here to make an exhaustive literature review, but only to exemplify the main control approaches and their variants.

3.1.1 Previous works

In the last decade, the majority of the works found in the literature used NMPC to tackle the problem of controlling the flight of tethered wings. These works usually considered the dynamic model proposed by Diehl (2001) for the wing flight, and later some models based on that original one, in order to compute the NMPC control law. The first efforts regarding flight control trace back to Diehl, Magni and Nicolao (2004), who used the "infinite horizon closed loop costing" scheme to ensure nominal stability to control the flight of a tethered kite with a constant tether length – therefore with no energy production. In a first step, a controller based on the Linear-Quadratic Regulator (LQR) was designed to stabilize the kite locally in a periodic lying-eight orbit. Then, a two-stage NMPC optimal control problem was formulated and solved in real-time, to penalize deviations of the system state from the periodic orbit reference, considering also a state constrain to avoid collision of the kite with the ground. The numerical solution of the sequence of optimization problems was achieved through the real-time iteration scheme. The solution was based on the direct multiple shooting method, that reformulates the optimization problem as a finite dimensional non-linear programming problem with a special structure, and solves it with an iterative optimization algorithm. The real-time iteration scheme exploits the fact that, in the NMPC optimization, a sequence of neighboring optimization problems has to be solved. Thus, the solution of the previous problem can be used as an initial guess for the next iteration through a so-called "initial value embedding" strategy. This initialization procedure is so efficient that it allows to perform only one single iteration per optimization problem, without sacrificing much the solution

accuracy. Another important conclusion from the authors is that their NMPC formulation showed good robustness for model mismatch: in the presence of a side wind with a magnitude 50 % of the nominal wind, the shape of the periodic orbit changed, but remained stable.

Two years later, Canale et al. (2006) used NMPC to control the pumping kite flight, hence now including electricity generation, by means of manipulating the wing roll angle ψ (see Sect. 2.2.1). Controllers were designed for both operating phases of the pumping kite. In the traction phase, the aim was to obtain as much mechanical energy as possible from the wind, thus the chosen cost function to be minimized, at every sampling instant t_k and considering a prediction horizon T_p, was

$$J(t_k) = - \int_{t_k}^{t_k+T_p} \dot{r}(\tau)T(\tau)d\tau. \tag{3.1}$$

The resulting optimal orbit had the same lying-eight shape as previously mentioned. When the tether reached a predefined length, the passive (retraction) phase, which was subdivided into three stages, started. In the first stage, the reel-out speed $\dot{r}$ was smoothly decreased to zero and the kite was brought to a region of the wind window where the apparent wind v_a, the lift force L, and consequently the traction force T, are all reduced, thus contributing to a low energy expense for the reeling-in. The cost function of the NMPC controller in the first stage of the retraction phase was

$$J(t_k) = \int_{t_k}^{t_k+T_p} \left[\theta^2(\tau) + (|\phi(\tau)| - \pi/2)^2 \right] d\tau. \tag{3.2}$$

Once $|\phi(t)| \geq \phi_{II}$ and $\theta(t) \leq \theta_{II}$, where $0 < \phi_{II}, \theta_{II} < \pi/2$, the second stage started, when the tether was actually reeled in. In order to minimize the energy expense, the cost function became

$$J(t_k) = \int_{t_k}^{t_k+T_p} |\dot{r}(\tau)|T(\tau)d\tau. \tag{3.3}$$

Finally, when the tether initial length was reached, $\dot{r}$ was smoothly increased to zero and the kite was maneuvered into a region where a new traction phase could start. This was achieved with the cost function

$$J(t_{\mathrm{k}}) = \int\limits_{t_{\mathrm{k}}}^{t_{\mathrm{k}}+T_{\mathrm{p}}} \left(|\theta(\tau) - \theta_1| + |\phi(\tau)| \right) d\tau, \tag{3.4}$$

where θ_1 is the average polar angle of the allowed region for the kite flight. Because the computation time to solve the optimization problem should typically not exceed 100 ms due to the relatively fast flight dynamics, the authors proposed a fast NMPC implementation. In a few words, it consists of evaluating *offline* a certain number of values of the optimization function f, and then use these to find *online* an approximation $\hat{\mathbf{f}}$ of the solution at every instant t_{k}.

In the following years, Canale, Fagiano and Milanese (2007) and then Canale, Fagiano and Milanese (2009) used NMPC to control AWE systems both in the pumping kite and carousel configurations. In the latter case, recalling that Θ is the angular position of the carousel (see Fig. 13), and Q_{c} is the resulting torque from all the KSUs, the cost function to be minimized was

$$J(t_{\mathrm{k}}) = -\int\limits_{t_{\mathrm{k}}}^{t_{\mathrm{k}}+T_{\mathrm{p}}} \left[\dot{r}(\tau)T(\tau) + \dot{\Theta}(\tau)Q_{\mathrm{c}}(\tau) \right] d\tau. \tag{3.5}$$

Fagiano (2009), and an year later Fagiano, Milanese and Piga (2010), extended these results by taking into consideration the wind shear behavior and wind histograms at some sites to better exemplify the advantages of working at high altitudes, culminating in a significantly higher capacity factor than that of the conventional wind turbines. It was also investigated how the power output of the pumping kite varies with system parameters like the kite area, tether length and aerodynamic efficiency.

Houska and Diehl (2007) also used the optimal control approach, with a direct multiple shooting method, to control a pumping kite. The objective function to be maximized was the cycle power, and the control inputs were the reeling speed $\dot{r}$, the roll angle ψ, and the coefficient of lift C_{L}. Besides considering control constraints (saturation), they aimed at a closed periodic orbit, i.e. one that repeats itself with the same starting and finishing 3D points. The optimal trajectories, again, turned out to be lying-eights. This time, however, due to the closed-orbit constraint, the figure was not symmetric: the side of the lying-eight which contained the reeling-in segment had a significantly larger perimeter, allowing the needed time to retrieve all the released cable during the traction phase.

Ilzhöfer, Houska and Diehl (2007) further used the NMPC approach with direct multiple shooting and closed (periodic) orbit constraint for the trajectory solution. An optimal reference trajectory with a fixed period of 20 s

was predetermined for each nominal wind speed v_w inside a given set. Then, the NMPC task was, at every iteration t_0, and given a prediction horizon T_p, to find the sequence of control inputs that achieves

$$\min_{\mathbf{x}(\cdot),\mathbf{u}(\cdot)} \int\limits_{t_0}^{t_0+T_p} \left(\|\Delta\mathbf{x}(t)\|_Q^2 + \|\Delta\mathbf{u}(t)\|_R^2 \right) dt + \|\Delta\mathbf{x}(t_0) + T_p\|_{P(t_0+T_p)}^2 , \qquad (3.6)$$

where $\Delta\mathbf{x}(t) = \mathbf{x}(t) - \mathbf{x}_{\text{ref}}^{v_w}(t)$ is the state deviation, $\Delta\mathbf{u}(t) = \mathbf{u}(t) - \mathbf{u}_{\text{ref}}^{v_w}(t)$ is the control input deviation, and Q, R and P are penalizing diagonal matrices of the current state, control input, and final state, respectively.

Continuing with the NMPC approach, Williams, Lansdorp and Ockels (2007) studied the use of power kites for two applications: the towing of ground vehicles and electric power generation on the ground – the latter in the pumping kite configuration. A mass-point model was derived for the kite using crosswind angular coordinates other than the ones used in Sect. 2.2.1. For the purpose of power generation, it was assumed that the derivatives of the kite angle of attack α, roll angle ψ, and the tether reeling speed $\dot{r}$ were controlled. The flight trajectories were constrained to periodic closed ones, and the goal of the optimizer was to find a (pseudo-) control input $\mathbf{u}(t) = \{\dot{\alpha}, \dot{\psi}, \ddot{r}\}$ that minimizes the combined cost function

$$J = \int\limits_{t_0}^{t_f} \left[-\frac{T(t)\dot{r}(t)}{t_f - t_0} + W_3 \left(\dot{\alpha}^2(t) + \dot{\psi}^2(t) + W_4 \ddot{r}^2(t) \right) \right] dt , \qquad (3.7)$$

where t_0 is the initial time, t_f is the final time, and W_3 and W_4 are weighting coefficients to penalize the control action. Later on, Williams, Lansdorp and Ockels (2008) used the trajectories obtained offline with Eq. (3.7) as reference values for an online tracking control based on two loops. The outer loop generated a full constrained nonlinear trajectory using NMPC based on the state estimate taken at the outer-loop sampling time. In turn, the inner loop employed unconstrained linear receding horizon control to track the outer loop reference. The resulting control signals were clipped at their saturation values, if needed. It was claimed that such two-loop control strategy allows fast enough update rates (small latency) to ensure the system stability. Also, the proposed state estimator reconstructed all system states out of the assumed noisy measurements from the Global Positioning System (GPS) sensor at the kite, tether traction force, tether length and reeling speed measured at the ground winch. The used estimator was a square-root version of the unscented

Kalman Filter.

From the year 2012 onwards, the trend has shifted from the MIMO centralized control approach – which was tackled through NMPC – to a SISO decentralized one based on the wing course angle, discussed in Sects. 2.3 and 2.4. Here we use the term *decentralized* to refer to a topology where the control laws of the kite flight and ground winch are computed separately. One of the first works under this new paradigm was published by Baayen and Ockels (2012), who used the *turning angle* concept from differential geometry – an approximation of the kite course angle – in a two-loop strategy to control the flight of the pumping kite in the traction phase: the outer loop computed a target flight trajectory in terms of a turning angle reference, whereas the inner loop tracked this reference by using an adaptive Lyapunov-based nonlinear control that manipulates the differential length of the steering lines. An estimator was designed, which maintains and updates an internal representation of the steering control derivatives.

In the scope of this doctoral dissertation, in the following year, Lellis, Saraiva and Trofino (2013) employed a similar strategy to control the kite flight. The main differences with respect to Baayen and Ockels' work were the use of Bernoulli's lemniscate in the outer loop as a reference for the lying-eight figure, the offline identification of the model used for the course angle dynamics, and the design of a feedback linearization controller based on that identified model. Since then the control strategy has been constantly refined, aiming at practical implementation in a prototype, and also extended for the retraction phase. We will now discuss, in the sequel, the improvements made on the two-loop decentralized flight control, comparing the continuous reference with Bernoulli's lemniscate to a "bang-bang" strategy with only two points of reference, and three different course angle controllers for the inner loop.

3.1.2 Proposed strategy

As we have seen, initial studies on the control of tethered wings employed mostly NMPC in a centralized, MIMO topology, as investigated by Fagiano (2009), Houska and Diehl (2007), and Ilzhöfer, Houska and Diehl (2007). In a few words, the approach consists of computing the control inputs for the flight (steering) and the ground winch (reel speed) of the pumping kite system by solving an optimization problem to maximize the average power in a pumping cycle – the cycle power. In this case, the references are jointly determined resulting in a coupled solution, in the sense that the flight trajectory is not predefined, but results from the optimization problem, that must be

solved within a sampling time typically smaller than 100 ms, according to the experience of Fechner and Schmehl (2012). Despite its advantages, NMPC may be quite a demanding task to solve at such a fast rate, especially for more complex, accurate models.

Alternatively, a decentralized control topology has received increasing attention in recent years, e.g. through the works of Fagiano et al. (2013), Jehle and Schmehl (2014), and Erhard and Strauch (2015). Keeping in mind that the complete pumping kite system can be viewed as a connection of two distinct parts – the wing flight subsystem and the ground winch subsystem –, the idea is to design a decentralized[1] control for the pumping kite, in the sense that the control loops use only variables available locally, and the computed control action is also applied only to the considered subsystem. Decentralized control is normally used to improve robustness of the control strategy against failures in the communication between the subsystems, as e.g. failures in the data link between the ground station and the airborne control pod.

Regarding the flight subsystem, we can use the turning rate law of Eq. (2.65), derived in Sect. 2.4, which is a SISO system compact enough to allow for an analytical control law. The idea is to use a cascade scheme comprising two (or more) loops, as shown in Fig. 29. An advantage of this approach is that it allows for a parameterization of the flight trajectory in the outermost loop, either from a continuous reference or from some points of reference. In the inner loop the steering input of the wing subsystem is manipulated to control the course angle, whose reference is generated in the outer loop based on the wing position relative to the reference trajectory.

Figure 29 – Cascade flight control based on the course angle dynamics.
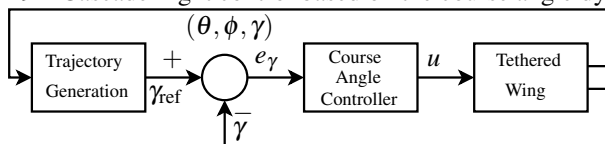
Source: original

3.1.2.1 Outer loop: trajectory generation

For the traction phase, one common strategy found in the literature is to parameterize the trajectory in terms of a few attraction points (attrac-

---

[1] More information and detailed examples on decentralized control were compiled e.g. by Bakule (2008).

tors), as used e.g. by Erhard and Strauch (2012), Vlugt, Peschel and Schmehl (2013), and Fagiano et al. (2013). These attractors are usually at the right and left edges of the lying eight, and serve as a steady reference position that the wing should reach. To better exemplify, let us consider the simple state machine with two attractors in Fig. 30, and that the wing is initially flying towards the left. The attractors have the same polar coordinate θ_{attr}, and are symmetrically displaced from the center of the wind window by an azimuth distance ϕ_{attr}. The wing position in the tangent plane is represented by $\mathbf{r}_k$.

Figure 30 – "Bang-bang" state-machine for generation of the lying-eight flight pattern in the outer loop.

$$\phi \leq -\phi_{attr}$$

Use $\mathbf{r}_r = \begin{bmatrix} -\phi_{attr} \\ \theta_{attr} \end{bmatrix} - \mathbf{r}_k$ to right   to left   Use $\mathbf{r}_r = \begin{bmatrix} \phi_{attr} \\ \theta_{attr} \end{bmatrix} - \mathbf{r}_k$
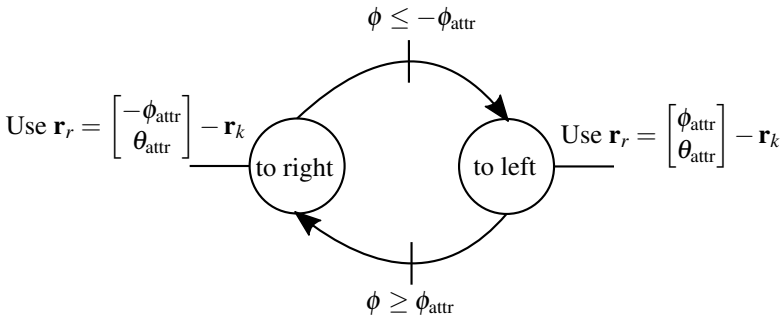
$$\phi \geq \phi_{attr}$$

Source: original

As soon as the wing crosses the positive azimuth coordinate ϕ_{attr}, the attractor at $-\phi_{attr}$ (right-hand side) becomes the active one, and vice-versa. Observe that, when the active attractor changes, the reference vector $\mathbf{r}_r$ of the wing tangential velocity suffers a discontinuity. The consequence will be a discontinuity in the tracking error of the inner loop – which is the angle between $\mathbf{r}_r$ and $\mathbf{r}_k$. In turn, a discontinuity in the control action (a "bang") may happen every time the attractor changes. Due to this characteristic, this strategy for generating the lying eight is often referred to as "bang-bang", and offers some interesting advantages. First of all, it is effective in producing a lying-eight figure using only a few tuning parameters, besides giving freedom to the wing to find its own path when moving between both sides of the wind window – which is an important feature for small trajectories. Another motivation is to avoid the need to precompute a whole trajectory based on on-line optimization, which is often dependent on an identified model of the system.

Depending on the situation, the bang-bang with two attractors may also offer some drawbacks, as the lack of a well-defined trajectory for the lying eight. For instance, as the perimeter (arc length) of the trajectory in-

creases, the tendency is the lying eight to become "squeezed" (flat) along the horizontal axis. Because previous studies, such as of Argatov and Silvennoinen (2010), have shown that the trajectory shape affects the harvested power, this relatively uncertainty in the lying eight shape obtained with the bang-bang may result in a lower power production. Zgraggen, Fagiano and Morari (2015), using the analytical model of the tethered wing in dynamic equilibrium of Sect. 2.3, showed that the average traction force (and, consequently, the harvested power) is not very sensitive on the lateral span $\Delta\phi$ of the trajectory, and that the vertical span $\Delta\theta$ should be small around the optimal value. However, the latter authors do recall that the model they employed does not capture the significant loss of speed (and force) due to performing tight turns in order to achieve a trajectory with a small span. In any case, another possible issue with the bang-bang control with two attractors, especially in the long term, is the mechanical stress induced on the steering actuator due to the discontinuity when switching between the attractors.

As an alternative approach for wide trajectories, we propose the use of Bernoulli's lemniscate, shown in Fig. 31. It has already been used for similar purposes – e.g. by Vaughn (2003) to control the trajectory of unmanned aerial vehicles – and it offers some interesting advantages to lift-mode AWE systems. First, the lemniscate resembles the optimal lying-eight trajectories investigated by Argatov and Silvennoinen (2010). Also, a smooth control action is expected when inverting the flight direction at the sides, instead of the possible discontinuity with the "bang-bang" strategy, because the lemniscate is a continuous mathematical function in these regions, as we will see. This is an interesting feature for reducing mechanical stress on the actuators. Furthermore, for being a well-defined mathematical function, it allows for an analytical approach to investigate how the parameterization of the trajectory affects system variables such as wing speed, harvested power, control input etc. Parallel to this dissertation, the use of Bernoulli's lemniscate in the decentralized, two-loop flight control scheme was also studied by Silva (2014). We will here build on those results, aiming to give more details on the implementation of the control strategy, exploring three different controllers for the inner loop, and comparing the performances of the lemniscate-based control with the bang-bang strategy.

The mathematical properties of the lemniscate were compiled, for instance, by Yates (1959)[2]. In short, the lemniscate is a 2D geometric figure with polar coordinates r_l and ω_l (radius and angle, respectively), defined by the function

---

[2]Keep in mind, though, that in the representation of Yates (1959) the lemniscate focus is $a = a_l\sqrt{2}$, where a_l is the focus considered in this dissertation.

Figure 31 – Bernoulli's lemniscate, with its four quadrants, as a reference for the lying-eight trajectory of the traction phase.

Source: original

$$r_l = f(\omega_l) = a_l \sqrt{2\cos(2\omega_l)}, \tag{3.8}$$
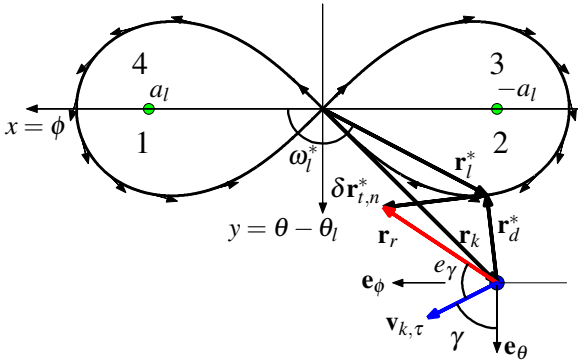
where a_l is the focal length. Eq. (3.8) yields real values – i.e. a positive radius, of physical meaning – in the interval

$$f(\omega_l) : \left[0, \frac{\pi}{4}\right] \cup \left(3\frac{\pi}{4}, 5\frac{\pi}{4}\right] \cup \left(7\frac{\pi}{4}, 2\pi\right) + 2k\pi \mapsto \mathbb{R}^+, \tag{3.9}$$

$k \in \mathbb{N}$. We will now proceed to an explanation on how the trajectory generation works. Keep in mind that the wing Cartesian coordinates in the lemniscate frame are $x = \phi$ and $y = \theta - \theta_l$, where θ_l is the polar angle of the lemniscate center. From Eq. (3.8) it follows that a generic point in the lemniscate has coordinates

$$\mathbf{r}_l = \begin{bmatrix} a_l \sqrt{2\cos(2\omega_l)} \cos\omega_l \\ a_l \sqrt{2\cos(2\omega_l)} \sin\omega_l \end{bmatrix}, \tag{3.10}$$

The tangent vector to a generic lemniscate point is

$$\mathbf{r}_t = \frac{d\mathbf{r}_l}{d\omega_l} = \frac{a_l \sqrt{2}}{\sqrt{\cos(2\omega_l)}} \begin{bmatrix} -\sin(3\omega_l) \\ \cos(3\omega_l) \end{bmatrix}. \tag{3.11}$$

Note that the norm of the tangent vector varies, depending on ω_l. In fact, it should be noted that the lemniscate function described by Eq. (3.8) has inflection points at $\omega^\dagger = \pi/4 \pm k\pi$, $k \in \mathbb{N}$, where $\|\mathbf{r}_t(\omega_l^\dagger)\| \to \infty$ and $\mathbf{r}_t$

changes direction. Thus, in order to have a continuous direction of flight, we must invert the tangent vector $\mathbf{r}_t$ on either side of the lemniscate. This was already done in Fig. 31, where the arrows representing the tangent vectors were inverted on the right-hand side ($\cos(\omega_l) < 0$) to have the wing flying down at the lemniscate edges (edge-down). For an edge-up flight, the inversion of $\mathbf{r}_t$ must be made whenever $\cos(\omega_l) \geq 0$.

The distance between a generic point in the lemniscate and the wing position $\mathbf{r}_k$ in the tangent plane is

$$\mathbf{r}_d = \mathbf{r}_l(\omega_l) - \mathbf{r}_k. \tag{3.12}$$

The idea behind the algorithm is simple: we must look in the domain given by Eq. (3.9) for the ω_l^* coordinate which minimizes $\|\mathbf{r}_d(\omega_l)\|$ in Eq. (3.12), and scale the normalized, sign-corrected tangent vector $\mathbf{r}_{t,n}(\omega_l^*)$ by a factor δ. We must normalize $\mathbf{r}_t$ because its norm varies with ω_l, as already discussed. The reference vector for the wing tangential velocity is then computed as

$$\mathbf{r}_r = \mathbf{r}_l(\omega_l^*) - \mathbf{r}_k + \delta\mathbf{r}_{t,n}(\omega_l^*), \tag{3.13}$$

where δ represents the tangential distance that the wing needs to cover in order to reach the lemniscate if the lemniscate were a straight line. In other words, δ acts as an *inverse gain*. In the case of a straight line, if $\delta \to \infty$ the wing would fly parallel to the line (no correction), whereas if $\delta \to 0$ the wing would approach the line in a perpendicular trajectory (strongest correction). Because the lemniscate path is obviously not a straight line, there will always be a small tracking error, unless $\delta \to 0$. Such a tuning should be avoided in practice, though, since it would cause the control action to constantly saturate.

Observe that, in the scheme of Fig. 29, the outer loop is providing a reference γ_{ref} to the inner loop. However, there is an inherent problem with using a course angle reference: because $\gamma \in (-\pi, +\pi)$, as defined in Eq. (2.44), if $\mathbf{r}_r \times (-\mathbf{e}_\theta)$ happened to change sign, there would be a discontinuity in γ_{ref}, switching from $+\pi$ to $-\pi$. In this scenario, if $\gamma \times (-\mathbf{e}_\theta)$ did not change sign, then the control error $e_\gamma = \gamma_{ref} - \gamma$ would also suffer a strong discontinuity and a sign inversion, which could lead to instability and eventual crash. To cope with this we choose to define the control error in terms of the relative angular displacement between γ_{ref} and γ, regardless of their orientation with respect to $(\mathbf{e}_\theta, \mathbf{e}_\phi)$. To this end, let us consider that

$$\mathbf{r}_r \times \mathbf{v}_{k,\tau} = (b_1, b_2, b_3), \tag{3.14}$$

where b_3 is the coordinate perpendicular to the lemniscate plane (x, y). If $b_3 \geq 0$ then it means that $\mathbf{r}_r$ is "in front" of or collinear with $\mathbf{v}_{k,\tau}$, i.e. $e_\gamma \geq 0$,

else $e_\gamma < 0$. Based on this reasoning, we define the control error as

$$e_\gamma = \arctan 2 \left(\frac{\|\mathbf{r}_r \times \mathbf{v}_{k,\tau}\|}{\mathbf{r}_r \cdot \mathbf{v}_{k,\tau}} \operatorname{sign}(b_3) \right) . \tag{3.15}$$

Let us now discuss some particularities when implementing the control strategy here proposed. First, in order to look for a solution which yields the desired eight-figure trajectory, we must define an appropriate quadrant to search for ω_l^*. Each quadrant has its domain, according to Table 4.

Table 4 – Lemniscate ω_l-domain depending on the active quadrant.

Quadrant	ω_l domain
1	$[0, \pi/4]$
2	$(3\pi/4, \pi]$
3	$(\pi, 5\pi/4]$
4	$(7\pi/4, 2\pi)$

Source: original

In principle, we could set the active quadrant depending on the (x, y) wing position in the lemniscate frame and the desired sequence of quadrants to be observed: $1 \rightarrow 3 \rightarrow 2 \rightarrow 4$ when flying edge-down, and $1 \rightarrow 4 \rightarrow 2 \rightarrow 3$ when going edge-up. At each sampling time, an ω_l^* solution should be found either in the current active quadrant or in the next one in the predefined sequence. This approach, however, has some issues in the case of smaller trajectories, where the angular dynamics is faster and the tracking error becomes relatively large so that the predefined sequence of quadrants may be hard to guarantee. It proved to be a more robust strategy choosing a quadrant based on the kite x-coordinate and its horizontal speed $\dot{x} = \dot{\phi}$. By doing so we avoid the need to necessarily switch from one quadrant to the next expected one: the active quadrant (hence the search domain) is chosen based on where the kite is, where it is going to, and the direction of flight (edge-down or edge-up), according to Algorithm 1.

When the quadrant changes, we redefine the solution from the previous iteration, $\omega_l^*(i-1)$, as the beginning of the new quadrant interval, depending on the direction of flight. Centered at $\omega_l^*(i-1)$ we apply a search window $\Delta\omega_l$ which must be contained within the quadrant interval. Such window is important in order to avoid finding a solution, based on the perpendicularity condition to be discussed in the following, which in fact does not correspond to the least distance $\|\mathbf{r}_d^*\|$ between the wing position and the lemniscate. This is another problem that may occur especially with tighter trajectories, when the tracking error tends to increase. The search domain is

Algorithm 1: Choice of active quadrant to search for a lemniscate solution ω_l^*.

if $x \geq 0$ then

  if $\dot{x} \geq 0$ then

    if *edge-down* then
    | quadrant = 4;
    else
    | quadrant = 1;
    end

  else

    if *edge-down* then
    | quadrant = 1;
    else
    | quadrant = 4;
    end

  end

else

  if $\dot{x} \geq 0$ then

    if *edge-down* then
    | quadrant = 2;
    else
    | quadrant = 3;
    end

  else

    if *edge-down* then
    | quadrant = 3;
    else
    | quadrant = 2;
    end

  end

end

Source: original

set according to Algorithm 2.

Algorithm 2: Definition of the search domain for ω_l^* to be used with the perpendicularity condition.

if *quadrant* $== 1$ **then**
$\quad\Big|\quad$ domain $= \left[\max\{\omega_l^*(i-1)-\frac{\Delta\omega_l}{2},0\},\min\{\omega_l^*(i-1)+\frac{\Delta\omega_l}{2},\frac{\pi}{4}\}\right]$;
else if *quadrant* $== 2$ **then**
$\quad\Big|\quad$ domain $= \left[\max\{\omega_l^*(i-1)-\frac{\Delta\omega_l}{2},3\frac{\pi}{4}\},\min\{\omega_l^*(i-1)+\frac{\Delta\omega_l}{2},\pi\}\right]$;
else if *quadrant* $== 3$ **then**
$\quad\Big|\quad$ domain $= \left[\max\{\omega_l^*(i-1)-\frac{\Delta\omega_l}{2},\pi\},\min\{\omega_l^*(i-1)+\frac{\Delta\omega_l}{2},5\frac{\pi}{4}\}\right]$;
else if *quadrant* $== 4$ **then**
$\quad\Big|\quad$ domain $= \left[\max\{\omega_l^*(i-1)-\frac{\Delta\omega_l}{2},7\frac{\pi}{4}\},\min\{\omega_l^*(i-1)+\frac{\Delta\omega_l}{2},2\pi\}\right]$;
end
Source: original

Our first strategy to find ω_l^* derives from the fact that, when $\|\mathbf{r}_d(\omega_l)\|$ is minimum, $\mathbf{r}_t(\omega_l)\cdot\mathbf{r}_d(\omega_l)=0$ (perpendicularity condition). However, the opposite is not necessarily true: the occurrence of $\mathbf{r}_t(\omega_l)\cdot\mathbf{r}_d(\omega_l)=0$ does not imply in minimum $\|\mathbf{r}_d(\omega_l)\|$ since we could have two conditions of perpendicularity between $\mathbf{r}_t(\omega_l)$ and $\mathbf{r}_d(\omega_l)$ in the same quadrant – therefore the importance of the $\Delta\omega_l$ window. With the search domain set, it follows that ω_l^* can be found as the solution to the equation

$$x\sin(3\omega_l)-y\cos(3\omega_l)-a_l\sqrt{2\cos(2\omega_l)}\sin(2\omega_l)=0. \qquad (3.16)$$

It may happen that, for the active (chosen) quadrant, $\nexists\ \omega_l\mid\mathbf{r}_t(\omega_l)\cdot\mathbf{r}_d(\omega_l)=0$. This may be the case, for instance, when the wing is going edge up on the right-hand side of the lemniscate, it has already crossed the x-axis, i.e. $y<0$, but still $\dot{x}<0$ due to the inner-loop tracking error. For situations like these, we can obtain ω_l^* by numerically minimizing $\|\mathbf{r}_d(\omega_l)\|$ in Eq. (3.12), given the minimization domain in Table 4. Observe that ω_l^* that minimizes $\|\mathbf{r}_d(\omega_l)\|$ also minimizes $\|\mathbf{r}_d(\omega_l)\|^2=\mathbf{r}_d(\omega_l)\cdot\mathbf{r}_d(\omega_l)$, hence

$$\omega_l^*=\arg\min\{2(a_l^2)\cos(2\omega_l)-2a_l\sqrt{2\cos(2\omega_l)}\,(x\cos\omega_l+y\sin\omega_l) \\ +x^2+y^2\}. \qquad (3.17)$$

We use the minimization strategy as a second attempt because it is computationally more expensive than finding the root of Eq. (3.16) from the

perpendicularity condition. Once ω_l^* is obtained through minimization, we only consider the solution as valid if it corresponds to an increment of arc along the lemniscate perimeter, considering the direction of flight, else we maintain the solution from the previous iteration. The pseudo-code for this check routine is in Algorithm 3.

Algorithm 3: Post-processing of ω_l^* obtained through minimization to determine whether it is a valid solution.

> **if** *edge-down AND*
> > *{[(quadrant 1 OR 4) & ($\omega_l(i)^* \geq \omega_l^*(i-1)$)] OR*
> > *[(quadrant 2 OR 3) & ($\omega_l(i)^* \leq \omega_l^*(i-1)$)]}*
> >
> > *OR*
> > *edge-up AND*
> > > *{[(quadrant 1 OR 4) & ($\omega_l(i)^* \leq \omega_l^*(i-1)$)] OR*
> > > *[(quadrant 2 OR 3) & ($\omega_l(i)^* \geq \omega_l^*(i-1)$)]}* **then**
> | solution = $\omega_l(i)^*$;
> **else**
> | solution = $\omega_l(i-1)^*$;
> **end**

Source: original

In the unlikely event that both search algorithms fail, the reference vector $\mathbf{r}_r$ remains the same as of the last iteration.

3.1.2.2 Inner loop: trajectory tracking

The role of the inner loop of Fig. 29 is to make the course angle control error e_γ, generated in the outer loop and given by Eq. (3.15), as small as possible by manipulating the steering input Δl. To choose an appropriate control technique for the inner loop we should keep in mind that the course angle reference is constantly changing with time, especially if we consider a lemniscate not too wide, in order to have the kite flight more concentrated in the high-power zone ($\phi \approx 0$). Therefore, by adding an integral action to the controller we should not expect a significant improvement in the reference tracking. For the sake of simplicity, let us then consider a proportional controller

$$\Delta l = k_p e_\gamma = k_p(\gamma_{ref} - \gamma), \tag{3.18}$$

where k_p is the proportional gain. To find the tuning of k_p to achieve a stable flight we replace the control law of Eq. (3.18) in the course angle dynamics given by Eq. (2.65), recalling that c_s, c_g and c_a are the steering, gravitational

and apparent coefficients. By linearizing the resulting closed-loop dynamics we obtain the Jacobian $J(\gamma) = -c_s k_p + c_g \cos \gamma$. Since, in this case, the Jacobian corresponds to the pole, for closed-loop stability it must be that $J(\gamma) < 0$, a condition we should analyze for three cases. If $\bar{\gamma} = 0$ the proportional gain should be $k_p > c_g/c_s$. Else, if the wing is flying parallel to the ground, $\bar{\gamma} = \pm\pi/2$ and it follows that $k_p > 0$. Finally, if the wing is flying towards zenith, with $\bar{\gamma} = \pm\pi$, then the proportional gain should be $k_p > -c_g/c_s$. Because $c_g < 0$, the more restrictive case is the latter one. We can express the proportional gain in terms of the stable closed-loop pole $p < 0$ at any linearization point $\bar{\gamma}$ as

$$k_p = \frac{c_g \cos\bar{\gamma} - p}{c_s} = -\frac{2 m_{eq} w_s (v_{k,\tau} p - g \sin\theta \cos\bar{\gamma})}{\rho A C_L (1 + \frac{1}{E^2})^2 v_{k,\tau}^2}. \qquad (3.19)$$

Another relatively simple control strategy for the inner loop is possible if we assume we know, in execution time, the identified coefficients of the course angle model in Eq. (2.65). If so, we could use a proportional controller while compensating for the non-linearities of the model. This is the idea behind the *feedback linearization* technique. To derive the control law, we differentiate the error expression $e_\gamma = \gamma_{ref} - \gamma$ w.r.t. time, substitute the course angle derivative by the open-loop dynamics of Eq. (2.65), and impose a first-order linear behavior, with pole $p < 0$, to the resulting closed-loop error dynamics. We can then solve the expression for the control input, obtaining

$$\Delta_l = \frac{\dot{\gamma}_{ref} - c_a}{c_s} - \underbrace{\frac{p + c_g \sin\gamma}{c_s}}_{k_p'} e_\gamma. \qquad (3.20)$$

It is interesting to observe that the composition of k_p and k_p' is the same for $\gamma = \bar{\gamma} = 3\pi/4 \pm k\pi$, $k \in \mathbb{N}$. In fact, the proportional gain k_p' of the feedback linearization controller in Eq. (3.20) changes as a function of $\sin\gamma$ in order to compensate for that nonlinearity. Moreover, in a separate term, the control law compensates for the apparent force and the rate of variation of the course angle reference $\dot{\gamma}_{ref}$. Nonetheless, for practical implementations, the latter variable must be used with caution, since the trajectory reference is computed by a kinematic algorithm in the outer loop and, therefore, it is not subject to a limited rate of variation. Therefore let us consider, in the simulation results that will follow, also the controller given by Eq. (3.20) but with $\dot{\gamma}_{ref} = 0$.

3.1.3 Simulation results

The simulation results to be presented in this section were obtained with a setup of the pumping kite airborne components aiming to match the characteristics of a small prototype built at UFSC to investigate flight control with no reeling capability, i.e. with a constant tether length. Regarding the tether, we will consider the *Dyneema*® technology, which combines high minimum breaking loads with small diameters and small linear densities, according to Fig. 32. The curves are very similar in shape, and were interpolated with 3rd degree polynomials.

Figure 32 – Characteristics of the Dyneema® tether.
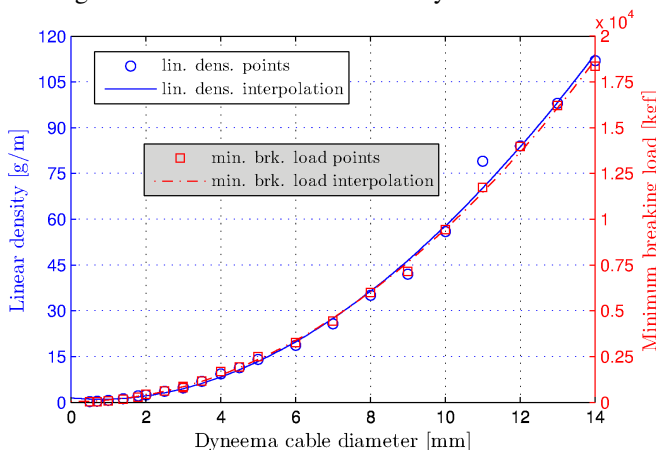
Source: data obtained from a commercial distributor

We will also consider a foil kite, with the aerodynamic curves shown in Fig. 33. These curves were borrowed from Paulig, Bungart and Specht (2013), correspond to a flat aspect ratio of 4.8, and were slightly extrapolated down to 0° and up to 40° of angle of attack. We will assume that, outside this range, the foil kite does not operate. For the sake of comparison, we also show in Fig. 33 the curves of a LEI tube kite, reproduced from Fechner et al. (2015). We highlight that the latter set of curves was not validated against experimental wind tunnel nor through Computational Fluid Dynamics (CFD) methods. Instead, these curves were obtained from empirical modifications on a wind turbine airfoil in order to reproduce the expected behavior of a LEI tube kite. Note that, because of the inflated leading-edge tube and struts, the LEI tube kite should be able to operate in a broader span of angle of attack

than the foil kite. Table 5 contains all other system parameters required for the simulations. It is important to emphasize that we are here considering a very small and constant tether length of 24 m. Hence the angular speeds $\dot{\theta}$ and $\dot{\phi}$ are very high, thus requiring a high sampling rate of the control law and a fast response of the actuators. On the other hand, for real systems used to generate electricity with a much longer tether length (typically longer than 200 m), the angular dynamics is much slower and, therefore, the sampling rate and actuator response become less critical for controlling the flight.

Figure 33 – Aerodynamic curves for a foil (ram-air) kite with aspect ratio of 4.8, and for a LEI tube kite.
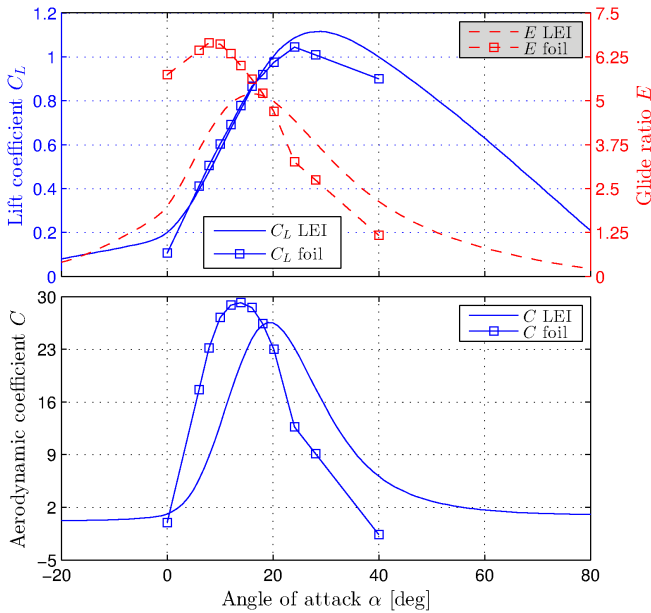
Source: data obtained from Paulig, Bungart and Specht (2013) (foil kite) and Fechner et al. (2015) (LEI tube kite)

We start by considering a constant nominal wind $v_w = 5$ m/s, and a lemniscate with focus $a_l = 25°$ centered at $\theta_l = 60°$. By choosing the edge-up direction of flight, we can expect the average course angle to be $\bar{\gamma} = \pm\pi$. Considering this value in Eq. (3.19) and a 95% settling time of 1 s, in average, we obtain the feedback gain $k_p = 0.39$ to use with the proportional controller. For the outer loop we use the inverse gain $\delta = 10°$. The simulation results are presented in Fig. 34, where the red-filled small circles indicate the completion of one orbit, when the wing crosses the lemniscate center going from the 3rd to

Table 5 – Parameterization of a small foil kite for simulations of flight control.

Description	Symbol	Value	Unit
wing mass	m	1	kg
projected wing area	A	3	m^2
projected wingspan	w_s	1	m
base angle of attack	α_0	0	deg
tether length	r	24	m
tether diameter	d_c	4	mm
minimum breaking load	T_{max}	1.495	kgf
tether volumetric density	ρ_c	656	kg/m^3

Source: original

the 1st quadrant[3]. Observe that the reference trajectory, indicated by the green dash-dotted line, is tracked with a relatively large control error. Regarding the inner loop, the tracking error peaked at about $\pm 69°$, with a standard deviation of $42.9°$, whereas the outer loop control error peaked at about $13.6°$, with standard deviation of $3.5°$. This tracking performance is due to a control action peaking at about 45 cm, which corresponds to a roll angle of about $8°$.

Note how the traction force T strongly oscillates throughout one orbit, with standard deviation of 21.2 kgf, which corresponds to approximately 38 % of the average traction force. This behavior is undesired, since it implies in an equally oscillating electric power output. It can be shown that this oscillation can be reduced by properly adjusting the lemniscate focus. Differently from the traction force, the angle of attack varies little, kept between $8°$ and $10°$. Also note how the apparent wind speed v_a is approximately the same as the wing speed v_k, corroborating the assumptions made to derive the course angle model in Sect. 2.4.

The control performance can be improved by tuning the gains of the inner and outer loops, as illustrated in Fig. 35. Observe how either decreasing the 95% settling time[4] of the inner loop (i.e. decreasing the pole given by Eq. (3.19) towards $-\infty$) as well as reducing the δ-parameter (inverse gain) of the outer loop causes both the inner and outer loop tracking errors to decrease. This improvement in the control performance comes with the cost of a more intense (higher amplitude) control signal. On the other hand, for combinations of inner loop settling time and δ-value large enough, the maximum value of the inner loop tracking error e_γ approaches its definition limit

---

[3]or vice-versa in the case of an edge-down flight.

[4]In fact we are referring to the minimum settling time of the inner loop, since we are considering the error dynamics of the inner loop linearized around $\bar{\gamma} = \pm\pi$, according to Eq. (3.19).

Figure 34 – Simulation results of a $3\,\text{m}^2$ foil kite with $v_w = 5\,\text{m/s}$, edge-up lemniscate in the outer loop, and proportional controller with average 95% settling time of $1\,\text{s}$.
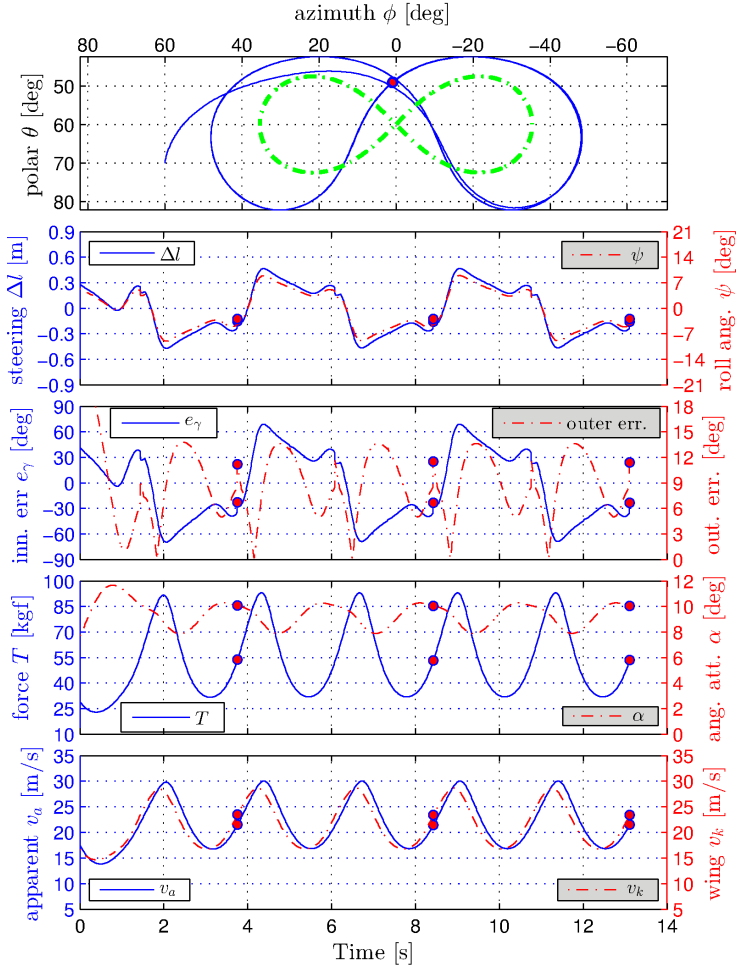
Source: original

at $180°$, which is a dangerous region to operate in because of the discontinuity around $\pm 180°$. Moreover, observe in the upper plot of Fig. 34 that the minimum angular distance from the lemniscate to the ground level is less than $20°$ (in the θ-direction). This margin of outer loop error is already trespassed for

a settling time higher than 1 s, depending on the value of δ, which means the wing would have crashed into the ground.

Figure 35 – Lemniscate tracking performance as a function of the inner loop settling time with proportional controller and the outer loop (inverse) gain.
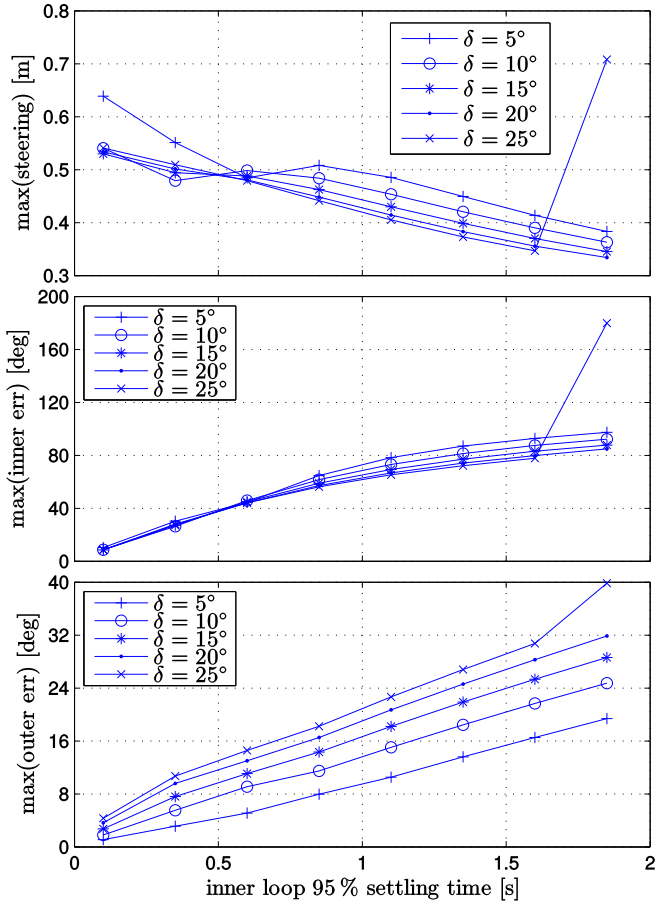
Source: original

Let us now compare the performance of the proportional controller with the feedback linearization one. We proceed as follows: for a same setting of the outer loop ($\delta = 10°$), we vary the pole p (hence the settling time) of the inner loop and obtain the corresponding feedback gain k_{p} given by Eq. (3.19) for the proportional controller, as well as the gain k_{p}' defined in Eq. (3.20) for the linearizing controller. Note that, in order to compute the

latter controller, we must assume we know all variables encapsulated by the coefficients c_s, c_g and c_a. Moreover, we will consider two implementations of the linearizing controller: one with supply of the time-derivative of the reference course angle $\dot{\gamma}_{ref}$, and another without it. The results are presented in Fig. 36. Observe that, for all three cases, the tracking performance both of the inner and outer loops deteriorates when the inner loop settling time is increased, as one could have expected. However, for almost all values of settling time analyzed, the proportional controller yields a lower maximum error for both loops when compared to the feedback linearization controller without accounting for $\dot{\gamma}_{ref}$. As for the complete implementation of the latter controller according to Eq. (3.20), it produces the better performance by far, although at the expense of a control signal that reaches higher peaks. Note that, despite the compensation of the inner loop non-linearities (assuming we know on-line the exact values of the system parameters), the tracking errors do not converge to zero, but to a region nearby. This is because the model for the course angle dynamics, given by Eq. (2.65) and used by the linearizing controller, has some errors due to approximations made w.r.t. the two-tether point-mass model of Sect. 2.2, hence the non-linear dynamics is not perfectly compensated. The inner and outer loop tracking errors could be arbitrarily decreased by adjusting the control parameters, but then stability problems could eventually arise in the presence of wind turbulence, for instance.

The results of Fig. 36 suggest that, if practical implementation issues do not allow for a smooth and accurate computation of $\dot{\gamma}_{ref}$, e.g. due to sensor noise, then the proportional controller results in a better tracking performance than the feedback linearization one without the derivative term. This conclusion holds if we consider the same closed-loop pole for both controllers, i.e. the imposed closed-loop pole with the linearizing controller, and the closed-loop pole obtained with the proportional controller at the linearization point $\bar{\gamma} = \pm\pi$. Also note that, if the parameters of the model for the course angle dynamics are not known on-line, the feedback linearizing controller becomes unfeasible even if $\dot{\gamma}_{ref}$ could be efficiently computed.

Now let us check the flight performance with the bang-bang outer-loop strategy. We used the attractor azimuth coordinate $\phi_{attr} = a_l\sqrt{2} \approx 35.4°$, which corresponds to the largest azimuth coordinate of the lemniscate, whereas the polar coordinate was the same, $\theta_{attr} = \theta_l = 60°$. In the inner loop we used the same proportional controller with $k_p = 0.39$. The results are shown in Fig. 37. Observe how the trajectory tends to become horizontally flatter. Also note the steep peaks on the steering (the discontinuity happens right before each peak), caused by the peaks in the inner loop tracking error e_γ. We do not compute the outer loop error because the trajectory is not a continuous closed-figure anymore, now consisting only of the two attractors. The

Figure 36 – Performance comparison between the proportional and Feedback Linearization (FL) controllers for tracking the lemniscate trajectory.
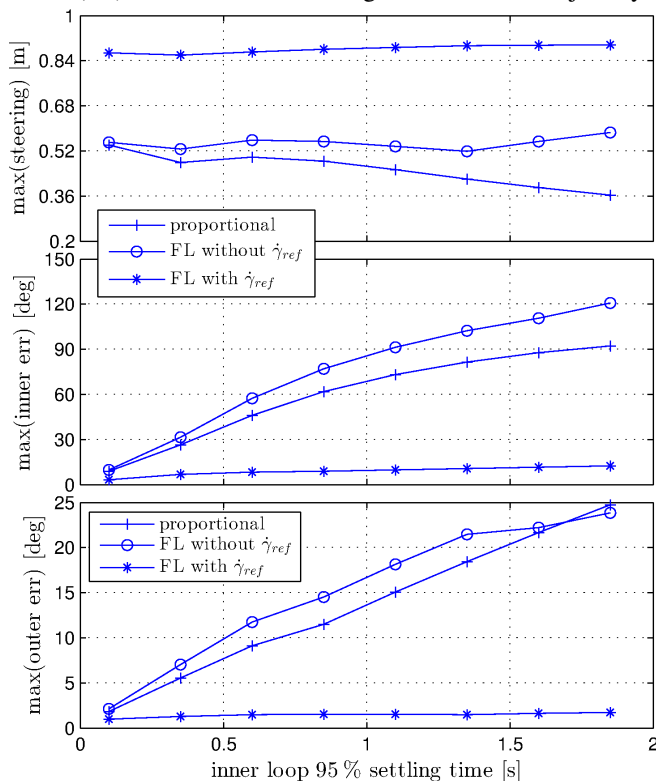
Source: original

average traction force was 48.6 kgf, which is about 13 % lower than the value obtained with the corresponding lemniscate.

To have a better feeling of how the direction of flight affects the trajectory tracking – both in the case of a continuous reference such as Bernoulli's lemniscate, as well as in the case of the two reference points of the bang-bang strategy – let us turn to the results of Fig. 38. The inner-loop was the same for all cases: the proportional controller with $k_p = 0.39$. In comparison to the edge-up lemniscate of the upper plot, observe that in the edge-down lemniscate the outer loop tracking error peaks at a higher value: the kite flies very close to $\theta = 90°$, which would mean a collision with the ground. This behavior is due to the pull of gravity, which contributes more to accelerat-

Figure 37 – Simulation results of a $3\,\text{m}^2$ foil kite with $v_w = 5\,\text{m/s}$, bang-bang edge-up strategy in the outer loop, and proportional controller with average 95% settling time of $1\,\text{s}$.
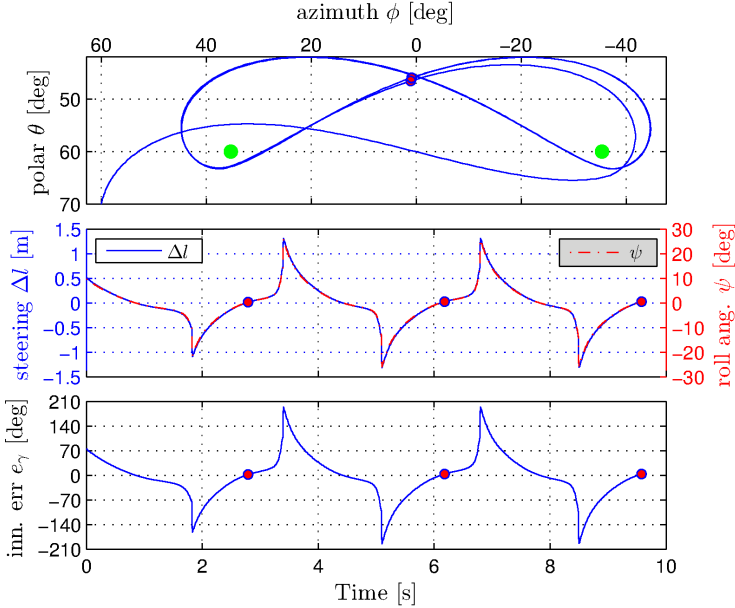
Source: original

ing the kite when the course angle crosses $\gamma = 0°$ at the lateral edges of the lemniscate. Despite the increased tracking error, flying edge-down yielded an average traction force of $64.3\,\text{kgf}$, roughly $15\,\%$ more than in the case of the edge-up lemniscate. This result is in accordance to Vlugt, Peschel and Schmehl (2013) who, in their practical experiments with a prototype, observed that "…in lightwind conditions, the downloop[5] figure eight (…) has proven to be the more efficient shape."

Regarding the bang-bang outer loop, note that in the edge-down flight (lowermost plot) the wing did not manage to turn around the attractor points: it reached the azimuth margin at a polar angle higher than θ_{attr} due to the tracking error of the proportional controller in the inner loop. One could already have expected this since, in order to "climb" above the attractor, a control error $e_\gamma > 0$ is needed. However, as $\theta \to \theta_{\text{attr}}$ the control error vanishes, and so does the control action.

---

[5] i.e. the edge-down flight direction, as denoted in this dissertation.

Figure 38 – Trajectory tracking results for Bernoulli's lemniscate and the bang-bang outer loop, with the same inner-loop proportional controller $k_\mathrm{p} = 0.39$, and for both directions of flight.
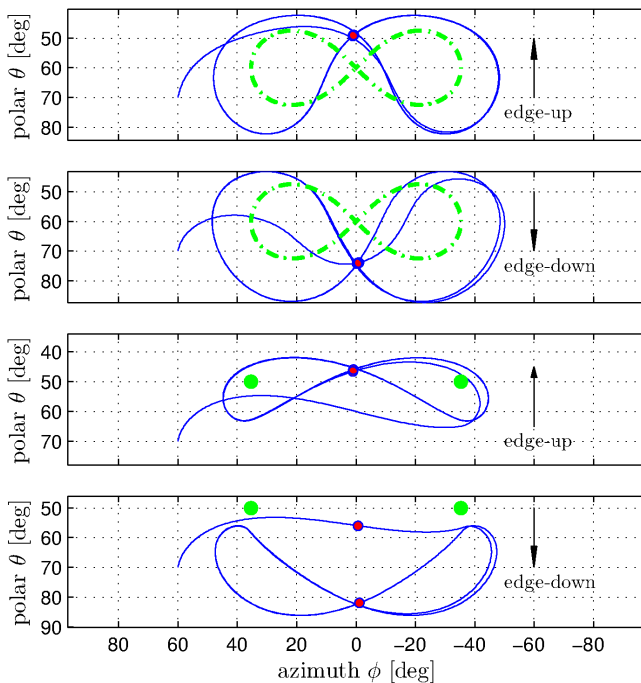
Source: original

We can also observe in Fig. 38 that, when turning edge-down towards the other attractor, the wing flied even closer to the ground than in the case of the edge-down lemniscate. In fact, the wing did not crash with the ground only because the polar coordinate of the attractors was decreased to $\theta_\mathrm{attr} = 50°$. While the edge-up bang-bang yielded an average traction force about 13 % lower than the edge-up lemniscate, the edge-down bang-bang produced an average traction force approximately 33 % higher than the edge-up lemniscate. This "excessive" increase can be explained by the resulting bang-bang edge-down trajectory with an average polar angle higher than in the edge-up lemniscate case. Let us recall that, the higher is θ, the more in crosswind the wing flies and the higher is the traction force[6], according to Eq.

---

[6]This conclusion is only valid if the nominal wind is kept constant regardless of the altitude. Because, in practice, the nominal wind tends to vary with the altitude, e.g. according to a log-

(2.50).

We would like to conclude this section by highlighting some particularities of the control strategies here discussed. Although, in the simulation environment, both the continuous reference (Bernoulli's lemniscate) and the few-points-of-reference (bang-bang with two attractors) may seem equally feasible to implement, this is not the case in a real system. Preliminary tests with a small prototype (parameterization similar to Table 5) for flight control studies have shown that a combination of factors makes it challenging to stabilize the kite flight with the lemniscate strategy. First of all, the fast angular dynamics allied with a relatively large sampling time (about 70 ms) allows for only a few updates of the control algorithm along the continuous trajectory reference. It is well known that, as the sampling time increases w.r.t. the open-loop dynamics, the closed-loop performance may deteriorate, or closed-loop stablity may even be lost at all.

Another factor to be considered is the speed saturation of the servomotor used for the steering actuator: this limitation characterizes a non-linearity that cannot be neglected for systems with faster flight dynamics. Hence, we should consider this speed saturation in the model of the open-loop system – e.g. by considering Δl in Eq. (2.65) as a state whose time derivative is limited – in order to design a more appropriate flight controller. One last factor we can mention in the real system is the delay between pulling/releasing the steering cables and the kite response in terms of the turning rate $\dot{\gamma}$. We estimate this delay to be in the order of tenths of seconds (depending on the wind speed), hence this delay becomes relevant for the considered system. Similarly to the speed saturation of the steering actuator, this transport delay should also be modeled in the open-loop dynamics used to design the flight controller.

In spite of these issues, the bang-bang outer loop with two attractors and some improvements (not discussed so far) seem to cope well with the task of stabilizing the kite flight with fast angular dynamics. As put by Vlugt, Peschel and Schmehl (2013), the idea is "... to give the kite a certain freedom to find its own path while tracking from one point to the other." By doing so we tackle the problem of the slow sampling rate relative to the system dynamics. The non-linearities of the steering speed saturation and the steering transport delay can be overcome by means of a predictive strategy in the outer loop: in order to calculate the course angle reference, instead of considering the current kite position we extrapolate the future kite position given the current turning rate $\dot{\gamma}$ and a given prediction horizon (usually between 0.5 s and 1 s). Preliminary tests with these enhancements in the control law have shown

---

arithmic wind shear model, trajectories too close to the ground tend to yield a lower traction force.

promising results, which are expected to be published soon.

Based on the same reasoning discussed above that claims the bang-bang control to be the more appropriate strategy in the case of faster flight dynamics, when it comes to slower dynamics that allow for a trajectory with a larger (arc length) perimeter, the continuous reference trajectory could become the more appropriate strategy. Especially in terms of the trajectory shape, it could already be verified (see Fig. 38) that the lying eight tends to become distorted (horizontally squeezed) with only the two attractors. This issue should be augmented as the tether length increases (and consequently the arc length of the lying-eight perimeter). If this happens, the tethered wing should loose efficiency in harvesting the wind power by deviating more from the optimal lying eight trajectories studied e.g. by Argatov and Silvennoinen (2010). One way to "correct" the lying-eight shape would be to add more points of reference: Vlugt, Peschel and Schmehl (2013) parameterized the flight trajectory with two, three and four attractors. Observe that, if the angular dynamics becomes slow enough, then the increasing sequence of points of reference could, in fact, become an approximation of a continuous trajectory.

3.2 OPTIMIZATION OF A PUMPING CYCLE

Having discussed the open-loop model of the two-tether point-mass wing in Sect. 2.2, and a corresponding flight control strategy in Sect. 3.1, we are now left with the question: what is the set of control parameters and references that maximizes the average produced power within a pumping cycle? Before we discuss the contribution of this dissertation on the topic, let us recall some related works in the literature

3.2.1 Related works

One of the first attempts to optimize a complete pumping cycle was carried out by Fagiano (2009) and Fagiano, Milanese and Piga (2011). In these papers, constant values of the polar angle θ, reel-out speed $\dot{r}$, and aerodynamic coefficients C_L (lift) and C_D (drag) for each pumping phase were assumed. It was also considered that the tether length variation Δr is negligible in comparison to the average tether length $\bar{r}$, so that r would be approximately constant during the whole pumping cycle. Under these assumptions the tether traction force T could be considered constant for each phase and, consequently, a simplified expression for the cycle power P_{cyc} was found. Two subsets of optimal solutions were proposed, $\mu_{\text{o}} = (\theta_{\text{o}}, \dot{r}_{\text{o}}, r_{\text{o}})$ for the trac-

tion and $\mu_i = (\theta_i, \dot{r}_i, r_i)$ for the retraction phase, and the optimal solution was computed as $\mu^* = \arg\max\{P_{cyc}(\mu_o, \mu_i)\}$. The solution for the azimuth angle was trivial, $\phi_o^* = \phi_i^* = 0$, for the "wing-glide maneuver"[7].

Some important remarks can be made on such approach. Firstly, in order for Δr to be negligible in comparison to $\bar{r}$, the traction phase must be short. By choosing to reel out 50 m around the optimal tether length of 611 m, i.e. $\Delta r \approx 8\% \, r^*$, the traction phase of Fagiano (2009) (p. 84) lasted about 23 s. This relatively short duration may give rise to a practical issue: if one takes into account the need for a transition maneuver between the pumping phases, and that such maneuver can take e.g. between 4 s and 10 s, this relatively long transition time may have a negative impact on the cycle power. This is because, during the transition, energy is not being optimally generated nor consumed. Secondly, keeping θ constant during the retraction phase may be a hard task to achieve in practice because pulling the wing "as a flag", as required for the wing-glide maneuver, leaves the elevation angle uncontrolled. It can also happen that the kite, especially if flexible, simply may not be de-powered as much as required to generate the needed low lift and stabilize the elevation. If this is the case, the decrease of θ during the retraction phase significantly affects the power consumption and thus should be taken into account by the optimizer. A third concern, and perhaps more importantly, is that it was not clear what angle of attack was used for the traction phase in order to run the optimization, nor was it justified the choice of the base angle of attack $\alpha_0 = 3.5°$. In other words, the angle of attack α was not (at least explicitly) considered as an argument of the optimization, although the aerodynamic curves $C_L(\alpha)$ and $C_D(\alpha)$ had been declared.

A similar approach and assumptions was used by Luchsinger (2013), who approximated the cycle power as a function of the constant values of reel-out and reel-in speeds, aerodynamic coefficients (different values for each pumping phase), and the elevation angle, which was assumed to be the same for the whole pumping cycle. However, the dependency of the system drag on the tether length was left out, as well as the wind shear model. Therefore, given θ, C_L and C_D, the only arguments to be optimized were $\dot{r}_o$ and $\dot{r}_i$. More recently, Erhard and Strauch (2015) proposed an optimization algorithm to compute the pumping cycle duration and the instantaneous values of the tether reel speed. The algorithm is based on a simplified model of the wing, similar to the one discussed in Sect. 2.3. In their approach, the authors considered a constant glide ratio (no de-powering) throughout the whole pumping cycle and showed that, by moving the kite to a position upwind of

---

[7]Fagiano (2009) also considered the "low-power maneuver" for the retraction phase, where the kite is brought to the border of the wind window at $0 < |\phi| < \pi/2$ before the tether is reeled-in.

the ground station before reeling in the tether, a significant amount of cycle power can be achieved (rather contrary to intuition).

Besides the works mentioned so far and those dealing strictly with the traction phase, only a few papers have been published focused on the retraction phase. A well-designed reel-in maneuver is essential for a higher cycle power since, regardless of the power generated in the traction phase, if that same amount is spent in the retraction phase, no net power is obtained. We can mention the work of Fechner and Schmehl (2013), who proposed a reel-in maneuver where the kite flies towards zenith while the azimuth angle is kept at zero. A numerical, iterative procedure based on a simplified model of the kite dynamics was used to compute the reel-in speed and elevation, at each time step, in order to maximize the cycle power. This strategy was chosen because the elevation angle typically increases during the maneuver execution, hence rendering the use of a quasi-steady model inappropriate. The optimization framework could be further explored though, as only the kite trajectory was shown as a result. Furthermore, the assumptions of constant aerodynamic coefficients and constant ratio between reel-in speed and traction force could be relaxed, allowing for a more thorough analysis. These are some of the points to be addressed in this section. On a different approach, Zgraggen, Fagiano and Morari (2015) designed a retraction maneuver to maintain the wing flying parallel to the ground, i.e. with a constant elevation angle, while the tether was reeled in. However, no criterion for the choice of the reel-in speed nor its impact on the cycle power was presented.

In the sequel we will discuss the contributions of this dissertation on the topic of cycle power maximization. We should keep in mind that we are here considering a decentralized control scheme, with distinct control laws (i.e. computed separately) for the flight and ground winch subsystems of the pumping kite. For the numerical results – that will be presented right next to the theoretical formulations – we will consider a system parameterization given by Table 6, the wind shear model depicted in Fig. 39, and the aerodynamic curves of a LEI tube kite shown in Fig. 33.

3.2.2 Traction power

We start our effort to maximize the cycle power by maximizing the traction power[8], approximated in Eq. (2.51) by the function $P(f, \theta, \phi, r, \alpha)$. To this end, the optimal (instantaneous) reel-out factor is well known to be $f^* = (1/3) \sin \theta \cos \phi$, as demonstrated e.g. by Schmehl, Noom and van der

---

[8]As we will discuss in Sect. 3.2.4, maximizing the power in the traction phase does not necessarily mean maximizing the cycle power.

Table 6 – Nominal parameters (constants) of the pumping kite model.

Description	Symbol	Value	Unit
Air density	ρ	1.2	kg/m^3
Gravitational acceleration	g	9.82	m/s^2
Wing mass	m	7	kg
Projected wing area	A	12	m^2
Projected wingspan	w_{s}	7.75	m
Electric machine inertia	J_{e}	0.25	kg $\cdot$ m^2
Drum inertia	J_{d}	0.1	kg $\cdot$ m^2
Drum radius	r_{d}	0.2	m
Ground winch transmission ratio	κ	9	-
Number of main tether(s)	n_{t}	1	-
Tether density	ρ_{t}	970	kg/m^3
Tether drag coefficient	$C_{\text{D,t}}$	1.2	-
Main tether diameter	d_{t}	5	mm
Wind model reference height	z_{ref}	15	m
Wind model reference speed	$v_{\text{w,ref}}$	7	m/s
Wind model roughness coefficient	z_0	0.05	m

Source: original
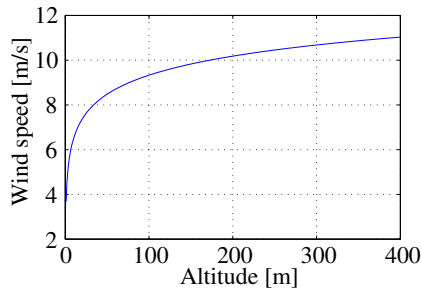
Figure 39 – Logarithmic wind shear model.

Source: original

Vlugt (2013). Keep in mind that the arguments θ, ϕ and α typically suffer cyclic variations inside a lying-eight orbit. Therefore we will attempt to optimize their average values within a single orbit, as well as the average tether length, since r constantly increases during the traction phase. By inspection in Eq. (2.51) we conclude that the optimal azimuth is $\phi^* = 0$.

Regarding the remaining three arguments observe that, by decreasing

θ the kite is able to reach a higher altitude $z = r\cos\theta$, where the wind is stronger. However, this positive effect on P is counterbalanced by displacing the system from the ideal crosswind condition, represented by the $(\sin\theta)$ factor in Eq. (2.51). There is also a trade-off with the tether length optimization: by increasing r the kite gains altitude where, again, the wind is stronger, nevertheless the total airborne drag increases due to the longer tether(s), according to Eq. (2.36). In fact, we will here predetermine the tether length variation $\Delta r = r_{max} - r_{min}$ and have it centered around the optimized value of r, i.e. the initial tether length of the traction phase will be $r_{min} = r^* - (\Delta r)/2$. Regarding the angle of attack note that, if we neglect the tether drag, the optimal value would be the one that maximizes the C term in Eq. (2.49), as discussed by Paulig, Bungart and Specht (2013). However, because we are taking the tether drag into account, there may be another value of α that, combined with a certain value of r, further maximizes P, even though C is not maximum. With this in mind we come to realize that the traction power depends on nonlinear combinations (multiplications) between θ, r and α and, therefore, these three arguments must be optimized jointly.

Before we formulate the optimization problem, observe that we intend to use Bernoulli's lemniscate as the lying-eight trajectory reference. Hence, ideally we should also treat the lemniscate focus a_l as an optimization argument. Basically, if a_l is too small the harvested power would be small due to the large steering needed to execute the tight curves and, consequently, due to the loss of the lift force decomposition onto the tether direction. On the other hand, if a_l is too big the kite would deviate too much from the high-power zone (at $\phi^* = 0$), hence P is also small. This leads us to conclude that there should be an intermediate value of a_l which is optimal. This behavior is currently under investigation and results should be published in the near future. For the numerical results in the sequel, we will consider an ad-hoc value for the lemniscate focus.

Aiming at a safe operation, we should also limit the traction force to a maximum value T_{max}, imposed by the tether minimum breaking load. The polar angle should also be constrained to a maximum in order to ensure the kite does not fly too close to the ground. We establish a minimum altitude $z_{min} = 3.5\,w_s$, i.e. the kite wingtip should keep a least distance of 3 wingspans from the ground[9]. Based on what has been presented so far and considering the point-mass wing model in dynamic equilibrium of Sect. 2.3 – which we will here refer to as the *optimization model* –, the solution is numerically obtained as

---

[9]considering no outer-loop tracking error on the lemniscate trajectory.

$$v_o^* = (\theta^*, r^*, \alpha^*) = \arg\max \left\{ C(\alpha, r) \left[v_w(\theta, r) \sin \theta \right]^3 \right\}$$

$$\text{subject to}$$

$$T \leq T_{max}$$

$$\theta \leq \arccos \left(\frac{z_{min}}{r - (\Delta r)/2} - \frac{a_l}{2} \right). \tag{3.21}$$

Having computed the optimal solution, we need to find the corresponding base angle of attack α_0^* that yields the desired angle of attack α^*. To this end let us consider once more the flight in dynamic equilibrium of Fig. 26. The partial angle of attack $\Delta\alpha$ can be computed as the solution of the force equilibrium equation in the tangent plane, while α_0 follows by using the definition of α:

$$\Delta\alpha = \arg \left\{ C_L(\alpha) \sin \Delta\alpha - C_D(\alpha, r) \cos \Delta\alpha = 0 \right\},$$

$$\alpha_0 = \alpha - \Delta\alpha. \tag{3.22}$$

With the chosen system parameters, the constraints of minimum altitude $z_{min} = 27\,\text{m}$, and maximum tether traction force $T_{max} = 15\,\text{kN}$, and setting the tether length variation as $\Delta r = 200\,\text{m}$, the optimal solution obtained is $v_o^* = (70.6°, 456\,\text{m}, 20.9°)$, yielding a mechanical power $P = 14.5\,\text{kW}$ at a traction force $T = 7.2\,\text{kN}$, achieved with a base angle of attack $\alpha_0 = 6.4°$ and at a reel-out speed $v_t = 3.1\,\text{m/s}$.

Note how $\alpha^* = 20.9°$ differs from the angle of attack of maximum kite aerodynamic efficiency $\alpha_E = 16°$, and of maximum lift $\alpha_L = 29°$ (see the curves for the LEI tube kite in Fig. 33), as expected. The optimal angle of attack is, in fact, very close to the value that maximizes the C term without considering the tether drag, $\alpha = 19.4°$, the theoretical optimum discussed by Paulig, Bungart and Specht (2013). To investigate how α^* varies with the tether drag, we ran the optimization of Eq. (3.21) for three different values of the tether drag coefficient $C_{D,t}$. For each value we changed α around the optimal value. We also applied the setpoints to the two-tether point-mass model of Sect. 2.2, which we will now denote as the *validation model*. The results are presented in Fig. 40.

Observe in Fig. 40 (top) that, by varying $C_{D,t}$ from 0 to 10 times the nominal value, the optimal angle of attack (indicated by the small circle on the peak of each power curve) only slightly varies inside the interval $\alpha^* \in [19.4°, 23.4°]$. This leads us to conclude that, although the tether drag has a strong impact on the harvested power (peak value of the P curves), it does not significantly influence the optimal angle of attack. Therefore it is indeed a

Figure 40 – Traction phase results with the massless wing model in dynamic equilibrium, used for optimization (opt mod), and the two-tether point-mass wing model, used for validation (val mod), for different values of tether drag coefficient $C_{D,t}$.
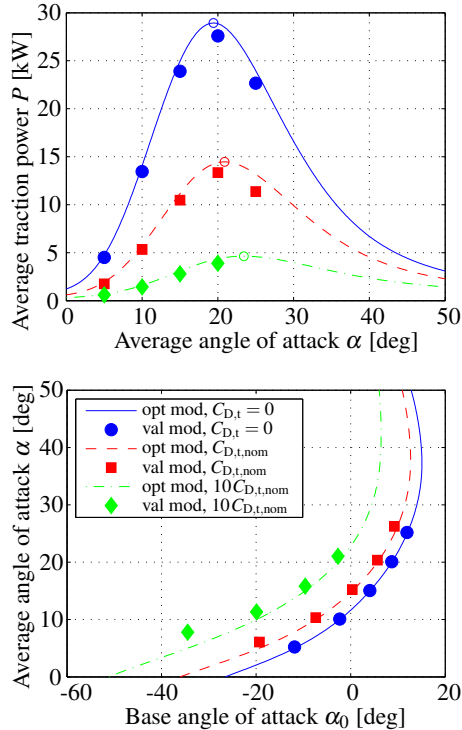
Source: original

good approximation to compute $\alpha^* = \arg\max\{C(\alpha)\}$, as proposed by Paulig, Bungart and Specht (2013), instead of having to use Eq. (3.21).

We can also see that the results obtained with the validation model (filled circles) have a high correlation with the optimization results (continuous curves). This is also the case in Fig. 40 (bottom), where the angle of attack obtained as a function of the base angle of attack is shown. For the optimization model we used Eq. (3.22), whereas for the validation model we took the average value of α. The validation experiments were carried out starting at $\alpha = 5°$, in increments of $5°$. Note that from $\alpha = 30°$ onwards no more validation results are shown. The reason is that, after the lift peak at

$\alpha_L = 29°$, the kite eventually comes to a stall and a complete traction phase is no more possible. We can here draw two conclusions. First, that the dynamic equilibrium model of Sect. 2.3 produces results which are very close to those obtained with a more complex model (of Sect. 2.2), hence the simpler model is a good choice between computational speed and modeling accuracy (the optimization takes about 3 s). The second conclusion is that we should avoid operating too close to the angle of attack of maximum lift to keep away from a stall condition.

Back to Fig. 40 (bottom), observe that the angle of attack becomes more sensitive on the base angle of attack as the latter is increased. Moreover, for high enough values of α_0 there are two equilibria of α, one of them beyond 35°. This is something to keep in mind, especially under turbulent wind conditions: a wind gust may perturb the angle of attack in such a way that it is attracted to the high-value equilibrium, causing the kite to stall. A more detailed study on the α-equilibria is yet to be carried out before we can draw further conclusions in this regard.

As a final remark on the traction power maximization, we would like to emphasize the importance of choosing the proper base angle of attack in face of the results presented in Fig 40. For instance, if we apply this optimization approach to the 500 m^2 kite considered in the paper of Lellis, Saraiva and Trofino (2013) we obtain the solution $v_o^* = (74°, 408\,\text{m}, 4.2°)$, with a corresponding $\alpha_0 = 1.1°$. Operation at this point results in 4.3 MW of electric power, i.e. a roughly 20 % increase with respect to the solution $v_o = (79.8°, 652\,\text{m}, 7.8°)$ presented in that work, where it was used $\alpha_0 = 3.5°$, the same value used by Fagiano (2009).

3.2.3 Retraction phase

Our goal here is to take a more realistic look into the retraction phase, obtaining results which could be actually tested with current prototype technology. Therefore we assumed a smooth transition from traction to retraction phase by ramping down – instead of abruptly changing – the base angle of attack and traction force to constant setpoints, which will be optimally determined in the sequel. Intuition on how to design a more efficient reel-in maneuver led us to establish the flight trajectory at $\phi = 0$, and use the traction force as the controlled variable for the electric machine at the ground, as explained in Sect. 2.2.3. For a realistic maneuver we should also take into account system constraints. Firstly, the kite, especially if made of flexible material as a LEI tube kite – or even more critically for a ram-air kite –, should not fly at too low angles of attack. Otherwise the wing loading can be

very low, the kite may lose its proper inflated shape, and thus lose steering capability. Hence let us consider a lower limit α_{min} on the angle of attack. Secondly, there is in practice a speed limitation $v_{t,sat}$ of the electric machine, imposed by factors such as the maximum centrifugal force withstood by the windings, the number of poles, and the transmission ratio κ between drum and electric machine.

Differently from Sect. 3.2.2, our goal now is to maximize the cycle power. Considering that $P_o(t)$ and $P_i(t)$ are the instantaneous mechanical power in the traction and retraction phases, respectively, the cycle power is

$$P_{cyc} = \frac{\int P_o(t)dt + \int P_i(t)dt}{\Delta t_o + \Delta t_i}. \qquad (3.23)$$

Having optimized the traction phase a priori, we know $\int P_o(t)dt$ and Δt_o. Therefore we can promptly set the following initial conditions of the retraction phase: $\dot{r}_i(0) = v_{t,o}^* = f^* v_w$, $r_i(0) = r_o^* + (\Delta r)/2$ and $\theta_i(0) = \theta_o^*$. If we consider the kite flying towards zenith, i.e. $\gamma = \pm\pi$, the tangential velocity is solely in the θ direction: $v_{k,\tau} = r\dot{\theta}$. By replacing this into Eq. (2.52) the initial angular condition $\dot{\theta}_i(0)$ can be computed. The initial value of the traction force can be obtained by solving Eq. (2.42b) for T with $\ddot{r} = 0$ and all other variables as already discussed. Then, with the zero-azimuth model of Sect. 2.2.3, including given ramp inclinations c_α and c_T of the control input curves of Eq. (2.41), we can simulate the retraction phase and compute the instantaneous power $P_i(t) = T_i(t) v_{t,i}(t)$ and cycle power in Eq. (3.23). We are now in conditions of optimizing the constant setpoints of base angle of attack and traction force to be used during the retraction phase. To this end we execute a grid search and obtain

$$v_i^* = (\alpha_{0,i}^*, T_i^*) = \arg\max \left\{ P_{cyc}\left(\alpha_{0,i}, T_i, \int P_o(t)dt, \Delta t_o\right) \right\}$$
$$\text{subject to} \qquad (3.24)$$
$$\alpha \geq \alpha_{min}$$
$$v_t \geq -v_{t,sat}.$$

It is intuitive to think we would like to de-power the kite as fast as possible, but there is also a speed limitation to execute that. Let us assume we are using the (maximum) de-powering speed $c_\alpha = -10°/s$. For ramping down the traction force, we will consider a ramp inclination $c_T = 982\,N/s$. Moreover, let us assume the optimization constraints are $\alpha_{min} = -5°$ and $v_{t,sat} = 10\,m/s$. To have a more comprehensive look into the optimization, we define a broad grid interval, composed by $\alpha_{0,i} \in [-100,0]°$ and $T_i \in [0,1000]\,N$, with reso-

lution $\delta\alpha_{0,i} = 5°$ and $\delta T_i = 50\,\mathrm{N}$. Using a time-integration step $\delta t = 50\,\mathrm{ms}$ to simulate the retraction phase, the resulting cycle power surface is shown in Fig. 41.

Figure 41 – Cycle power as a function of the constant references of traction force and base angle of attack, used after the ramping down in the retraction phase.
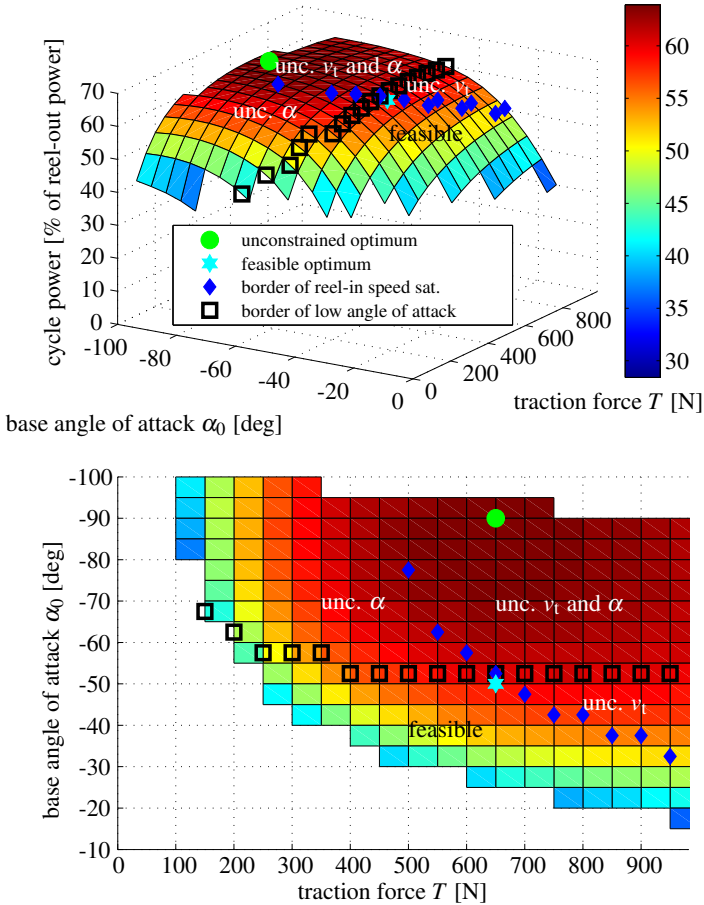
Source: original

Observe that, for intermediate values of T_i and $\alpha_{0,i}$, the retraction phase is completed without violating the constraints on the angle of attack and reel-in speed. In this case we say the solution $v_i = (\alpha_{0,i}, T_i)$ is inside the

feasible region. Let us take a grid point for our analysis somewhere in the middle of this region. Starting there, if T_i is increased there may be initially an increase in P_{cyc} because the tether must be reeled-in faster. However, at a certain point, reel-in saturation may happen. If not, we may reach a certain value of T_i beyond which the benefit of operating at a faster reel-in speed – thus with a shorter retraction phase – is overshadowed by the increase in the power expense to reel-in the tether, hence P_{cyc} starts to decrease. Back to the starting point of our analysis and moving towards lower values of T_i, the tendency is for the cycle power to decrease because the retraction phase must be carried out at a reel-in speed closer to zero, hence Δt_i increases in Eq. (3.23). If T_i becomes too low, the retraction maneuver is not possible anymore because the tether must be actually reeled-out to allow for the low traction force.

Once again in the middle of the feasible region and then decreasing $\alpha_{0,i}$, the cycle power increases monotonically, regardless of T_i. The problem is that, below a certain value of base angle of attack, the constraint on the minimum angle of attack is violated at some point during the maneuver. Looking into the other direction, when increasing $\alpha_{0,i}$ it comes a point when the retraction phase cannot be completed anymore for the same reason as for a traction force too low: the tether must be reeled out. Grid points for which the retraction phase cannot be completed were omitted (blank/white squares) in Fig. 41.

Observe that the maximum cycle power $P_{cyc,unc}^* = 0.639\,P_o$ is obtained with $v_{i,unc}^* = (-90°, 650\,\text{N})$, in a region where both constraints $v_{t,sat}$ and α_{min} are violated. We refer to $v_{i,unc}^*$ as the *unconstrained optimum*. To comply with the constraints we must look for the optimal solution inside the feasible region. Thus our choice becomes $v_i^* = (-50°, 650\,\text{N})$, the *feasible optimum*, which yields $P_{cyc}^* = 0.556\,P_o$. As can be seen in Fig. 41, one could think of the optimal solution more as a "plateau region", since the cycle power remains approximately constant in the vicinity of $v_{i,unc}^*$. In fact note that, relative to the unconstrained optimum, the decrease in cycle power to reach the feasible optimum is below 10%.

If this optimization were applied to a rigid wing, the constraint on the minimum angle of attack could probably be disregarded. However, when considering a foil (ram-air) kite, the α_{min} constraint could be more restrictive. In this case the border of α_{min} violation – indicated by the black squares in Fig. 41 – would move towards higher values of α_0, "squeezing" the feasible region. This would also be the case if we had a ground station with less reel speed capability: the feasible region would be squeezed to the left by the $v_{t,sat}$ line (blue diamonds in Fig. 41). Also note that, not only power kites have a limited de-powering speed c_α, but also the maximum de-powering itself may

be limited, i.e. α_0 may not be arbitrarily low, especially for flexible kites. This constraint can be easily taken into account by reducing the $\alpha_{0,i}$ search domain. Similarly, a minimum value of traction force T_{min}, which is important to ensure the kite maintains steering capability during the reel-in maneuver, can be taken into account by reducing the search domain to $T_i \geq T_{min}$.

Figure 42 – Examples of retraction phase trajectories in the $\phi = 0$ plane: (i) feasible optimum, (ii) unconstrained optimum, (iii) violation of α_{min}, and (iv) violation of $v_{t,sat}$.

Source: original

In Fig. 42 we can compare flight trajectories obtained with different values of v_i. Note that, in the first 4 s, when α_0 and T are being ramped down in all cases, the trajectories are the same because of the same c_α and c_T. Furthermore, we can see that the unconstrained optimum, which requires $\alpha_{0,i} = -90°$, causes the kite to follow more of a straight trajectory towards the ground station – a behavior we already expected since it makes the kite operate at a very low angle of attack. To verify this, and understand how these trajectories are generated, let us take a look at some system variables, presented in Fig. 43.

Note how the unconstrained optimum causes both the $v_{t,sat}$ and α_{min} constraints to be violated. In fact, the angle of attack becomes extremely low, closing in on $\alpha = -20°$, below which the aerodynamic curves of the LEI tube kite are not defined (see Fig. 33). We can also see that the maneuver with $(-70°, 300\,N)$ is the longer one, which is mostly due to the relatively low traction force, requiring very little power to be spent, but also violating α_{min} because of the high de-powering.

Figure 43 – Time evolution of system variables of four different retraction phase solutions: (i) feasible optimum, (ii) unconstrained optimum, (iii) violation of $\alpha_{\min}$, and (iv) violation of $v_{t,sat}$.
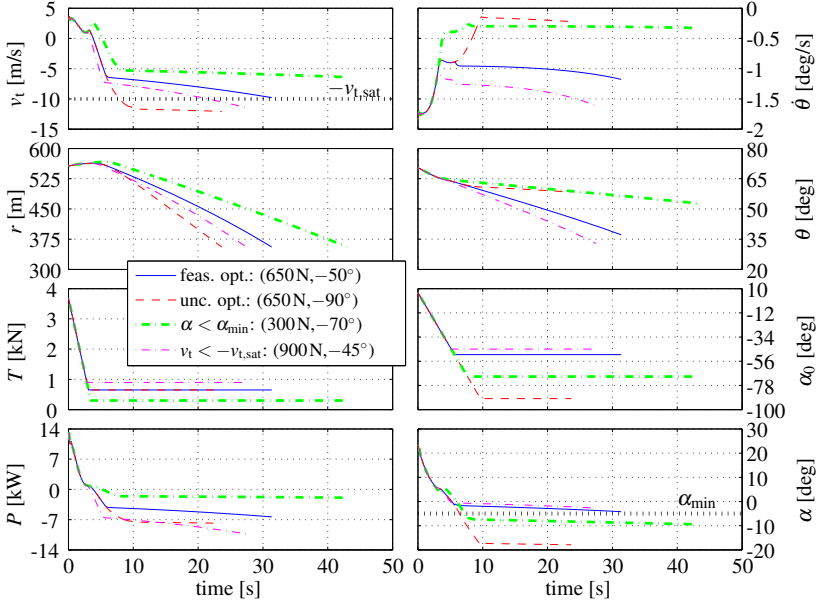
Source: original

3.2.4 Iterative algorithm

As stated in the beginning of this section, our end goal is to find a pumping cycle parameterization that maximizes the cycle power. This was already considered in the retraction phase optimization of Sect. 3.2.3. However, in Sect. 3.2.2 the maximized function was the traction power P, whose maximum does not correspond to the maximum of the cycle power P_{cyc}. The reason is simple: imagine we decrease the traction phase reel-out speed $v_{t,o}$. It can be shown that the traction power, approximated by Eq. (2.51), will decrease, yet the duty cycle $\Delta t_o / (\Delta t_o + \Delta t_i)$ will increase – i.e. the kite will spend a greater ratio of the pumping cycle duration harvesting energy. While the decrease of P has a negative effect on P_{cyc} (see Eq. (3.23)), the increase in the duty cycle has a positive effect on P_{cyc}. We will see in the sequel that, if $v_{t,o}$ is decreased to a certain amount, we can further maximize the cycle power.

The idea is, once the traction power and retraction phase are optimized in a first iteration, to run a second iteration where the traction phase is optimized to maximize the cycle power, this time considering the reel-out speed as an argument. Because we have discussed it is a good approximation to optimize the angle of attack by maximizing $C(\alpha)$ in Eq. (2.49) regardless of the tether drag, we will keep the value of α^* found in the first iteration. Also, since the retraction phase initial conditions depend on the optimal solution of the traction phase, we must complete the iteration with a new optimization of the retraction phase as well. We will execute these iterations until the increase in P_{cyc} falls below a tolerance, meaning we reached a new optimum. This is represented in pseudo code by Algorithm 4.

Algorithm 4: Iterative algorithm for pumping cycle optimization (constraints have been omitted for a compact representation).

> **while** *increase in $P_{cyc} \geq$ tolerance* **do**
> > **if** *1st iteration* **then**
> > > $(\theta_o^*, r_o^*, \alpha_o^*) = \arg\max\left\{ C(\alpha, r) \left[v_w(\theta, r) \sin\theta \right]^3 \right\}$;
> > > $v_{t,o}(t) = (1/3) \sin\theta(t) \cos\phi(t) v_w(t)$;
> >
> > **else**
> > > $(\theta_o^*, r_o^*, v_{t,o}^*) = \arg\max\left\{ P_{cyc}\left(\theta, r, v_t, \int P_i(t) dt, \Delta t_i \right) \right\}$;
> > > $v_{t,o}(t) = v_{t,o}^* \cos\phi(t)$;
> >
> > **end**
> > $\alpha_{0,o}^* = \alpha_o^* - \Delta\alpha(\alpha_o^*, r_o^*)$;
> > $(\alpha_{0,i}^*, T_i^*) = \arg\max\left\{ P_{cyc}(\alpha_{0,i}, T_i, \int P_o(t) dt, \Delta t_o) \right\}$;
>
> **end**

Let us consider the de-powering limit of the kite is $\alpha_0 = -60°$, set the convergence tolerance to $100\,\text{W}$, and shorten the retraction phase optimization grid to intervals in which the optimal values are more likely to be found. For the 1st iteration, we search inside $\alpha_{0,i} \in [-60, -20]°$ ($\delta\alpha_{0,i} = 2.5°$) and $T_i \in [200, 900]\,\text{N}$ ($\delta T_i = 100\,\text{N}$). For the following iterations we still consider these intervals, but center the grid around the solution previously found 5 times the resolution in each direction. The resolution is then set to $\delta\alpha_{0,i} = 2°$ and $\delta T_i = 25\,\text{N}$. The values of all other involved parameters remain as presented so far. With these settings, the solution found is $v^* = (\theta_o^*, r_o^*, v_{t,o}^*, \alpha_{0,o}^*, \alpha_{0,i}^*, T_i^*) = (70.4°, 400\,\text{m}, 2.3\,\text{m/s}, 6.8°, -50°, 600\,\text{N})$, yielding an optimal cycle power $P_{cyc}^* = 9.2\,\text{kW} = 0.672\,P_o$. The algorithm took 1 minute and 55 seconds to converge in 3 iterations, with more than 90 % of the duration required for simulating the retraction phases. Note that, because the optimal reel-out speed found was 25.8 % lower than the value that maximizes

the traction power (1st iteration), we obtained a 9.3 % increase in the optimal value of cycle power, accompanied by a 27.8 % increase in the traction force. The optimized kite trajectory is shown in Fig. 44.

Figure 44 – Optimized flight trajectory during two pumping cycles. The 1st cycle begins in the middle of the traction phase.
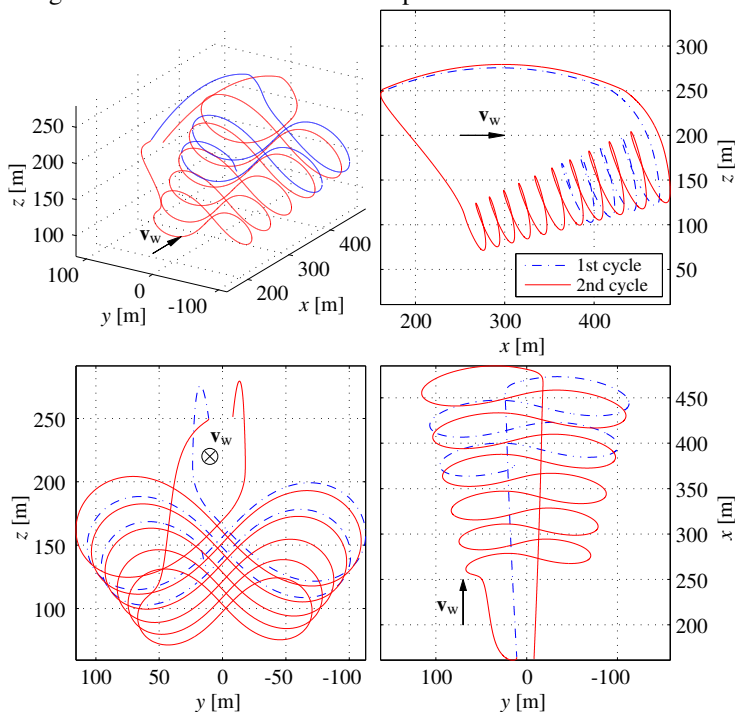
Source: original

The time course of some system variables are shown in Fig. 45. Note how the design and validation results of the retraction phase, with the 2D and 3D models of Sects. 2.2.3 and 2.2, respectively, closely match. In the traction phase we can see the cyclic variations in the traction force, power, polar angle, angle of attack, and in the steering input Δl. The discontinuity in Δl is due to the transition from the reel-in trajectory with $\phi = 0$ back to the lemniscate, when a new pumping cycle begins.

To show how the optimal pumping cycle solution behaves when system parameters are varied we ran a sensitivity analysis with respect to the nominal solution previously obtained. Because the traction force is influ-

Figure 45 – Time evolution of system variables in a pumping cycle.
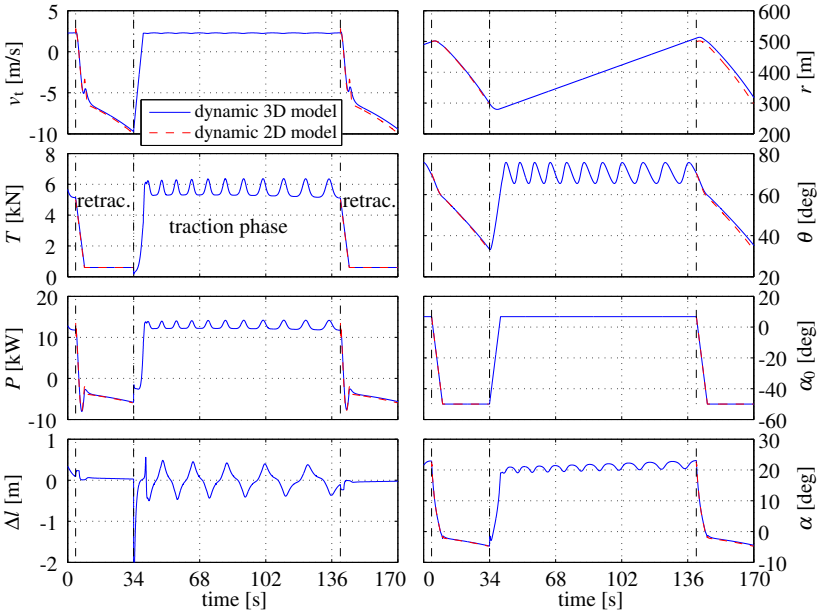
Source: original

enced by the kite glide ratio E_k through the C coefficient, whereas T depends linearly on the kite area A (see Eq. (2.50)), we adjusted the ramp inclination from the nominal value as $c_T = c_{T,nom}(C/C_{nom})$ when varying E_k, and $c_T = c_{T,nom}(A/A_{nom})$ when altering A. The results are shown in Fig. 46. Variations of the kite mass were not considered because the model used for the traction power optimization is massless. Also keep in mind that the tether diameter remained unaltered, although in reality it should vary according to the traction force variations.

Observe the strong influence of the kite glide ratio on the cycle power: a variation of 30 % on E_k almost doubled P_{cyc}, only possible because the base angle of attack increased by 50 %, to $\alpha_{0,i} = -27.5°$. Less de-powering results in a higher traction force during the reeling-in, which is indeed observed. Although not shown in Fig. 46, the higher glide ratio causes the kite tangential speed to increase, and therefore the reel-in maneuver must end around zenith. This situation may require a more elaborate strategy to maintain the traction force above a minimum safety level when making the transition back to the traction phase. In any case, the high sensitivity of P_{cyc} on E_k justifies the efforts in developing more aerodynamically efficient materials for power kites,

Figure 46 – Sensitivity analysis by varying the kite glide ratio, $E_k = C_L/C_{D,k}$, and projected wing area, A, around their nominal values.
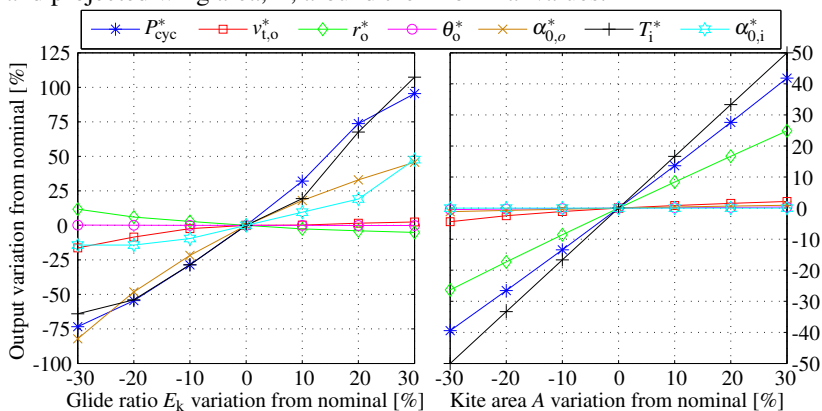
Source: original

especially for flexible (ram-air and LEI tube) ones. In the right-hand side plot we can see that the base angle of attack is not affected by variations of the kite area, as one could have expected. On the other hand, the inclination of the P_{cyc} curve is higher than one, which does not correspond to the expected linear behavior modeled by Eqns. (2.50) and (2.51). This is partially because the tether diameter was kept constant in spite of the changing traction force, but especially due to variations of the average tether length r_o^*, and the corresponding changes on the operating altitude and nominal wind, according to Eq. (2.66).

It is important to highlight that, when scaling up to higher power levels an AWE system based on a tethered wing, the necessary increase in the tether diameter required to match the higher traction force levels contributes to decreasing the equivalent drag coefficient of the airborne system, independently of the airfoil efficiency. To better understand this effect, let us recall Eq. (2.36). In the right-hand side of that expression we have two shares of the total drag: the airfoil drag, and the tether drag – the latter depending on the tether diameter d_t. Therefore, even if the airfoil drag coefficient $C_{D,k}$ and the tether drag "specific" coefficient $C_{D,t}$ remain the same when scaling up the system, the "total" tether drag coefficient, i.e. the second share in Eq. (2.36), grows linearly with d_t, just as it does with the tether length r. This observation suggests that the increase in P_{cyc} when increasing either the wing glide ratio E_k or the projected wing area A in the sensitivity analysis of Fig. 46 should be, in reality, lower. A more detailed study in this regard is yet to

be carried out.

As final remarks to this section, we can mention a few other points for investigation in future works. Firstly, the lemniscate focus a_l is a parameter that is still to be optimized. Also, the ramp inclinations of the base angle of attack c_α and traction force c_T were set empirically. Therefore an interesting question is what would be the best values of c_α and c_T to be considered or, more generally, how to optimize these parameters. This is particularly important because the combination of tether length with the wing tangent speed (e.g. about 100 km/h regardless of the system size) determines a required time to leave the crosswind condition, i.e. to reach a certain elevation angle. Hence, if the parameters c_T and c_α are not properly chosen, the transition into the reel-in phase may be too fast or too slow.

Alternatively, it would be interesting to relax the requirement of constant setpoints and linear ramping down of the base angle of attack and traction force, and use more powerful optimization tools, such as NMPC, to find trajectories of these parameters that yield a higher cycle power. In this work we have used a simple grid search method for the optimization because we would like to have an idea on how sensitive the optimal solution is with respect to changes in some parameters as, for instance, the base angle of attack and traction force setpoints of the retraction phase.

Another improvement would be to model and include in the optimization the transition from the retraction back to the traction phase in order to guarantee a safe maneuver. Also, for the cases when e.g. the wing aerodynamic curves and the wind model are not well known, an alternative modeling and optimization procedure based on more easily estimated (available) parameters could be developed. Finally, regarding the aerodynamics and structural dynamics of flexible kites, it would be valuable to know where the constraint on the minimum angle of attack is, since we showed how a relaxation of this constraint yields a higher cycle power.

3.3 POWER CURVE

The power curve of a wind device represents how much power is extracted from the wind as a function of the wind speed. In the case of a horizontal-axis wind turbine, because the rotor operates at a fixed height, we need to consider only the wind speed at that height. This means that the power curve would be, in principle, independent of the site where the turbine operates. However, in the case of a pumping kite, due to its degree of freedom to change the operating height according to the wind shear model of Eq. (2.66), we must vary the wind speed at the reference height, v_{ref}. As a consequence,

the wind speed will be changed accordingly at all heights. As we will see, the distinct interpolation of the wind shear model for each location may result in a distinct power curve for the same pumping kite system.

For the sake of simplicity, we will consider from now on a simpler model for the pumping cycle than the optimization method proposed in Sect. 3.2. This simplification is twofold. Firstly, as long as the traction force is below the tether capacity, the reel-out speed is the "classic" solution for the traction power maximization, given by Eq. (1.5). If the nominal wind at the wing altitude becomes large enough so that the traction force is saturated, the reel-out speed increases above the value that maximizes the traction power in order to limit the traction force. The second simplification on the pumping cycle regards the retraction phase: we will assume we can reel-in the tether while keeping the polar angle constant. This requires finding the angle of attack that stabilizes the θ motion given by Eq. (2.42a). Such reel-in maneuver could be realized, for instance, by means of the B-stall procedure for foil kites, discussed in Sect. 2.1. Here we will assume that, during the retraction phase, the B-stall causes the lift coefficient to be reduced to a fifth of the value indicated in Fig. 33, i.e. the whole curve is divided by 5. Another advantage of considering the foil kite curves instead of the LEI tube kite ones of Fig. 33 is that the foil curves were obtained through a CFD method. Therefore, based on the latter curves we should get a more realistic feel of how much mechanical power can be harvested by a real system during the traction phase.

Motivated by the idea of comparing the AWE approach to the conventional technology of wind turbines, we will consider henceforth a larger, more powerful pumping kite system. As a size reference, let us consider a wind turbine with a rotor diameter of 90 m and a nacelle placed on top of a tower 80 m high, driven by three blades with a length of 44 m ("wingspan") and an average chord length (blade "height") of 2.5 m. Turbines of this size usually have a rated (electric) power around 2 MW. We then define the wing projected area as the total area of the three blades combined. The pumping kite parameters are summarized in Table 7.

Considering the location of Schleswig (Germany), the power curve as well as the behavior of other system variables are presented in Fig. 47. It is important to mention that we are considering two constraints here. The first one is the maximum operating height, $z_{k,max} = 600$ m, which corresponds to the limit above which the logarithmic wind shear model may loose accuracy. The second constraint is the maximum tether length r_{max}, which derives from spatial constraints for a hypothetical hybrid wind farm with both tower-based wind turbines and pumping kites. For wind power plants installed in flat areas, as a general rule, the turbines are distant from one another $7R$ in the direction of the prevalent wind, and $4R$ in the perpendicular direction, where R is the

Table 7 – Parameterization of a foil pumping kite similar in size to a $2\,\mathrm{MW}$ horizontal-axis wind turbine.

Description	Symbol	Value	Unit
Air density	ρ	1.2	$\mathrm{kg/m^3}$
Gravitational acceleration	g	9.82	$\mathrm{m/s^2}$
Mass of wing and control pod	m	203	kg
Projected wing area	A	330	$\mathrm{m^2}$
Projected wingspan	w_s	39.8	m
Number of main tether(s)	n_t	1	-
Tether density	ρ_t	731.9	$\mathrm{kg/m^3}$
Tether drag coefficient	$C_\mathrm{D,t}$	1.2	-
Tether diameter	d_t	18	mm

Source: original

rotor diameter. Hence, assuming $R \approx 100\,\mathrm{m}$ and $100\,\mathrm{m}$ of minimum distance between the tethered wing and the turbine tower, we obtain $r_\mathrm{max} = 600\,\mathrm{m}$ (for $\theta = \phi = 0$). The amount of tether to be reeled-out/in during a pumping cycle is $\Delta r = 200\,\mathrm{m}$. We can divide the power curve in five regions:

I right below the *cut-in* value, the wind speed is simply too low for operation. Although the mathematical model suggests a very small yet positive cycle power, unmodeled mechanisms, such as the possible dependence on a minimally strong wind to allow for launching and landing the kite, as well as the negative effect of the airborne weight (wing, control pod and tether), render the operation unfeasible;

II right after the *cut-in* value, the wind speed becomes strong enough for the system operation. The mean, optimal values of tether length r^*, polar angle θ^*, and angle of attack α^* result from the traction power optimization given by Eq. (3.21). Within this region the traction power grows with the cube of the wind speed, according to Eq. (2.51). It is interesting to observe that, although the power in the traction and retraction phases are (in magnitude) approximately the same, the cycle power is almost as high as the traction power. This is due to the relatively very high duration of the traction phase w.r.t. the retraction phase, i.e. a large *duty cycle*[10]. Also, observe how the reel-out speed curve has a lower inclination than the nominal wind curve (one third, in fact). The traction force grows according to a parabola given by Eq.

---

[10]The importance of the duty cycle was considered in the pumping cycle optimization proposed in Sect. 3.2. In this simplified method, the duty cycle is not an optimized variable.

Figure 47 – Power curve of a pumping kite with a $330\,\text{m}^2$ foil wing and ad-hoc retraction phase with constant polar angle, for the location of Schleswig, Germany. The reference height of the wind model is $z_{\text{ref}} = 30\,\text{m}$.
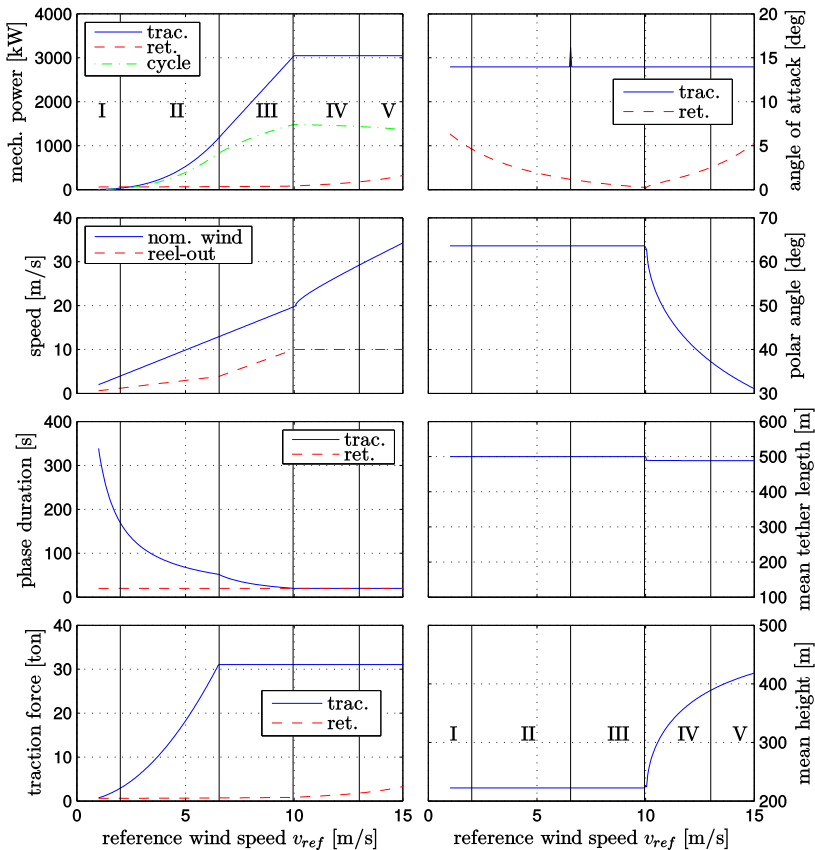
(2.50). Note how the polar angle is high, around $63°$, placing the wing in approximate crosswind conditions. Combined with the mean tether length saturated at $r^* = r_{\text{max}} - 0.5\,\Delta r$, the operating altitude is around $220\,\text{m}$, which is above the blade tips of our hypothetical $2\,\text{MW}$ wind turbine. It is also interesting to observe that the angle of attack of the retraction phase, in this region, decreases as the reference wind speed v_{ref} increases. This is because, as the apparent wind becomes faster, a lower lift coefficient is needed to counterbalance the airborne mass in

order to keep the polar angle constant.

III the beginning of this region is characterized by the saturation of the traction force. In this case, considering the Dyneema® curve of minimum breaking load of Fig. 32 and the tether diameter $d_t = 18\,\text{mm}$, the saturation value is $T_{\text{sat}} = 31.05\,\text{ton}$. As v_{ref} continues to increase, the reel-out speed must become higher than the optimal value given by Eq. (1.5) in order to ensure that the traction force saturation is respected. This means the pumping kite must harvest less power in the traction phase than it theoretically could do. In fact, note how the inclination of the reel-out speed and the nominal wind speed become the same (parallel lines). Since, in this region, the reel-out speed varies whereas the traction force is kept constant, the power $P = T\,v_t$ now varies linearly with the reel-out speed. Also, note how the traction phase duration decreases towards the retraction phase duration as the nominal wind becomes stronger, i.e. the duty cycle decreases. This has a negative impact on the cycle power, which increases progressively slower than the traction power.

IV this region begins when the reel-out speed reaches saturation, here assumed to be at $v_{t,\text{sat}} = 10\,\text{m/s}$. Since the traction force was already saturated, the mechanical power is kept constant even though the nominal wind increases with the increasing v_{ref}. This power saturation can be achieved by deviating the operating point from the optimal crosswind condition, i.e. θ diminishes. Consequently, the operating height increases, and so does the nominal wind speed (note the slight change of inclination w.r.t. region III). Another consequence of the decrease in the mean polar angle is that the increasing drag force – due to the stronger wind – tends to push the wing back to a high θ. Thus, the θ equilibrium at low values can only be achieved by a stronger lift force, and therefore the angle of attack must increase. This, in turn, causes the traction force during the reel-in phase, and consequently the power expense, to increase. Finally, the augmented power expense causes the cycle power to monotonically diminish as v_{ref} becomes faster.

V if the nominal wind becomes too strong, above the *cut-off* value that defines the beginning of this region, the pumping kite must be put out of operation (landed). One reason for this is that the cycle power progressively decreases in spite of the increasing wind – a loss of efficiency that was already happening in region IV. Secondly, the very fast nominal wind (approaching hurricane speeds around $100\,\text{km/h}$) usually comes along with high turbulence and stormy conditions, not to mention other threats as lightning, thus resulting in a hazardous operating

scenario. It is postulated, though, that the extra degree of freedom of the pumping kite to move away from the crosswind (by decreasing θ) allows the pumping kite to operate in stronger wind speeds than the tower-based wind turbine, i.e. to have a higher cut-off wind speed.

One can also observe in Fig. 47 that r^* remains approximately constant even though the mean tether length is optimized for each distinct value of the reference wind speed v_{ref}. This occurs in this particular case because, given the maximum tether length constraint $r_{max} = 600\,\mathrm{m}$, changing the polar angle has a much more significant effect on keeping the traction power constant (in regions IV and V) than changing r.

As claimed in the beginning of this section, differently from a conventional wind turbine, the power curve of a pumping kite depends on the location where it operates because of the distinct wind shear model interpolations. To illustrate this, we computed the power curve of the same pumping kite, with parameters given in Table 7 and Fig. 33, for the locations of Confins, Fortaleza and Schleswig, considering their wind shear model parameters in Table 3. Note that the wind model for these sites was interpolated with the same reference height z_{ref}. This is required for the analysis that will follow. The resulting curves of (mechanical) cycle power, average polar angle, average operating height, and nominal wind at the operating height are shown in Fig. 48. The average tether length was roughly $500\,\mathrm{m}$ for all locations throughout the whole span of v_{ref}.

Taking into consideration the wind shear curves of Fig. 27, one could readily accept the higher cycle power (up to reaching its peak) in Schleswig. What can seem a contradiction at first sight is the fact that the cycle power curve in Confins increases faster than in Fortaleza, although Fortaleza has a clearly stronger wind speed at all heights. The explanation lies in the surface roughness coefficient z_0: it basically indicates how strong is the wind gain with the altitude. For low values of z_0 the wind grows slowly with the altitude (more "horizontal" wind shear curves in Fig. 27), as happens e.g. at the sites of Fortaleza ($z_0 = 0.0052$), Alta Floresta ($z_0 = 0.0012$) and Brindisi ($z_0 = 0.0083$). On the other hand, sites as Belém ($z_0 = 8.5124$), Porto Alegre ($z_0 = 4.8328$), De Bilt ($z_0 = 7.4770$) and Schleswig ($z_0 = 3.8512$) present a stronger wind gain, with more "C-shaped" wind curves. Confins has an intermediate surface roughness: $z_0 = 0.3932$. Because in the comparison of the cycle power curves in Fig. 48 we are applying the same v_{ref} for all locations, regardless of how often such wind speed occur, what causes the curves to be different is the z_0 coefficient. We will see in Chap. 4 that, although Confins yields theoretically a better cycle power curve than Fortaleza, the influence of the wind histogram causes a pumping kite in Fortaleza to produce a higher amount of energy because of the higher capacity factor.

Figure 48 – Power curves of a pumping kite with a $330\,m^2$ foil wing and ad-hoc retraction phase with constant polar angle, for the locations of Confins, Fortaleza and Schleswig.
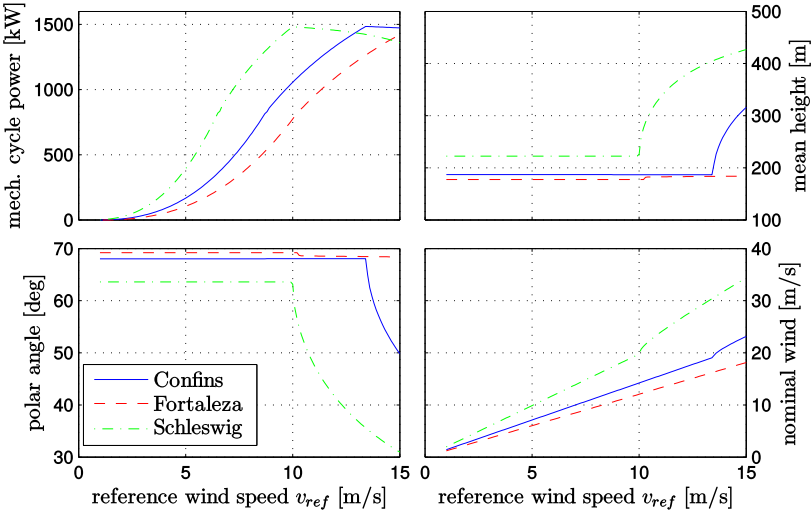
Source: original

Furthermore, observe in Fig. 48 that the pumping kite in Schleswig operates at a lower polar angle, which implies a higher altitude. In such case, the option to deviate more from the crosswind operation in order to have a stronger nominal wind is advantageous, given the larger z_0 coefficient of Schleswig. For the cases of Confins and Fortaleza, however, the best option found by the optimizer was to prioritize the crosswind condition.

As a final comment on the power curve note that, although the pumping kite has been parameterized to approximately match a 2 MW wind turbine, it has reached a peak traction power of about 3 MW. As we will discuss for the case of wind turbines in Sect. 4.3.1, to obtain the electric power we should take into account several losses, including aerodynamic (blade tip), mechanical and electrical ones. Put together, these losses may result in an efficiency factor around $\zeta \approx 0.7$, to be applied to the mechanical power curve. This would cause the maximum traction power of Fig. 47 to yield the approximated 2 MW of electric power expected. Moreover, to compute the electric cycle power through Eq. (3.23), besides multiplying the traction power by ζ, one must divide the retraction power by the same efficiency factor. This leads us to conclude that the conversion efficiency of the pumping kite has a

stronger impact on the net power delivered – due to the retraction phase – than in the case of a wind turbine or even Loyd's drag mode, which are constantly generating energy.

4 MODELING FUNDAMENTALS OF WIND ENERGY

We have two goals in this chapter. The first one is to compare horizontal-axis wind turbines with pumping kites in terms of power production. Having studied the power curve of a pumping kite based on the model of Sect. 2.3, we now need a model for the turbine. Our second goal is to verify that both Loyd's lift and drag mode machines can be seen as a specific case of the generic actuator disc – considered when deriving the Betz limit for power extraction from the wind through conservation of energy.

4.1 BETZ THEORY AND THE ACTUATOR DISC MODEL

The modeling framework discussed in the sequel is reproduced from Manwell, McGowan and Rogers (2009). Let us consider an actuator disc subject to an airflow within a control volume. This actuator disc is a generic device upon which the airflow can execute work and, therefore, transfer energy. Keep in mind that we are not specifying whether the disc corresponds to the rotor swept area of a horizontal-axis wind turbine, or the area covered by a tethered wing in a circular flight path and operating with a high polar angle (approaching $90°$). We will start by considering only the axial dimension of the disc, and use momentum theory to derive the Betz limit. To this end, let us also establish the following assumptions:

- a homogeneous and incompressible fluid flow at steady state (no accelerations);

- no frictional drag;

- an infinite number of blades (or wings);

- a uniform thrust force upon the disc area;

- a non-rotating wake;

- a static pressure far upstream and far downstream of the disc equal to the undisturbed ambient static pressure.

The idea is that the energy harvested by the actuator disc from the airflow must decrease the wind speed, in accordance with the principle of conservation of energy. In other words, if the wind has lost kinetic energy, its speed downstream of the disc must be lower than it is upstream. Hence we can

define four wind speeds along the airflow direction: the far upstream speed, U_1, the upstream speed reaching the disk, U_2, the downstream speed leaving the disc, U_3, and the far downstream speed, U_4. This scenario is depicted in Fig. 49. The disc area is $A_2 = A_3 = A$.

Figure 49 – Actuator disc of a generic wind power device immersed in a homogeneous airflow.
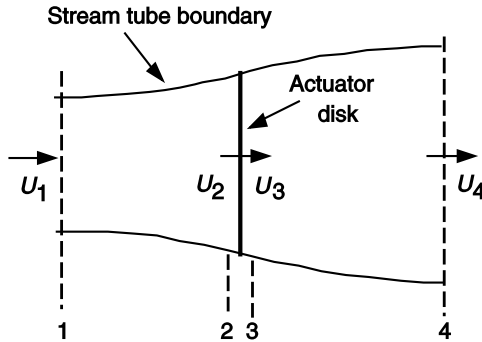
Source: Manwell, McGowan and Rogers (2009)

From the conservation of linear momentum for a one-dimensional, incompressible, time-invariant airflow interacting with the actuator disc, the thrust (force) T upon the disc is equal, in magnitude, to the rate of change of momentum of the air stream:

$$T = U_1 (\rho A U)_1 - U_4 (\rho A U)_4 , \qquad (4.1)$$

where A is the cross-sectional area, U is the wind speed, and the subscript indicates the numbered cross-section along the flow of Fig. 49. Observe that $\rho A U = \dot{m}$ is the mass flow rate, which is constant according to our assumption of a steady state flow. Hence $(\rho A U)_1 = (\rho A U)_4$, and Eq. (4.1) is simplified to

$$T = \dot{m} (U_1 - U_4) . \qquad (4.2)$$

Note that a positive thrust upon the disc requires that $U_1 > U_4$. Now let us find how the wind speeds U_2 and U_3 are related to U_1 and U_4. Since work is executed by the air stream only upon the disc, i.e. between cross-sections 2 and 3, we can apply Bernoulli's equation to the control volumes on either sides of the disc:

$$p_1 + \frac{1}{2}\rho U_1^2 = p_2 + \frac{1}{2}\rho U_2^2 \quad \text{and} \quad p_3 + \frac{1}{2}\rho U_3^2 = p_4 + \frac{1}{2}\rho U_4^2, \qquad (4.3)$$

knowing that the assumption of a homogeneous fluid implies that $\rho_1 = \rho_2 = \rho_3 = \rho_4 = \rho$. The thrust can also be expressed as the net sum of forces on each side of the actuator disc:

$$T = A\left(p_2 - p_3\right). \qquad (4.4)$$

The assumption of static pressures far upstream and far downstream equal to the undisturbed ambient static pressure means that $p_1 = p_4$ in Eq. (4.3), whereas the non-rotating wake implies that $U_2 = U_3$. With these simplifications we can solve Eq. (4.3) for $p_2 - p_3$ and replace the result into Eq. (4.4), obtaining another expression for the thrust:

$$T = \frac{1}{2}\rho A\left(U_1^2 - U_4^2\right). \qquad (4.5)$$

If we now equate the thrust expressions of Eqns. (4.2) and (4.5), recalling that the constant mass flow also means that $\dot{m} = \rho A U_2$, we get

$$U_2 = \frac{U_1 + U_4}{2}. \qquad (4.6)$$

With this we have related the wind speeds at all four cross-sections of Fig. 49. The next step is to relate the wind speeds to the power extraction at the rotor disc. To this end, let us define the *axial induction factor a*, representing the fractional decrease in wind speed between the far upstream and the upstream cross-section at the rotor disc:

$$a = \frac{U_1 - U_2}{U_1}. \qquad (4.7)$$

Another way to think of a is as a variable representing a "permeable wall" effect: if $a = 0$ then the actuator disc does not slow down the wind flow reaching it, i.e. the disc is a perfectly permeable obstacle. As the disc starts extracting kinetic energy from the airflow, U_2 decreases and a increases, meaning that the disc becomes less permeable. From Eqns. (4.7) and (4.6) we get the relations

$$U_2 = U_1(1 - a) \quad \text{and} \quad U_4 = U_1(1 - 2a). \qquad (4.8)$$

Observe that, if $a = 1/2$, the wind far downstream of the actuator disc has slowed down to zero. In fact, for $a > 1/2$ the wind at U_4 would reverse

its direction, which obviously does not correspond to the reality. The $a = 1/2$ value corresponds to an upper limit for the validity of this model based on the one-dimensional linear momentum theory (or simply "Betz theory").

The mechanical power captured by the actuator disc can be obtained as the thrust, given by Eq. (4.5), times the wind speed at the disc:

$$P = \frac{1}{2}\rho A(U_1^2 - U_4^2)U_2. \tag{4.9}$$

By substituting the expressions of U_2 and U_4 from Eq. (4.8) into Eq. (4.9), and denoting the free stream (far upstream) wind speed as $U = U_1$, we obtain

$$P = \frac{1}{2}\rho A U^3 4a(1-a)^2. \tag{4.10}$$

If we now divide the harvested power by the power available in the wind flow, given by Eq. (1.1), we obtain the *power coefficient*

$$C_P = \frac{(1/2)\rho A U^3 4a(1-a)^2}{(1/2)\rho A U^3} = 4a(1-a)^2. \tag{4.11}$$

There are two roots to the polynomial $\partial C_P(a)/\partial a$. The first root is $a = 1$ and corresponds to the minimum of the function $C_P(a)$, whereas the other root is $a^* = 1/3$ and corresponds to the maximum of the power coefficient, $C_P(a^*) = 16/27 \approx 0.5926$, also known as the *Betz limit*. This means that any wind power device, under the assumptions here made, can extract no more than about 60 % of the kinetic energy from the wind.

Similarly to the mechanical power, we can also obtain the *thrust coefficient* by replacing the expression of U_4 from Eq. (4.8) into Eq. (4.5), and then dividing the resulting expression by the dynamic force present in the airflow:

$$C_T = \frac{(1/2)\rho A U^2 4a(1-a)}{(1/2)\rho A U^2} = 4a(1-a). \tag{4.12}$$

In Fig. 50 we can see the plots of the power and thrust coefficients just discussed. Observe that, if the axial induction factor grows above the optimal value $a^* = 1/3$, not only does the power start to drop but also the thrust on the actuator disc keeps increasing up to $a = 1/2$. If the device is a horizontal-axis wind turbine, the thrust produces a torque on the foundations at the ground proportional to the tower height. Hence, one should avoid exposing the turbine supporting structure to unnecessarily high loads with $a > 1/3$. Note that, in the case of an AWE tethered wing, the thrust corresponds to the tether traction force, whereas the torque on the foundation should be negligible because

the drum housing the tether is practically at ground level.

Figure 50 – Curves of power and thrust coefficients of the actuator disc, according to Betz theory, as a function of the axial induction factor (a).
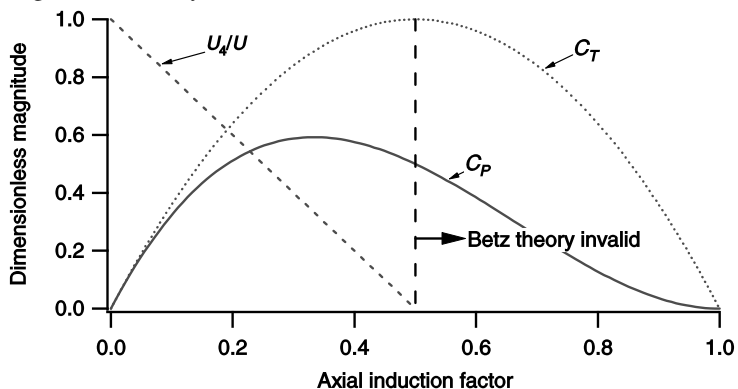
Source: Manwell, McGowan and Rogers (2009)

So far we have related the wind speed at different points along the wind direction with the power and thrust coefficients of the actuator disc immersed in this airflow. This was possible by introducing the axial induction factor a. Although we have determined an optimal value of a for the power extraction, it is still not clear how we can reach such value. We need an enhanced model that considers the aerodynamic curves of the turbine blades, or the tethered wing, and gives us a control parameter/input. Before we do this, let us take an intermediate step in the modeling procedure, where we will introduce the radial dimension of the disc and, by doing so, consider its angular speed.

4.2 ANGULAR MOMENTUM THEORY

Because in the previous section we considered only the axial dimension of the actuator disc, we did not model the rotational effects in the radial direction. For instance, we disregarded real-world effects such as the rotational wake, and the influence of the disc angular speed on the "permeable wall". In this section we will extend the one-dimensional disc model with the radial dimension. We will use the variable dr as an infinitesimal displacement in the direction of the radius r, forming an annular stream tube with cross-sectional area $dA = 2\pi r\, dr$, as shown in the right-hand side of Fig. 51.

Figure 51 – Actuator disc, with axial and radial dimensions, of a generic wind power device immersed in a homogeneous airflow.
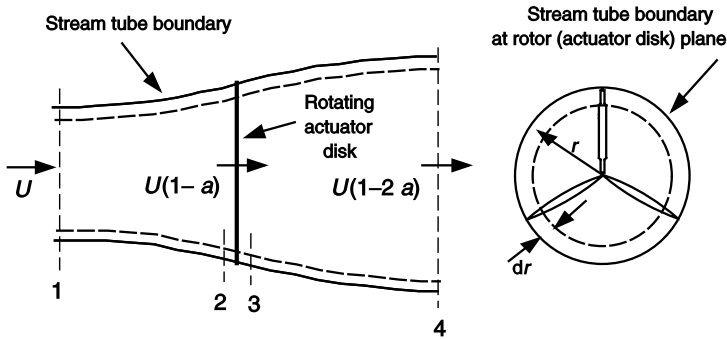
Source: Manwell, McGowan and Rogers (2009)

As a starting point of our analysis, let us now consider that, as the wind flows through the actuator disc, it causes the disc to rotate with an angular speed Ω, i.e. a torque is applied to the disc by the wind. According to the principle of conservation of angular momentum, the disc must then apply a torque of similar magnitude and opposite direction to the wind mass, causing it to rotate with an angular speed ω as the wind continues to flow downstream. The result is a helical trajectory of the wind flow downstream, characterizing the wake rotation. From the principle of conservation of energy, we can say that the work exerted by the thrust upon the actuator disc causes the disc to rotate relative to the wind flow, or vice-versa. From the point-of-view of the wind mass, its angular speed relative to the disc increases from Ω to $\Omega + \omega$, hence a variation of ω inside a time interval Δt, where the average relative wind speed is $\Omega + \omega/2$. We have that the torque exerted upon the disc ring is $m r^2(\omega/\Delta t)$, where $m = \rho \, dA \, U_2 \Delta t$ is the wind mass and $\omega/\Delta t$ is the suffered acceleration. Multiplying this torque by the average angular speed of the wind $\Omega + \omega/2$ inside the Δt interval gives us the harvested mechanical power. The latter is then equal to the power exerted by the thrust: $(p_2 - p_3)dA \, U_2 \Delta t$. Equating both power expressions yields

$$p_2 - p_3 = \rho \left(\Omega + \frac{1}{2}\omega \right) \omega r^2.$$

(4.13)

Hence the thrust on a ring of radius r is

$$dT = (p_2 - p_3)dA = \left[\rho \left(\Omega + \frac{1}{2}\omega \right) \omega r^2 \right] 2\pi r \, dr.$$

(4.14)

Let us now define the *angular induction factor*

$$a' = \omega/(2\Omega).$$ (4.15)

By solving Eq. (4.15) for ω and substituting the result into Eq. (4.14), the expression of the annular thrust becomes

$$dT = 4a'(1+a')\rho\,\Omega^2\,\pi\,r^3\,dr.$$ (4.16)

Note that we can also obtain the thrust on an annular section by multiplying the thrust coefficient of Eq. (4.12) by the ring cross section $dA = 2\pi r\,dr$. The result is

$$dT = 4a(1-a)\rho\,U^2\,\pi r\,dr.$$ (4.17)

By equating the thrust expressions of Eqns. (4.16) and (4.17) we obtain the relationships

$$\frac{a(1-a)}{a'(1+a')} = \frac{\Omega^2\,r^2}{U^2} = \lambda_r^2,$$ (4.18)

where λ_r is the *local speed ratio*, which relates the tangential speed of the ring of radius r to the free-stream wind speed U. If we make $r = R$, where R is the radius of the actuator disc, we obtain the *tip speed ratio*

$$\lambda = \frac{\Omega R}{U} = \frac{R}{r}\lambda_r,$$ (4.19)

an important quantity when optimizing the operating point of the wind power device, as we will see. Again using the principle of conservation of angular momentum, the torque exerted upon the rotor disc must be equal to the variation of angular momentum of the airflow during the Δt time interval in which the wind goes through the disc. Recalling that the wind mass is $m = \rho\,dA\,U_2\,\Delta t$, and the ring area is $dA = 2\pi r\,dr$, the torque becomes

$$dQ = \underbrace{m r^2}_{\text{wind inertia}}\;\frac{\omega}{\Delta t} = \rho\,2\pi\,U_2\,\omega\,r^3\,dr.$$ (4.20)

Substituting $U_2 = U(1-a)$ from Eq. (4.8) and $\omega = 2\Omega a'$ from Eq. (4.15), we can rewrite Eq. (4.20) as

$$dQ = 4a'(1-a)\rho\,U\,\Omega\,\pi\,r^3\,dr.$$ (4.21)

The mechanical power harvested by each annular segment of the actuator disc is $dP = \Omega\,dQ$, in which we can replace Eqns. (4.21), (4.19) and

(4.18) to obtain

$$dP = \frac{1}{2} \rho A U^3 \underbrace{\left[\frac{8}{\lambda^2} a'(1-a)\lambda_r^3 \, d\lambda_r \right]}_{dC_P},$$
(4.22)

where dC_P is the power coefficient of the ring. If we integrate it from $\lambda_r = 0$ (assuming that the blades/wing begin at $r = 0$) to λ we get the total power coefficient of the actuator disc. In order to integrate dC_P in Eq. (4.22), we need to relate the variables a, a' and λ_r. We start by solving Eq. (4.18) for a', whose positive root (the one with physical meaning) is

$$a' = -\frac{1}{2} + \frac{1}{2}\sqrt{1 + \frac{4}{\lambda_r^2} a(1-a)}.$$
(4.23)

Note that, in order to maximize the power production, the term $a'(1-a)$ in Eq. (4.22) should be maximum. Hence, substituting the expression for a' of Eq. (4.23) into $a'(1-a)$ and setting its partial derivative w.r.t. a to zero, the root of physical meaning is

$$\lambda_r^2 = \frac{(1-a)(4a-1)^2}{1-3a}.$$
(4.24)

Substituting this result into Eq. (4.18) yields the relationship between a and a' we were looking for:

$$a' = \frac{1-3a}{4a-1}.$$
(4.25)

If we differentiate Eq. (4.24) w.r.t. a, we obtain a relationship between the infinitesimals da and $d\lambda_r$ at the condition of maximum power production:

$$2\lambda_r \, d\lambda_r = \frac{6(4a-1)(1-2a)^2}{(1-3a)^2} \, da.$$
(4.26)

By using Eqns. (4.24), (4.25) and (4.26) into the expression of dC_P in Eq. (4.22), and taking the integral, we end up with

$$C_{P,\max} = \frac{24}{\lambda^2} \int_{a_1}^{a_2} \left[\frac{(1-a)(1-2a)(1-4a)}{(1-3a)} \right]^2 \, da.$$
(4.27)

The lower integration limit, a_1, is obtained by replacing $\lambda_r = 0$ in Eq. (4.24). The root $a_1 = 1$ does not correspond to a feasible operation (outside the validity interval of Betz theory), whereas the root $a_1 = 1/4$ is the one with physical meaning, that we will work with. As for the upper integration limit,

a_2, it remains as a function of the tip speed ratio by replacing $\lambda_r = \lambda$ in Eq. (4.24). Also, note in Eq. (4.24) that the tip speed ratio goes to infinity as $a \to 1/3$. By solving Eq. (4.27) as a function of λ we get the result shown in Fig. 52. We can see that, because we are now modeling the wake rotation, as the tip speed ratio increases the maximum power coefficient approaches asymptotically the Betz limit. In plain words, the conclusion we take under the set of assumptions made is that, the faster the turbine rotates (or the faster is the tangential speed of the tethered wing), the more energy can be harvested from the wind within the limit established by Betz.

Figure 52 – Maximum power coefficient of the actuator disc as a function of the tip speed ratio.
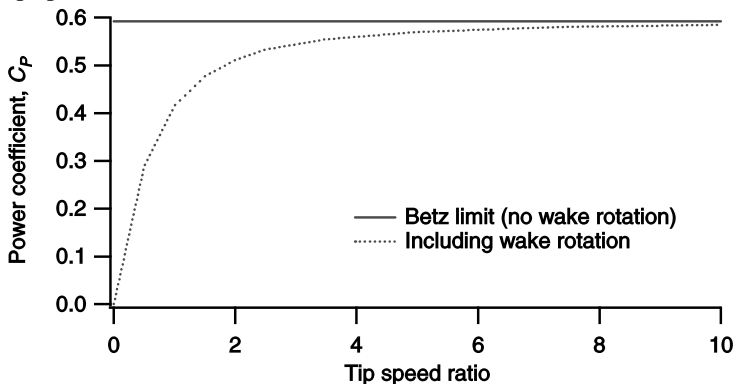
Source: Manwell, McGowan and Rogers (2009)

In spite of the results of Fig. 52, the optimal tip speed ratio of horizontal-axis wind turbines is known to be typically below 10; for faster angular speeds the power extraction progressively diminishes. This effect is due to the combination of lift and drag forces upon the airfoil (blade or wing) as a function of the angle of attack, as we will see in the sequel.

4.3 BLADE ELEMENT MOMENTUM THEORY

So far in this chapter we have analyzed a device extracting the wind power without taking into account the components which actually interface with the wind: the blades of a wind turbine (or the tethered wing). When considering an airfoil with aerodynamic curves resulting in a limited glide ratio, the curve of the power coefficient with wake rotation shown in Fig. 52 becomes an upper limit (ideal case). Even though we will now consider

a discrete number of turbine blades (or one tethered wing), and the airfoil aerodynamic behavior as a function of the blade section through the variable r, we will assume no interaction between the sections comprising the blades, i.e. no radial airflow. In reality, there is a radial flow that contributes to decreasing the efficiency of the airfoil.

The apparent wind reaching the blade is the vector sum of the axial wind component $U(1-a)$, according to Eq. (4.8), and the average apparent (relative) tangential speed $U_{rad} = \Omega + \omega/2$ discussed in Sect. 4.2. If we use the expression of ω from Eq. (4.15), we can reformulate the tangential speed as

$$U_{rad} = r\Omega(1+a').\tag{4.28}$$

The magnitude of the relative (apparent) wind speed reaching the blade section is then

$$U_{rel} = \sqrt{[U(1-a)]^2 + [r\Omega(1+a')]^2}.\tag{4.29}$$

The variables used to model the blade geometry and the aerodynamic forces are depicted in Fig. 53. The blade pitch angle at the blade root (nearest section to the nacelle) is $\theta_{p,0}$, and is used as a control input to optimize the power extraction, or keep it at the rated power for stronger winds. The different twist angle θ_T for each section is what gives the "twisted" shape of a wind turbine blade, and is obtained to optimize the torque on the rotor. The section pitch angle[1] $\theta_p = \theta_{p,0} + \theta_T$ is the angle between the section chord line and the plane of rotation. The angle of relative wind is ϕ, which corresponds to the partial angle of attack, $\Delta\alpha$, of the pumping kite model (see Sect. 2.2), whereas the section pitch angle corresponds to the base angle of attack, α_0. The difference here is that, instead of having the (total) angle of attack of each section as the sum of the partial ($\Delta\alpha$) and base (α_0) components, the relationship is

$$\phi = \theta_p + \alpha = (\theta_{p,0} + \theta_T) + \alpha.\tag{4.30}$$

The lift and drag forces on a blade section are dF_L and dF_D, respectively. From their vector sum we obtain the total aerodynamic force, which can be decomposed as a component in the axial (normal) direction, the thrust dF_N, and a component in the radial direction, dF_T. From Fig. 53, the definition of the local speed ratio λ_r in Eq. (4.18), the definition of the aerodynamic forces as used in Eq. (2.37), and knowing that c is the section chord length,

---

[1]Note that, in a tethered wing, we have $\theta_T = 0$.

Figure 53 – Blade geometry and variables used to model the blade aerodynamics, from the perspective of looking down from the blade tip.
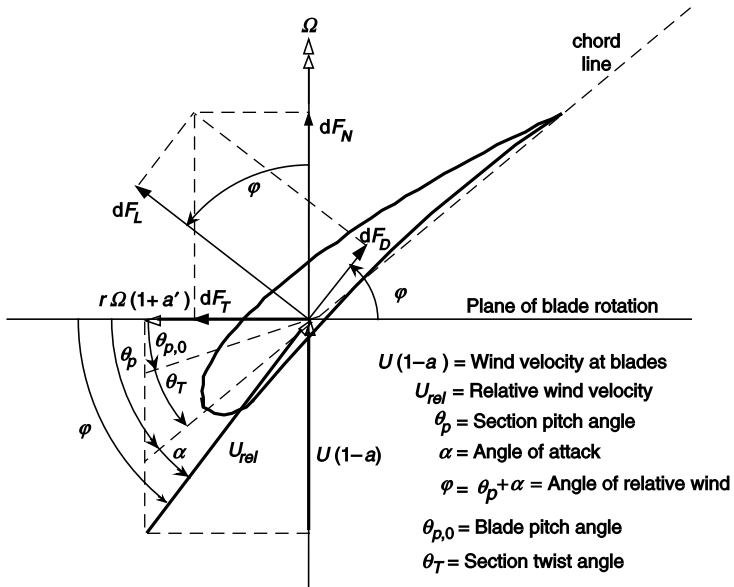
we obtain the following relationships:

$$\tan\phi = \frac{U(1-a)}{\Omega r(1+a')} = \frac{1-a}{(1+a')\lambda_r} \tag{4.31a}$$

$$U_{\text{rel}} = \frac{U(1-a)}{\sin\phi} \tag{4.31b}$$

$$dF_{\text{L}} = (1/2)\,\rho\,C_l\,U_{\text{rel}}^2\,c\,dr \tag{4.31c}$$

$$dF_{\text{D}} = (1/2)\,\rho\,C_d\,U_{\text{rel}}^2\,c\,dr \tag{4.31d}$$

$$dF_{\text{N}} = dF_{\text{L}}\cos\phi + dF_{\text{D}}\sin\phi \tag{4.31e}$$

$$dF_{\text{T}} = dF_{\text{L}}\sin\phi - dF_{\text{D}}\cos\phi \tag{4.31f}$$

Assuming that the actuator disc has B blades, substituting Eqns. (4.31c), (4.31d) and (4.31b) into Eq. (4.31e) yields the total thrust differential at a ring of radius r of the disc:

$$dF_N = \frac{1}{2}\rho B (C_l \cos\phi + C_d \sin\phi) \frac{U^2(1-a)^2}{\sin^2\phi} c\,dr. \qquad (4.32)$$

Similarly, we can calculate the total torque differential at the ring:

$$dQ = B r\,dF_T = \frac{1}{2}\rho B (C_l \sin\phi - C_d \cos\phi) \frac{U^2(1-a)^2}{\sin^2\phi} c r\,dr. \qquad (4.33)$$

Observe that the drag force has the negative effects of increasing the thrust and decreasing the torque, in the case of a wind turbine. These effects are amplified when the actuator disc rotates at a higher angular speed Ω, thus causing ϕ to diminish. Using Eqns. (4.33), (4.31b) and (4.19), we can compute the total power harvested by the horizontal-axis turbine as

$$P = \int_{r_0}^{R} \Omega\,dQ = \frac{1}{2}\rho U^3 \frac{\lambda B c}{R} \int_{r_0}^{R} \frac{(1-a)^2}{\sin^2\phi}(C_l \sin\phi - C_d \cos\phi) r\,dr. \qquad (4.34)$$

Let us define the *local solidity*

$$\sigma' = \frac{B c}{2\pi r}, \qquad (4.35)$$

which represents the ratio between the ring arc occupied by the blades w.r.t. the total ring perimeter. Assuming that the blades begin at a radial distance r_0 from the rotor center, we can define the equivalent rotor radius $R_b = \sqrt{R^2 - r_0^2}$. Eq. (4.34) can then be rewritten as

$$P = \underbrace{\frac{1}{2}\rho \pi R_b^2 U^3}_{\text{wind power}} \underbrace{\frac{2\lambda}{R_b^2 R} \int_{r_0}^{R} \frac{\sigma'(1-a)^2}{\sin^2\phi}(C_l \sin\phi - C_d \cos\phi) r^2\,dr}_{\text{power coefficient, } C_P}. \qquad (4.36)$$

Before we can numerically integrate C_P in Eq. (4.36), we need to find a relationship between a, a' and ϕ. This can be achieved by equating both expressions for the torque differential: Eq. (4.21), obtained only with the conservation of angular momentum, and Eq. (4.33), obtained through the aerodynamic forces on the blades. The result is

$$a' = \frac{\sigma'(C_l \sin\phi - C_d \cos\phi)}{4\lambda_r \sin^2\phi}(1-a). \qquad (4.37)$$

In a similar way, the other relationship comes from equating the thrust expressions of Eqns. (4.17) and (4.32). We obtain

$$\frac{a}{1-a} = \frac{\sigma'(C_l \cos\phi + C_d \sin\phi)}{4\sin^2\phi} = x \;\Rightarrow\; a = \frac{x}{1+x}. \qquad (4.38)$$

To compute the solution of (ϕ, a, a') at each blade section, we use an iterative procedure similar to that suggested by Manwell, McGowan and Rogers (2009). Basically, we define a tolerance, $tol = 10^{-3}$, and set the initial guesses of the induction factors as $a_{\text{old}} = 1/3$ and $a'_{\text{old}} = 0$. These particular values are chosen because they are asymptotes in the ideal case of a machine with no drag and infinite number of blades, thus helping in the convergence of the algorithm for high tip speed ratios. Having initialized (a, a'), we then enter a while-loop in which we first compute ϕ using Eq. (4.31a), followed by the computation of a_{new} using Eq. (4.38), and then a'_{new} using Eq. (4.37). Next, we compute the norm of the error vector $norm\_err = (a_{\text{new}}, a'_{\text{new}}) - (a_{\text{old}}, a'_{\text{old}})$. If $norm\_err < tol$ the algorithm has converged and we leave the while-loop, else we keep iterating. Besides the particular initialization values for (a, a'), the convergence of the algorithm for high values of tip speed ratio is also facilitated if we make $C_d = 0$ in Eqns. (4.38) and (4.37). This yields negligible errors in the solution found in the case of efficient airfoils (with high C_l/C_d). Note that, in spite of the assumption $C_d = 0$ to compute the solution, we still consider the drag coefficient when computing the C_P of the wind turbine through Eq. (4.36).

For the following numerical results regarding the wind turbine, we will consider the aerodynamic characteristics of three airfoils from the National Renewable Energy Research Laboratory (NREL), shown in Fig. 54. We will assume a constant chord length for all blade sections (i.e. along the r dimensions), $c = 2.5\,\text{m}$, although the optimal c typically changes with r. The *root* airfoil is at the base of the blade, at $r_0 = 1\,\text{m}$, whereas the *primary* airfoil is at 75 % of the rotor radius $R = 45$, and the *tip* airfoil is at 95 % of R. The $C_l(\alpha)$ and $C_d(\alpha)$ coefficients of each blade section result from the linear interpolation of the corresponding coefficients of these airfoils. Note in Fig. 54 how apparently slight modifications on the airfoil shape cause relatively big changes on the aerodynamic coefficients. The root airfoil is the thicker, also due to the more demanding structural (load) constraints. On the other hand, the tip airfoil is the thinner, thus becoming the more aerodynamically efficient between 1 and 6 degrees of angle of attack.

In fact, observe how the maximum aerodynamic efficiency E reaches about 170 for the tip airfoil, which is about 24 times the maximum efficiency of the foil kite of Fig. 33. The Pumping Kite (PK) equivalent aerodynamic

Figure 54 – Aerodynamic characteristics and shape of the three NREL airfoils comprising the blades of a wind turbine: S818 (root), S827 (primary) and S828 (tip).
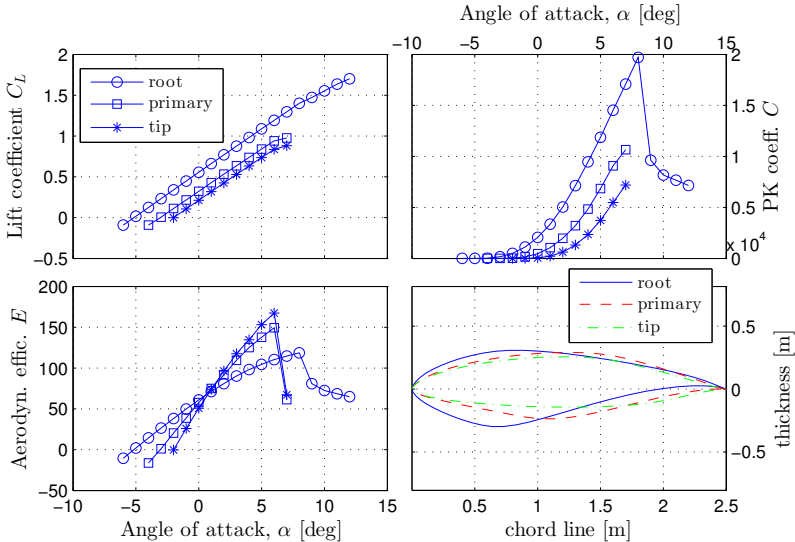
coefficient C of Eq. (2.50), upon which the power depends linearly, is in average about 330 times greater for the NREL airfoils. Because of the high sensitivity of the pumping kite models from Sects. 2.2 and 2.3 on the aerodynamic coefficients C and E, if we were to use these NREL airfoils we would obtain unrealistically high values of power (and other affected variables) for the pumping kite. What happens is that the reverse effect of the tethered wing slowing down the airflow going through the disc, as the wing tangential speed increases, is not considered in those models. Further in this section we will formulate an expression for the harvested power of the traction phase of a pumping kite (Loyd's lift mode), flying in a circular trajectory, using blade element momentum theory. The solution of that power expression should respect the Betz limit, derived in Sect. 4.1, for any given value of aerodynamic efficiency, thus becoming a more appropriate model for the case of more efficient wings.

In Fig. 55 we can see some numerical results for the considered wind turbine. Keep in mind that all the results were obtained by optimizing the angle of attack of each blade section, i.e. independently choosing the angle of

attack that maximizes the contribution dC_P of each section to the total power coefficient C_P. Observe that, for a hypothetical one-bladed turbine, the peak on C_P occurs at a relatively high tip speed ratio. As we add more blades to the turbine, the optimal λ decreases. This happens because, if λ remains the same, the increasing number of blades tends to progressively slow down the wind reaching the disc (thus to increase a above the optimal value $a^* = 1/3$). Also note that the higher maximum C_P is obtained with 5 blades, at the lower optimal tip speed ratio (around 6). It can be shown that, for a wind turbine airfoil with no drag (thus infinite efficiency), the highest C_P is obtained with an infinite number of blades, and the C_P curve approaches asymptotically the Betz limit as the tip speed ratio increases to infinity, according to the dotted curve of Fig. 52. Modern, utility-scale wind turbines have converged to 3 blades, among other factors, because of the higher cost and added complexity of adding up blades to the rotor. Nonetheless, note that the decrease in the maximum C_P is small when comparing the 5-blade case ($C_\mathrm{P} = 0.5531$) to the 3-blade case ($C_\mathrm{P} = 0.5445$): a 1.6% decrease considering these NREL airfoils.

Figure 55 – Optimization results of a wind turbine with rotor radius of 45 m and a combination of the NREL airfoils S818 (blade root), S827 and S828 (blade tip).
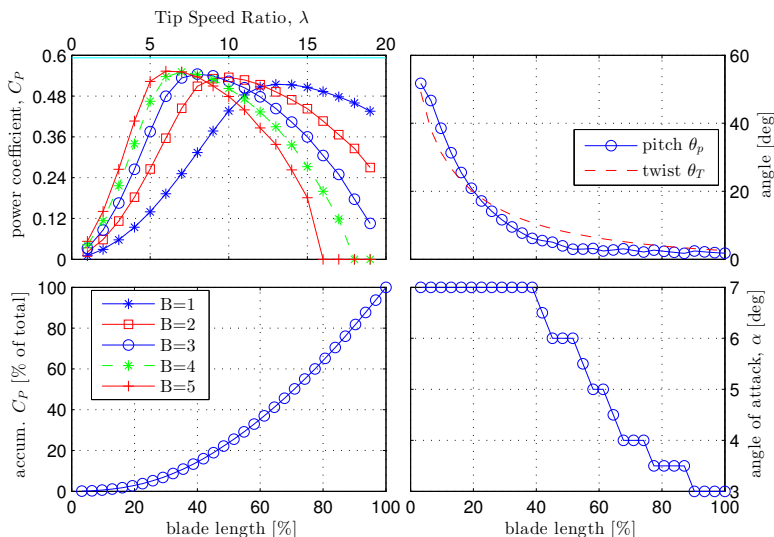
Source: original

As already stated, for the results of Fig. 55 we have optimized the angle of attack[2] at each blade section, as shown in the bottom-right plot. We can see that α decreases along the blade length towards the tip. Given α and the angle of the relative wind ϕ found for each section, we can calculate the pitch angle by using Eq. (4.30), as shown in the upper-right plot. If we assume a null base pitch angle, i.e. $\theta_{p,0} = 0$, the pitch corresponds to the twist angle, which can be interpolated by a function[3] and used for the blade design. This result corroborates the typical characteristic of the blades of horizontal-axis wind turbines: the blade leaves the nacelle with a high twist angle, and "unwinds" itself towards the tip.

Probably the most important result of Fig. 55, which is often used to promote the development of AWE, is in the lower-left plot. The curve shows the accumulated power coefficient (integrated dC_P) along the radial direction towards the tip of the blades. We can clearly see that the half of the blade area connected to the root (nacelle) contributes only to about 20% of the whole power harvested by the turbine. Therefore, much more than its contribution to the power, the main role of the first half of the blade is to support (hold in place) the outermost half. This conclusion leads us back to the hypothesis presented in the beginning of Sect. 1.3.1: if we could eliminate the tower, nacelle and the first half of the blades, and find a way to keep the second blade half airborne, we could still generate about half of the original power, yet with a structure orders of magnitude lighter. Consequently, transportation and installations costs should decrease dramatically, and the economical return on the investment should be higher, as argued by Lellis et al. (2016).

Let us consider from now on the turbine with 3 blades, following the de-facto standard of nowadays. Its peak power coefficient is around 91.9% of the Betz limit – a high value even for the current state-of-the-art technology. In practice, there are several sources of inefficiency that must be applied to the theoretical C_P of Fig. 55 in order to get a realistic value of electric power generated. Among these sources are mechanical losses (e.g. friction in the gearbox), electrical losses in the generator, and aerodynamic losses at the tip of the blades[4] and between the blade sections. We will consider that these combined losses result in an efficiency factor $\zeta = 0.7$, that we should multiply by the harvested mechanical power in order to compute the electric power. Hence, in the case of our hypothetical 3-bladed turbine, the electric power coefficient we will consider from now on is $C_{P,ele} = 0.7 \cdot 0.5445 \approx 0.3811$.

---

[2]We have used a resolution of $0.5°$ for the angle of attack.

[3]In the upper-right plot of Fig. 55 we used the ad-hoc function for the twist angle $\theta_T = -0.09 \ln(0.5\,r/R)/((r/R) + 0.4)$, where $\ln()$ is the natural logarithm.

[4]Similarly to the recirculation of air from the lower to the upper part of an airplane wing at its tip. To minimize these losses, modern aircraft are equipped with winglets.

4.3.1 Power curves of a wind turbine and a pumping kite

To conclude our discussions on the wind turbine, let us now compute its (electrical) power curve and compare it to the power curve of the pumping kite. We will again take as an example the location of Schleswig, Germany, and vary the wind speed v_{ref} at the reference height $z_{ref} = 30\,m$. According to Eq. (4.36), the harvested power of the turbine (P curve in Fig. 56) is the product between the power coefficient and the power in the airflow going through the rotor swept area. We will also consider five variants of the pumping kite:

a) similar parameterization as in Sect. 3.3: projected wing area of $330\,m^2$, which is equal to the total area of the three turbine blades combined; foil (ram-air) kite with maximum aerodynamic efficiency around 7, and reel speed saturation at $10\,m/s$. The differences here are: (i) we are saturating the mechanical traction power at $2\,MW/\zeta$, where $\zeta = 0.7$ is the same efficiency factor considered for the turbine; (ii) the tether diameter was increased by $4\,mm$, becoming $d_t = 22\,mm$; (iii) motivated by the results of Sect. 3.2.4 and as long as the traction force is not saturated, we will use an ad-hoc optimal reel-out speed equal to 3/4 of the value given by Eq. (1.5), that maximizes the traction power. The cycle power is denoted by the P_{cyc} curve, whereas the traction power is represented by P_{tra}. We will refer to this setup as the "standard" pumping kite;

b) similar to a), except that the projected wing area is increased by 50%, reaching $495\,m^2$. The cycle power is denoted by the P_{cyc} (1.5A) curve;

c) similar to a), except that the aerodynamic efficiency of the foil kite is increased by 50%, reaching a maximum around 10.5. The cycle power is denoted by the P_{cyc} (1.5E) curve;

d) similar to a), except that the maximum reel-speed, which is used during the ad-hoc retraction phase, is increased by 50%, reaching $15\,m/s$. The cycle power is denoted by the P_{cyc} (1.5$v_{t,sat}$) curve;

e) a combination of the three previous variants with respect to the setup of item a). The cycle power is denoted by the P_{cyc} (all) curve;

The power curve results are shown in Fig. 56. We can see that the turbine generates more power than the standard pumping kite at all (reference) wind speeds. Note that, when the turbine reaches saturation at $2\,MW$ at a wind speed around $11\,m/s$, the pumping kite cycle power is about $750\,kW$, even though at a slightly stronger wind, around $15\,m/s$. This happens as a

Figure 56 – Electrical power curves of a 2 MW horizontal-axis wind turbine and five variants of a 2 MW pumping kite, for the location of Schleswig, Germany. The reference height is $z_{\text{ref}} = 30\,\text{m}$.
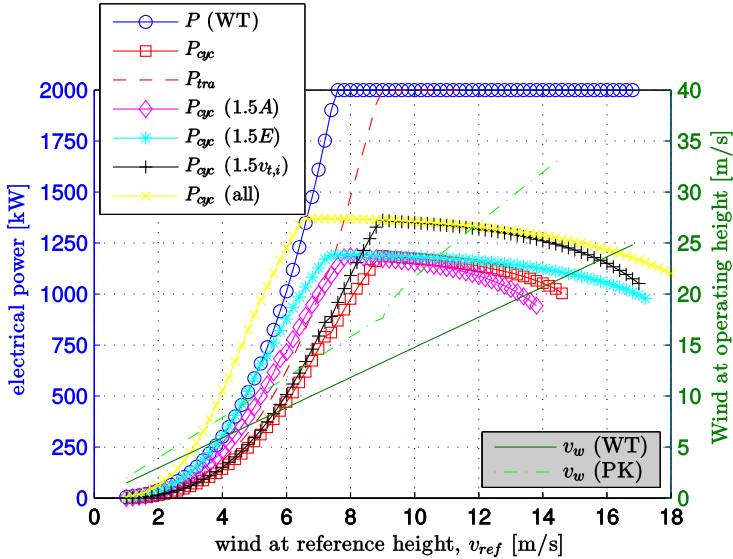
Source: original

consequence of the much higher aerodynamic efficiency of the NREL airfoils used for the turbine blades – about 24 times more efficient than the foil (ramair) kite, of Fig. 33, used for the pumping kite. Moreover, the cycle (net) power delivered by the AWE device is negatively impacted by the retraction phase: the significant traction force and time required for the reeling-in of the tether is the reason for the vertical gap between the traction power (P_{tra}) and cycle power (P_{cyc}) curves in Fig. 56.

We could argue that comparing both wind power devices based on an equal total wing area could be too restrictive for the pumping kite, since the cost per area of the flexible kite should be much lower than for a rigid turbine blade. Hence, while adding more blade area to a wind turbine could be economically disadvantageous, increasing the flexible wing area in a pumping kite would most likely result in an augmentation of the revenues from the power plant, since the increment in the generated power would pay off for the increase in the wing area. Observe in Fig. 56 that a 50 % increment in the projected wing area has indeed increased the harvested power at lower wind speeds, yet still not reaching the turbine power curve. At higher wind

speeds the cycle power curve decreases faster than in the case of the standard pumping kite due to the stronger drag on the wing.

Another possible improvement on the pumping kite is on the aerodynamic efficiency of the foil (raim-air) wing. Keep in mind that the considered curves, of Fig. 33, correspond to an existing kite tuned for towing sea-going vessels. The best current paragliding kites, used for racing, are known to achieve an aerodynamic efficiency around 10, which corresponds to an increment of roughly 50 % on the efficiency considered for the standard pumping kite. Observe in Fig. 56 that improving the aerodynamic efficiency has a stronger positive impact on the net power than increasing the wing area: this time, the pumping kite power curve reaches the turbine power curve for reference wind speed up to approx. 5 m/s. Furthermore, at stronger wind speeds, the decrease in the cycle power is less intense. This is an important observation to foster the research in the development of more efficient flexible wings.

A third opportunity for improvement on the pumping cycle regards the reel speed limitation. In the ideal case of a retraction maneuver with insignificant traction force, the vertical gap between the traction and cycle power curves would be solely due to the reel speed saturation. Hence, if the traction phase duration could be made arbitrarily small, the mentioned vertical gap would tend to disappear. When assuming an improved ground winch capable of reeling in 50 % faster than in the standard scenario, we can see an overall improvement on the cycle power curve, although not in the same proportion due to the non-negligible traction force during the retraction phase. As we will see in Sect. 4.4, this more significant improvement on the cycle power for higher wind speeds does not impact much the capacity factor because the observation frequency of faster winds is usually low.

Finally, by combining the 50 % increments in the projected kite area, aerodynamic efficiency and reel-in speed saturation, we can see in Fig. 56 that the pumping kite power curve improves substantially, generating more power than the wind turbine for reference wind speeds up to approx. 6.5 m/s, which corresponds to a wind speed near 10 m/s at the turbine. We should bear in mind that the increase in the cycle power could be, in fact, more modest. This is due to the decrease in the equivalent drag coefficient that comes along with an increase in the tether diameter in order to match the higher traction force, as discussed in Sect. 3.2.4. Even so, the results in Fig. 56 suggest that combined improvements on different aspects of the AWE system, with respect to the technology that is available today, could allow the pumping kite to generate a net power equivalent to that of current wind energy technology, if not more. When adding to this observation the expectation of overall reduced costs – especially on transportation, installation and materials –, a promising scenario is formed for the future development of this AWE con-

cept based on flexible wings (kites). We should note, however, that although upfront costs can be lower for AWE with respect to conventional wind energy technology, it is still uncertain whether operational and maintenance costs can be limited to the same levels found with the tower-based turbines. For instance, the frequency of maintenance of the individual components such as wing and cables, and the impact that these maintenance procedures would have on the economics of the power plant is still hard to assess quantitatively. These points should become more clear when aspects such as launching and landing strategies become more mature, and more extensive testing of AWE systems in longer time intervals are carried out.

One could argue that the comparison between the wind turbine and pumping kite power curves may still be biased by the fact that the models we have used deal differently with the aerodynamic efficiency. Let us recall that, for the ideal case of an airfoil with no drag (thus infinite efficiency), the turbine power reaches the Betz limit according to the models of this section, whereas the pumping kite power goes to infinity according to the models of Sects. 2.2 and 2.3. Hence, if we were to reproduce the results of Fig. 56 for a rigid-wing pumping kite, with an aerodynamic efficiency equivalent to the NREL airfoils, we could be running into a significant overestimation of the AWE power curve. To cope with this and improve the conditions for comparison, we should work with the same modeling framework for both systems. In this case, using Blade Element Momentum (BEM) theory would be more appropriate because it respects the power limit shown by Betz. With this motivation in mind, let us discuss, in the following section, how Loyd's lift mode system (the pumping kite traction phase) can be analyzed using BEM theory.

4.3.2 Application to airborne wind energy

One important observation about the Betz limit for extraction of power from the airflow by an actuator disc in Sect. 4.1 is that, for the derivation of the limit, it was not assumed a specific means of power extraction. In other words, we have not specifically assumed the power as the torque on the actuator disc multiplied by its angular speed (wind turbine), nor the power as the thrust on the disc times the reel-out speed of the disc (Loyd's lift mode), not even the power as the tangential speed on the disc times the useful drag[5]

---

[5]By "useful drag" we mean the axial force to which a turbine attached to the tethered wing is subject when extracting power from the tangential component of the apparent wind, i.e. the thrust force discussed in this section. Added to this useful drag there is the drag on the tethered wing, which does not execute useful work (power extraction).

force tangent to the disc (Loyd's drag mode). The generalization was done as the power being obtained through the thrust times the speed of the wind going through the actuator disc, which can be more or less permeable to the airflow, depending on the axial induction factor a. Hence, if we now consider that the tethered wing is a fraction of only one blade of the disc (see Fig. 51), the Betz limit automatically applies to AWE devices operating in crosswind. This brings us to the question: how to compute the power coefficient of lift and drag mode AWE devices?

Applying BEM theory to Loyd's lift mode is, in principle, simple. The idea is that the actuator disc is not only rotating, but also moving downstream at a speed v_t, i.e. the reel-out speed. Hence, in the expression of the differential thrust of Eq. (4.32) the wind speed far upstream U becomes $U - v_t$. The harvested power P is then obtained as the integral of this modified differential thrust times the reel-out speed v_t. Knowing that the harvested power is $P = (1/2) \rho \pi R_b^2 U^3 C_P$, where $R_b = \sqrt{R^2 - r_0^2}$ and $R - r_0 = w_s$ is the projected wingspan, the power coefficient becomes

$$C_P = \underbrace{\frac{2(U - v_t)^2 v_t}{R_b^2}}_{\text{gain } k_L} \int_{r_0}^R \frac{\sigma'(1-a)^2}{\sin^2 \phi} \left(C_l \cos \phi + C_d \sin \phi\right) r \, dr. \qquad (4.39)$$

Note that the power coefficient can be expressed as a gain $k_L(v_t)$ applied to an integral. Hence we need to find the value of v_t that maximizes this gain and, consequently, C_P. By doing $\partial k_L(v_t)/\partial v_t = 0$ we obtain two roots: the root $v_t = U$ corresponds to the minimum of $k_L(v_t)$, whereas $v_t^* = (1/3)U$ corresponds to the maximum. Because here we are assuming ideal crosswind conditions with $\theta = \pi/2$ and $\phi = 0$, observe that the optimal reel-out value just found corresponds to the "classic" solution $v_t^* = (1/3)v_w \sin \theta \cos \phi$ obtained by analyzing the model of Sect. 2.3. If we apply $v_t = (1/3)U$ to the power coefficient gain it becomes $k_L^* = 8/(27 R_b^2)$. Recalling that the Betz limit is $C_{P,max} = 16/27$, then the maximum value of the integral in Eq. (4.39) must be $2R_b^2$.

Unfortunately, using the same iterative procedure to compute the solution (ϕ, a, a') at each section of the wingspan, proposed by Manwell, McGowan and Rogers (2009) and based on Eqns. (4.37) and (4.38), did not yield numerical results that seem correct. We will leave this question open for future investigations. It would be a valuable contribution to the AWE field the use of Betz theory and the models based on the conservation of energy, as the ones discussed in this chapter, to analyze and optimize AWE devices based on Loyd's lift and drag modes.

4.4 AVERAGE POWER GENERATION

As mentioned in Sect. 1.1.2, another important aspect of a wind power device, besides its power curve, is the capacity factor:

$$C_{\mathrm{f}} = \frac{P_{\mathrm{avg}}}{P_{\mathrm{nom}}}, \tag{4.40}$$

where P_{avg} is the average electric power produced within a given time interval, and P_{nom} is the rated electric power of the device. Given its power curve and the wind histogram f_{obs} at the operating height z, the average power can be computed as

$$P_{\mathrm{avg}} = \sum_{n=1}^{N} P(v_{\mathrm{w}}(n)) \, f_{\mathrm{obs}}(v_{\mathrm{w}}(n,z)) \tag{4.41}$$

over a discrete interval with N elements of $v_{\mathrm{w}}(n)$ at the operating height of the device. In our case, because the pumping kite may change its average operating height depending on the roughness coefficient z_0 of the wind shear model in Eq. (2.66) for a specific location, we computed the power curve as a function of the reference wind speed v_{ref}. To facilitate the comparison, we also computed the wind turbine power curve as a function of v_{ref}. Therefore, one way to obtain the average produced power using Eq. (4.41) is by computing the histogram at the reference height z_{ref}. Let us recall, from Sect. 2.5, that we have used a strategy of extrapolating each wind sample $v_{\mathrm{w}}(n,z)$ obtained from the NREL database to any height of interest z by using the wind shear model, once z_0 had already been computed through least-squares. The motivation was that, because of the often poor distribution of wind samples along the altitude range (among the altitude slots), the histogram for the nacelle height ($z = 80\,\mathrm{m}$) in such cases was not representative. We consider this strategy valid because, for instance, if a given wind sample $v_{\mathrm{w}}(z_1, n)$ at an altitude z_1 is stronger than the average value given by the logarithmic curve (see Fig. 27), then the wind speed at a different altitude z_2 must also be higher than average, according to the roughness coefficient z_0. Hence, since the power curves were already computed as a function of v_{ref}, we will use this extrapolation strategy to compute the histogram at z_{ref} and, finally, to obtain the average power through Eq. (4.41).

For the following numerical results, we will consider the locations of Table 3, the 2 MW wind turbine (WT), and the five variants of the 2 MW pumping kite (PK) explained in Sect. 4.3.1. The power coefficients obtained by the convolution of the power curves with the histogram at the reference height are shown in Table 8, where the green-shaded cells denote a higher

capacity factor of the pumping kite compared to the wind turbine. We can see that the turbine generates more average power than the standard pumping kite in all locations. Again, the much higher aerodynamic efficiency of the NREL airfoils used for the blades are responsible for this result. Nevertheless, the different power curves and wind histogram at each location causes the capacity factor of the wind turbine to vary between less than twice (as in Belém and De Bilt) and less than four times (as in Fortaleza) the value of the standard pumping kite. In this regard note that, given the assumed lower costs of the AWE-based power plant, the minimum capacity factor to allow for economical feasibility should be lower as well. Therefore it is possible that, for some of the locations where the turbine is not economically attractive, the pumping kite capacity factor could already be at a level to motivate an utility-scale wind power project.

Table 8 – Capacity factors, from January/2013 through January/2016, for a 2 MW wind turbine (WT) with NREL airfoils, a 2 MW pumping foil kite (PK) and its three variants: 50% more reel-in speed (PK $1.5\,v_{t,i}$), 50% more area (PK $1.5A$), 50% more aerodynamic efficiency (PK $1.5E$), and all previous three variants combined (PK all).

Location	WT [%]	PK std. [%]	PK $1.5\,v_{t,i}$ [%]	PK $1.5A$ [%]	PK $1.5E$ [%]	PK all [%]
Belém/PA, Brazil	14.93	9.07	9.72	14.38	18.29	28.46
Manaus/AM, Brazil	8.95	3.82	4.10	6.21	7.95	13.01
Fortaleza/CE, Brazil	37.75	11.01	11.81	17.21	21.55	32.89
Porto Velho/RO, Brazil	7.14	2.86	3.08	4.69	6.02	10.05
Alta Floresta/MT, Brazil	17.16	4.94	5.32	7.75	9.72	15.44
Brasília/DF, Brazil	20.07	6.81	7.29	10.85	13.82	21.95
Confins/MG, Brazil	16.68	5.61	6.00	9.09	11.66	18.96
Foz do Iguacu/PR, Brazil	34.55	13.19	14.38	18.83	22.49	32.45
Florianopolis/SC, Brazil	19.39	7.19	7.75	11.07	13.75	21.06
Porto Alegre/RS, Brazil	16.04	7.89	8.52	12.05	14.88	22.48
De Bilt, the Netherlands	27.85	15.67	17.11	22.03	26.12	36.66
Schleswig, Germany	42.11	20.58	22.86	27.10	31.29	41.99
Brindisi, Italy	33.35	11.12	12.11	16.01	19.20	27.95

Source: original

Now analyzing the pumping kite variants, when adding 50% more

reel-in speed capability, the increment in the capacity factor is small. This is because the advantage of reeling in faster is more evident at higher wind speeds, when the traction phase duration is shorter. However, faster wind speeds occur very seldom, and therefore the contribution to the convolution of Eq. (4.41) is small, about 1 %. On the other hand, when adding 50 % more wing area, the positive impact on the capacity factor is larger, increasing between 50 % and 100 %. Among the three possible improvements on the AWE system, the most impacting one is on the aerodynamic efficiency, though. Observe that, in the case of Belém, the pumping kite overtakes the wind turbine in terms of average power generation – which is due to the favoring wind shear behavior at that site (see Fig. 27). At last, when considering all the three improvements simultaneously, the pumping kite capacity factor overtakes that of the wind turbine in most of the locations. In Belém this relative increment is the largest, almost twice as much average power. In the remaining locations, where the pumping kite still does not generate more average power, the AWE generation becomes very close to the wind turbine performance. The reason for this is that the most frequent wind speed values are usually observed in the region where the power curve of the wind turbine and the improved pumping kite are growing (see Fig. 56) and equivalent.

As we have already mentioned, the investment in a pumping kite unit is expected to be significantly lower than in a horizontal-axis wind turbine of same rated power. Therefore, in face of the results in Table 8, we are left with the following question: what would be the minimum value of the pumping kite capacity factor that would turn a hypothetical wind farm based on pumping kite units into an economically feasible power plant? Studies in this direction would be a valuable contribution to the field and are the subject of ongoing research, as an extension of the work of Lellis et al. (2016).

5 CONCLUDING REMARKS

Airborne Wind Energy (AWE) is an alternative approach, that has been more intensively investigated in the past ten years, to harvest the wind power. This new approach is currently moving from the stage of technology demonstration towards establishing commercial viability (see Zillmann and Hach (2014)). We can mention two main motivations that foster the increasing research and development in the area. First is the fact that, for being capable to remain airborne by either aerodynamic or aerostatic forces, AWE devices do not need a rigid, heavy and expensive tower to operate. This cuts down on the usually high costs of transportation/logistics and assembly of wind power plants. Moreover, in case that the wing is made of flexible material (fabric), the reduction in the transportation costs is even more dramatic. Basically, one replaces the rigid tower and nacelle of a horizontal-axis wind turbine by one or more tethers, whereas the rigid blades are substituted by a rigid or flexible wing, or even a tethered buoyant device holding a light-weight wind turbine. The second attractive aspect of AWE is the possibility of operating at higher altitudes than those reached by the blade tips of the current tower-based wind turbines, which is possible by reeling out the tether(s) of the AWE device to a larger length. Since the general behavior of the airflow is to become more laminar, constant and stronger as the altitude increases, operating at higher altitudes becomes clearly an advantage.

Among the several configurations of AWE devices already proposed in the literature, the so-called pumping kite draws attention by probably being the simpler one to experiment with. Because the generator is located at the ground, the tethered wing may consist of a flexible kite, and thereby the system becomes cheaper and simpler to build. Motivated by these advantages, this doctoral dissertation proposed contributions in several aspects of AWE technology, giving emphasis to the pumping kite configuration. The overall goal was to carry out a rather comprehensive (but not exhaustive) study that could serve either as a manuscript for those intending to get acquainted with how the technology works, as well as a reference point for more specific investigations in the field.

5.1 SUMMARY OF THE CONTRIBUTIONS

After an introductory chapter, the first contribution was to discuss several models that can be used to simulate, analyze, and to design controllers for tethered wings. First, it was derived in detail the 3D two-tether actuation con-

cept which, due to its relative simplicity and reasonable accuracy in modeling the wing translational dynamics, is often used to validate flight control laws, especially when simulation in real time is desired. In order to make the model more accurate from the point of view of physics, adjustments on the effect of the tether mass on the weight, apparent forces and on the equations of motion were proposed. We also revisited the model for the course angle dynamics – an important variable that is often used to design flight controllers. Again, the focus was to be instructive, explaining all assumptions and intermediate steps to get to the model. In the sequel we discussed the logarithmic wind shear model, which is often considered in the literature to represent how the average wind speed increases with the altitude up to about 600 m. Based on data publicly available from the ESRL database, the model was interpolated for several sites around the world. It was also briefly explained how to generate the respective wind histograms, representing the frequency of observation of the different wind speed intervals for a specific location.

A second contribution of this dissertation was on the control aspect of AWE. A decentralized topology was considered, where the control laws of the ground winch and the tethered wing are computed separately. Regarding the task of flight control specifically, the idea was to compare different control laws in a two-loop cascade scheme used for both operating phases of the pumping kite. During the traction phase, the outer loop uses Bernoulli's lemniscate as a reference for the lying-eight flight trajectory and, based on the tracking error, generates a course angle reference for the inner loop. For the retraction phase, the course angle reference is set to the zenith to move away from the high-power zone (crosswind condition) and thus allow for an efficient reel-in maneuver. It was also discussed a simpler strategy for the outer loop during the traction phase, consisting of only two attraction points (attractors), with only one of them being active at a time. We discussed how the bang-bang may be advantageous to control tethered wings flying in trajectories with a short perimeter (arc length), in which case the controller sampling rate becomes relatively low, whereas continuous references (as Bernoulli's lemniscate) may be more adequate for trajectories with a wider perimeter.

As for the inner loop, three variants were investigated. The first one consists of a simple proportional controller. Using the model of the course angle open-loop dynamics, a feedback linearization controller was designed in order to guarantee a first-order linear dynamics to the course angle tracking error. The third variant is the previous linearizing controller without the derivative of the course angle reference, generated in the outer loop, which may be hard to obtain free of significant noise. When comparing the three variants considering an approximately same closed-loop pole, the complete feedback linearization controller achieved a better performance, whereas the

variant without the derivative term, although remaining stable, performed worse than the proportional controller.

A third area to which this dissertation has contributed is the optimization of a pumping cycle when considering the decentralized topology already mentioned. Because the flight control law is computed separately from the ground winch, we need to choose values for some operating parameters, and this choice may have a significant impact on the net power delivered by the AWE system. For instance, regarding the traction phase, it was shown how the base angle of attack can be computed from the angle of attack that maximizes the traction power. In this particular topic, the contribution was to demonstrate that the optimal angle of attack is not significantly influenced by the tether drag. It was also shown how the base angle of attack influences, non-linearly, the average angle of attack, and may even leave the wing more exposed to a stall condition if not adjusted properly. Another important parameter to be optimized in the traction phase is the reel-out speed. The contribution in this regard was to show that the reel-out speed value that maximizes the cycle power is lower than the value that maximizes the traction power. This happens because the positive effect of increasing the duty cycle is greater than the negative effect of generating less power in the traction phase. Considering a $12\,\mathrm{m}^2$ foil kite with maximum aerodynamic efficiency around 7 and subject to a nominal wind around $10\,\mathrm{m/s}$ it was observed that, by using a reel-out speed $26\,\%$ lower than the value that maximizes the traction power, the cycle power increases by $9\,\%$, reaching approximately $9.2\,\mathrm{kW}$, which corresponds to $67\,\%$ of the average traction power. The increment in the cycle power by increasing the duty cycle was accompanied by a $28\,\%$ increase in the average traction force during the reeling-out. Other parameters optimized for the traction phase were the average polar angle of the lying eight and the average tether length, which depend on the parameters of the wind shear model considered.

For the retraction phase, a maneuver was designed aiming at maximizing the cycle power. To this end a flight trajectory at zero azimuth was established, during which the base angle of attack (de-powering process) and the traction force are ramped down towards constant values. Therefore the parameters to be tuned are the two ramp inclinations and the two constant values. Assuming a maximum feasible de-powering and an ad-hoc value for the traction force ramp inclination, a grid search was carried out to optimize the constant values of base angle of attack and traction force without violating constraints on the minimum angle of attack and tether reel speed saturation. The first constraint is particularly important in the case of a flexible wing to ensure that the kite maintains its proper inflated shape, whereas the reel-in speed saturation corresponds to a practical limitation of the ground

winch, which must be respected for a feasible maneuver. Because the retraction phase is computed based on the solution of the traction phase and vice-versa, the operating parameters of the pumping cycle were adjusted by means of an iterative algorithm.

The pumping kite power curve was computed by varying the reference wind speed applied to the wind shear model while considering a cycle power simplified in two ways: the reel-out speed that maximizes the traction power was used, and it was assumed an ad-hoc retraction phase during which the wing remains at a constant polar angle while the tether is reeled-in at the saturation speed. Two differences with respect to the wind turbine power curve were discussed. First, as the wind keeps increasing above the point where the rated (traction) power is reached, the cycle power starts to decline because of the progressive increase in the traction force during the reeling-in. The second difference is that, because of the degree of freedom to decrease the polar angle and, thereby, to limit the traction power, the pumping kite is thought of being able to operate at higher wind speeds, where the wind turbine would have already been put out of operation for safety reasons. This advantage of the pumping kite can contribute to an increase in its capacity factor.

In wind energy technology, it is well known that the maximum fraction of power (the power coefficient) that can be harvested from the wind flow through a wind turbine is $16/27 \approx 0.59$: the Betz limit. We have revisited the modeling procedure leading to the derivation of this limit, highlighting that it in fact applies to a generic device named the "actuator disc", which is subject to a thrust force resulting from the interaction between the wind speed far upstream of the disc and the "permeability" of the disc to the wind (the axial induction factor). The harvested power of the actuator disc is formulated as the thrust times the wind speed going through the disc. Observe that this is not how a horizontal-axis wind turbine operates. Its harvested power results from the torque on the disc times its angular speed. The contribution of this dissertation in this context is to point out that Loyd's lift (the pumping kite traction phase) and drag modes can be seen as particular cases of the actuator disc, just as the horizontal-axis turbine is. Using blade element momentum theory, once the expressions of the thrust and torque on a ring of the actuator disc have been formulated, the harvested power of the lift mode is obtained by considering the product between the thrust and the introduced reel-out (downstream) speed of the disc, which should be subtracted from the wind speed far upstream. By maximizing the resulting power expression, the optimal reel-out speed is obtained: one-third of the wind speed far upstream – a result which is already known by working with specific AWE models.

Lastly, it was carried out a comparison on the capacity factor of a

wind turbine and a pumping kite, the latter with an existing foil (ram-air) kite. When considering the wing area equal to the combined area of the three turbine blades, it could be seen that, given the much higher aerodynamic efficiency of the wind turbine airfoil and the loss of cycle power of the pumping kite due to the retraction phase, the capacity factor of the wind turbine tends to be greater. However, we should note that adding more wing area to the pumping kite while keeping its rated power constant would augment its power curve and, thereby, the capacity factor, approaching the values achieved by the turbines. The increase in the kite area would probably pay off due to the much lower costs of the flexible wing relative to the rigid blades. Furthermore, when adding to the larger kite a slightly higher aerodynamic efficiency, and more reel-in speed capability, the pumping kite achieves a higher capacity factor than the one turbine does in most of the locations considered. These observations, combined with the expectations of greatly reduced transportation and installation costs, establish a promising scenario for the further development and future deployment of pumping kite systems in commercial scale.

5.2 RECOMMENDATIONS FOR FUTURE WORK

In this work, the lying eight was considered as the flight path during the traction phase of the pumping kite. Nonetheless, the lying-eight is often chosen only because it allows the wing to remain in the high-power zone without accumulating torsion on the tether(s). If we were to employ a mechanism, similar to a fishing swivel, to avoid this issue on the pumping kite with only one tether between the ground winch and the airborne control pod, another candidate for the optimal flight trajectory would be a circle. In fact, the circle is the chosen trajectory for some AWE concepts, such as Makani Power's drag mode system. One hypothesis is that the circular trajectory may be advantageous w.r.t. the lying eight in terms of the control energy and ease of control. Note that, if there were no gravity, a constant steering input would be enough to produce the circle: the larger is the value of this constant steering input, the smaller is the radius of the trajectory. Nonetheless, due to the pull of gravity, when the wing passes closer to the ground the steering input must slightly increase, whereas the opposite happens when the wing flies in the upper part of the circle. Hence, we would need only a small varying control action on top of a constant value. If the steering actuator had something similar to a self-locking worm gearbox, no energy would be spent for the constant portion of the steering signal, and we would thereby save energy for the actuator. We can also postulate that the controller to track the circular tra-

jectory may be easier to design and more robust against wind perturbations, since the reference trajectory has a constant derivative (thus no inflections). In face of this promising prospect, the circular trajectory for the traction phase of a pumping kite is recommended for future works.

There is also significant room for improvement regarding the iterative optimization procedure for the cycle power. Firstly, although it was conceived for any airfoil with given aerodynamic curves, it may be hard to apply the method in the case of flexible wings because their aerodynamic characteristics, when known in the first place, may change depending on the wing loading, apparent wind speed, angle of attack and deformations induced by steering. Therefore one branch for future studies is the adaptation of the method for wings with unknown aerodynamic curves, possibly by means of online adaptation (maximum-seeking) and estimation algorithms. In this work, a simple grid search strategy was used with the purpose of illustrating how sensitive the optimal solution is with respect to changes in some parameters as, for instance, the base angle of attack and traction force setpoints of the reel-in phase. Therefore one possible improvement is the use of more powerful optimization tools that could not only compute the solution in a faster way, but also relax the constraints of a ramp followed by a constant value of the setpoints, thus obtaining a less conservative solution. Moreover, it would be desirable to include in the search the ramp inclinations of the base angle of attack and traction force. By doing so the cycle power could be further maximized.

One important observation on the pumping kite AWE concept is the need for a retraction phase. When considering rigid wings, de-powering should not be a problem since the wing shape is unaffected by the angle of attack. As we argued in this work, flexible wings are also attractive for a handful of reasons, but executing a "good" retraction phase with flexible kites is still a challenging task because of the limitation on the minimum angle of attack for safe operation. Another drawback is the limited reel-in speed of the ground winch: even if we could practically spend no energy during the retraction due to an excellent de-powering, we would still spend a significant amount of the cycle duration reeling in the tether, which has a negative impact on the cycle power. In short, the retraction phase is a crucial aspect of the pumping kite concept, and may be decisive in terms of whether such AWE system becomes economically feasible and reliable enough for operation. In face of these observations, the investigation of alternative mechanical structures at the ground for harvesting lift-mode power would also be an important task. Keep in mind that Loyd's drag mode system does not have its operation divided into traction and retraction phases, since the tether length is kept constant. However, drag mode systems tend to be technologically more complex,

besides other disadvantages w.r.t. lift-mode systems, therefore focus should be turned to the pumping kite retraction phase, with the goal of making it more efficient and reliable.

From a technical point of view, perhaps one of the most significant challenges that still remain is the development of autonomous launching and landing strategies for AWE pumping systems based on both flexible and rigid wings. When it comes to the latter wing type, there is the possibility of using relatively small turbines in order to have the aircraft hover during the transition maneuvers – a strategy employed e.g. by the Swiss company TwingTec. Such small on-board turbines are hard to attach to a flexible wing like a LEI tube or a ram-air kite, in which case a dedicated structure based e.g. on a mast would have to be designed. The level of complexity and automation, as well as the robustness of these launching and landing strategies will impact the operation costs of the AWE power plant. These costs, along with the maintenance costs, will determine how competitive, and in which power scale, AWE pumping systems will be in comparison to the conventional wind energy technology of nowadays.

To conclude these recommendations, let us recall the effort of comparing horizontal-axis wind turbines and tethered wings under the same modeling framework through blade element theory. The expression for the power coefficient of Loyd's lift mode was formulated in this dissertation, but the computation of the axial and radial induction factors and the angle of relative wind at each annular section of the disc must still be carried out. The power coefficient could be formulated for Loyd's drag mode as well. The solution of these problems would be another valuable contribution, since the current models used for tethered wings do not take into account the conservation of energy. As a consequence, the power extraction from the wind increases indefinitely (and non-linearly) with the increase in the aerodynamic efficiency of the wing, which is obviously something not realistic.

5.3 PUBLICATIONS AND RESEARCH GRANTS

The following papers were written in the scope of this dissertation:

- LELLIS, M. D.; SARAIVA, R.; TROFINO, A. Turning angle control of power kites for wind energy. In: **Proceedings of the IEEE 52nd Annual Conference on Decision and Control**. Firenze, Italy: IEEE, 2013. p. 3493–3498.

- SARAIVA, R.; LELLIS, M. D.; TROFINO, A. Passive phase design of a pumping kite wind generator. In: **Proceedings of the 19th IFAC**

World Congress. Cape Town, South Africa: IFAC, 2014. vol 19, n. 1, p. 6764–6769.

- LELLIS, M. D.; SARAIVA, R.; TROFINO, A. On the optimisation of pumping kites for wind power. In: SCHMEHL, R. (Ed.). **Airborne Wind Energy Conference**. the Netherlands: TU Delft, 2015, p. 63.

- TIL, J. V.; LELLIS, M. D.; SARAIVA, R.; TROFINO, A.; SCHMEHL, R. Dynamic model of a bridled kite including rotational deformations. In: SCHMEHL, R. (Ed.). **Airborne Wind Energy Conference**. the Netherlands: TU Delft, 2015. p. 48.

- SARAIVA. R.; LELLIS, M. D.; TROFINO, A.; CAVALCANTI, D. Online parameter estimation for flight control of tethered airfoils. In: SCHMEHL, R. (Ed.). **Airborne Wind Energy Conference**. the Netherlands: TU Delft, 2015. p. 62.

- LELLIS, M. D.; MENDONÇA, A. K.; SARAIVA, R.; TROFINO, A.; LEZANA, Á. Electric power generation in wind farms with pumping kites: An economical analysis. **Renewable Energy**, vol. 86, p. 163–172, February 2016.

- LELLIS, M. D.; SARAIVA, R.; TROFINO, A. On the Optimization of Pumping Cycles for Power Kites. In: SCHMEHL, R. (Ed.). **Airborne Wind Energy**. Springer-Verlag, 2016, (Advances in Technology Development and Research). chap. 6. *Accepted for publication*.

- TIL, J. V.; LELLIS, M. D; SARAIVA, R.; TROFINO. A. Dynamic model of a C-shaped Bridled Kite using a few Rigid Plates. In: SCHMEHL, R. (Ed.). **Airborne Wind Energy**. Springer-Verlag, 2016, (Advances in Technology Development and Research). chap. 34. *Accepted for publication*.

BIBLIOGRAPHY

Altaeros Energies. **The next transformation in rural infrastructure efficiency**. URL: <http://www.altaerosenergies.com/>.

ARCHER, C. L. An introduction to meteorology for airborne wind energy. In: AHRENS, U.; DIEHL, M.; SCHMEHL, R. (Ed.). **Airborne Wind Energy**. Berlin Heidelberg: Springer-Verlag, 2014, (Green Energy and Technology). chap. 5, p. 81–94.

ARCHER, C. L.; CALDEIRA, K. Global assessment of high-altitude wind power. **Energies**, vol. 2, n. 2, p. 307–319, 2009.

ARGATOV, I.; SILVENNOINEN, R. Energy conversion efficiency of the pumping kite wind generator. **Renewable Energy**, vol. 35, n. 5, p. 1052–1060, 2010.

BAAYEN, J. H. Modeling a kite on a variable length flexible tether. WI5012 Internship Report. Delft University of Technology. Supervisor: R. Schmehl. 2011.

BAAYEN, J. H. Vortexje - an open-source panel method for co-simulation. Cornell University Library. 2012. URL: <http://arxiv.org/abs/1210.6956>.

BAAYEN, J. H.; OCKELS, W. J. Tracking control with adaption of kites. **IET Control Theory and Applications**, vol. 6, n. 2, p. 182–191, 2012.

BAKULE, L. Decentralized control: An overview. **Annual Reviews in Control**, vol. 32, n. 1, p. 87–98, April 2008.

BOSCH, A.; SCHMEHL, R.; TISO, P.; RIXEN, D. Dynamic nonlinear aeroelastic model of a kite for power generation. **AIAA Journal of Guidance, Control and Dynamics**, vol. 37, n. 5, p. 1426–1436, 2014.

BREUKELS, J. **An Engineering Methodology for Kite Design**. Dissertation (PhD) — Delft University of Technology, 2011.

CANALE, M.; FAGIANO, L.; IPPOLITO, M.; MILANESE, M. Control of tethered airfoils for a new class of wind energy generator. In: **Proceedings of the 45th IEEE Conference on Decision and Control**. San Diego, CA: IEEE, 2006. p. 4020–4026.

CANALE, M.; FAGIANO, L.; MILANESE, M. Power kites for wind energy generation - fast predictive control of tethered airfoils. **IEEE Control Systems Magazine**, vol. 27, n. 6, p. 25–38, 2007.

CANALE, M.; FAGIANO, L.; MILANESE, M. Kitegen: A revolution in wind energy generation. **Energy**, vol. 34, n. 2, p. 355–361, 2009.

DIEHL, M. **Real-time optimization for large scale nonlinear processes**. Dissertation (PhD) — University of Heidelberg, 2001.

DIEHL, M.; MAGNI, L.; NICOLAO, G. D. Efficient NMPC of unstable periodic systems using approximate infinite horizon closed loop costing. **Annual Reviews in Control**, vol. 28, n. 1, p. 37–45, 2004.

Enerkite. **Airborne Wind Energy**. URL: <http://www.enerkite.com/>.

ERHARD, M.; STRAUCH, H. Control of towing kites for seagoing vessels. **IEEE Transactions on Control Systems Technology**, vol. 21, n. 5, p. 1629–1640, 2012.

ERHARD, M.; STRAUCH, H. Flight control of tethered kites in autonomous pumping cycles for airborne wind energy. **Control Engineering Practice**, vol. 40, n. 0, p. 13–26, 2015. ISSN 0967-0661.

ESRL. **Radiosonde database**. Earth System Research Laboratory of the National Oceanic and Atmospheric Administration, USA. URL: <http://www.esrl.noaa.gov/raobs/>.

FAGIANO, L. **Control of tethered airfoils for high-altitude wind energy generation**. Dissertation (PhD) — Politecnico di Torino, 2009.

FAGIANO, L.; MILANESE, M.; PIGA, D. High-altitude wind power generation. **IEEE Transactions on Energy Conversion**, IEEE, vol. 25, n. 1, p. 168–180, 2010.

FAGIANO, L.; MILANESE, M.; PIGA, D. Optimization of airborne wind energy generators. **International Journal of Robust and Nonlinear Control**, vol. 22, n. 18, p. 2055–2083, 2011.

FAGIANO, L.; ZGRAGGEN, A. U.; MORARI, M.; KHAMMASH, M. Automatic crosswind flight of tethered wings for airborne wind energy: Modeling, control design and experimental results. **IEEE Transactions on Control Systems Technology**, vol. 22, n. 4, p. 1433–1447, July 2013.

FECHNER, U.; SCHMEHL, R. Design of a Distributed Kite Power Control System. In: **Proceedings of the 2012 IEEE International Conference on Control Applications**. Dubrovnik, Croatia: IEEE, 2012. p. 800–805.

FECHNER, U.; SCHMEHL, R. Model-based efficiency analysis of wind power conversion by a pumping kite power system. In: AHRENS, U.; DIEHL, M.; SCHMEHL, R. (Ed.). **Airborne Wind Energy**. Berlin Heidelberg: Springer, 2013. chap. 14, p. 249–269.

FECHNER, U.; van der Vlugt, R.; SCHREUDER, E.; SCHMEHL, R. Dynamic model of a pumping kite power system. **Renewable Energy**, vol. 83, p. 705–716, November 2015.

GL Garrad Hassan. **Market Status Report High Altitude Wind Energy**. August 2011. URL: <http://www.gl-garradhassan.com/assets/technical-/Market-Report_HAW-Energy.pdf>.

GOLDSTEIN, L. Theoretical analysis of an airborne wind energy conversion system with a ground generator and fast motion transfer. **Energy**, n. 0, p. 987–995, 2013.

GWEC. **Global Wind Report, Annual Market Update**. 2011. Global Wind Energy Council. URL: <http://gwec.net/wp-content/uploads/2012/06-/Annual_report_2011_lowres.pdf>.

GWEC. **Global Wind Report, Annual Market Update**. 2014. Global Wind Energy Council. URL: <http://www.gwec.net/wp-content/uploads-/2015/03/GWEC_Global_Wind_2014_Report_LR.pdf>.

HARARI, Y. N. **Sapiens: A Brief History of Humankind**. 1st. ed. New York, NY, USA: HarperCollins, 2015.

HOUSKA, B.; DIEHL, M. Optimal control for power generating kites. In: **Proceedings of the 9th European Control Conference**. Kos, Greece: IEEE, 2007. p. 3560–3567.

IEA. **Technology Roadmap – Wind Energy**. 2013. Internation Energy Agency. URL: <https://www.iea.org/publications/freepublications-/publication/Wind_2013_Roadmap.pdf>.

IEA. **World Energy Outlook**. 2013. International Energy Agency. URL: <https://www.iea.org/publications/freepublications/publication/WEO2013-.pdf>.

ILZHöFER, A.; HOUSKA, B.; DIEHL, M. Nonlinear MPC of kites under varying wind conditions for a new class of large-scale wind power generators. **International Journal of Robust and Nonlinear Control**, vol. 17, n. 17, p. 1590–1599, 2007.

IPCC. **Climate Change 2014: Synthesis Report. Contribution of Working Groups I, II and III to the Fifth Assessment Report of the Intergovernmental Panel on Climate Change**. 2014. Core Writing Team, R.K. Pachauri and L.A. Meyer (eds.). Geneva, Switzerland, 151 pp.

JEHLE, C.; SCHMEHL, R. Applied tracking control for kite power systems. **AIAA Journal of Guidance, Control, and Dynamics**, vol. 37, n. 4, p. 1211–1222, 2014.

LELLIS, M. D.; MENDONCA, A. K.; SARAIVA, R.; TROFINO, A.; LEZANA, A. Electric power generation in wind farms with pumping kites: An economical analysis. **Renewable Energy**, vol. 86, p. 163–172, February 2016.

LELLIS, M. D.; SARAIVA, R.; TROFINO, A. Turning angle control of power kites for wind energy. In: **Proceedings of the IEEE 52nd Annual Conference on Decision and Control**. Firenze, Italy: IEEE, 2013. p. 3493–3498.

LOYD, M. L. Crosswind kite power. **Journal of Energy**, vol. 4, n. 3, p. 106–111, 1980.

LUCHSINGER, R. H. Pumping cycle kite power. In: AHRENS, U.; DIEHL, M.; SCHMEHL, R. (Ed.). **Airborne Wind Energy**. Berlin Heidelberg: Springer, 2013. chap. 3, p. 47–64.

Makani Power. **Response to the Federal Aviation Authority; Docket No. FAA-2011-1279; Notice No. 11-07; Notification for Airborne Wind Energy Systems (AWES)**. URL: <http://www.makanipower.com>.

MANWELL, J. F.; MCGOWAN, J. G.; ROGERS, A. L. **Wind Energy Explained: Theory, Design and Application**. 2. ed. Chichester: John Wiley & Sons, Ltd., 2009.

Minesto. **Power from tidal and ocean currents**. URL: <http://www.minesto.com>.

NREL. **Wind Turbine Airfoils**. National Renewable Energy Laboratory. URL: <https://wind.nrel.gov/airfoils/>.

OCKELS, W. J. Laddermill, a novel concept to exploit the energy in the airspace. **Aircraft Design**, vol. 4, n. 2–3, p. 81–97, June–September 2001.

PAULIG, X.; BUNGART, M.; SPECHT, B. Conceptual design of textile kites considering overall system performance. In: AHRENS, U.; DIEHL, M.; SCHMEHL, R. (Ed.). **Airborne Wind Energy**. Berlin Heidelberg: Springer, 2013. chap. 32, p. 547–562.

SCHMEHL, R. (Ed.). **Airborne Wind Energy Conference – Book of Abstracts**. the Netherlands: Delft University of Technology, 2015.

SCHMEHL, R.; NOOM, M.; van der Vlugt, R. Traction power generation with tethered wings. In: AHRENS, U.; DIEHL, M.; SCHMEHL, R. (Ed.). **Airborne Wind Energy**. Berlin Heidelberg: Springer, 2013. chap. 2, p. 23–45.

SILVA, R. S. d. **Aerofólios Cabeados para Geração de Energia Elétrica**. Thesis (Master) — Federal University of Santa Catarina, Florianopolis, Brazil, 2014.

STEVENS, B. L.; LEWIS, F. L. **Aircraft Control and Simulation**. 2nd. ed. Hoboken, New Jersey: John Wiley & Sons, Ltd, 2003.

THRESHER, R.; ROBINSON, M.; VEERS, P. To capture the wind. **Power and Energy Magazine, IEEE**, IEEE, vol. 5, n. 6, p. 34–46, 2007.

TwingTec. **TwingPower: Wind Energy 2.0**.

VAUGHN, A. C. **Path Planning and Control of Unmanned Aerial Vehicles in the Presence of Wind**. Thesis (Master) — University of California at Berkeley, USA, 2003.

VLUGT, R. van der; PESCHEL, J.; SCHMEHL, R. Design and experimental characterization of a pumping kite power system. In: AHRENS, U.; DIEHL, M.; SCHMEHL, R. (Ed.). **Airborne Wind Energy**. Berlin Heidelberg: Springer, 2013. chap. 23, p. 403–425.

WILLIAMS, P.; LANSDORP, B.; OCKELS, W. Optimal crosswind towing and power generation with tethered kites. In: **AIAA Guidance, Navigation and Control Conference and Exhibit**. Hilton Head, South Carolina: American Institute of Aeronautics and Astronautics, 2007.

WILLIAMS, P.; LANSDORP, B.; OCKELS, W. J. Nonlinear control and estimation of a tethered kite in changing wind conditions. **AIAA Journal of Guidance, Control and Dynamics**, vol. 31, n. 3, 2008.

YATES, R. C. **A Handbook On Curves and Their Properties**. Ann Arbor, Michigan, USA: J. D. Edwards, 1959.

ZGRAGGEN, A. U.; FAGIANO, L.; MORARI, M. Real-time optimization and adaptation of the crosswind flight of tethered wings for airborne wind energy. **IEEE Transactions on Control Systems Technology**, vol. 23, n. 2, p. 434–448, March 2015.

ZGRAGGEN, A. U.; FAGIANO, L.; MORARI, M. Automatic retraction and full-cycle operation for a class of airborne wind energy generators. **IEEE Transactions on Control Systems Technology**, vol. 24, n. 2, p. 594–608, March 2016.

ZILLMANN, U.; HACH, S. Financing strategies for airborne wind energy. In: AHRENS, U.; DIEHL, M.; SCHMEHL, R. (Ed.). **Airborne Wind Energy**. Berlin Heidelberg: Springer, 2014. chap. 7, p. 117–137.